Exact diagonalization study of strongly correlated topological quantum states

Mengsu Chen

Dissertation submitted to the Faculty of the
Virginia Polytechnic Institute and State University
in partial fulfillment of the requirements for the degree of

Doctor of Philosophy
in
Physics

Vito W. Scarola, Chair
Eric R. Sharpe
Chenggang Tao
Uwe C. Täuber

November 29th, 2018
Blacksburg, Virginia

Keywords: exact diagonalization, fractional Chern insulators, topological Mott insulators, charge density wave, optical lattice, emergent kinetic

Exact diagonalization study of strongly correlated topological quantum states

Mengsu Chen

(ABSTRACT)

A rich variety of phases can exist in quantum systems. For example, the fractional quantum Hall states have persistent topological characteristics that derive from strong interaction. This thesis uses the exact diagonalization method to investigate quantum lattice models with strong interaction. Our research topics revolve around quantum phase transitions between novel phases. The goal is to find the best schemes for realizing these novel phases in experiments. We studied the fractional Chern insulator and its transition to uni-directional stripes of particles. In addition we studied topological Mott insulators with spontaneous time-reversal symmetry breaking induced by interaction. We also studied emergent kinetics in one-dimensional lattices with spin-orbital coupling. The exact diagonalization method and its implementation for studying these systems can easily be applied to study other strongly correlated systems.

Exact diagonalization study of strongly correlated topological quantum states

Mengsu Chen

(GENERAL AUDIENCE ABSTRACT)

Topological quantum states are a new type of quantum state that have properties that cannot be described by local order parameters. These types of states were first discovered in the 1980s with the integer quantum Hall effect and the fractional quantum Hall effect. In the 2000s, the predicted and experimentally discovered topological insulators triggered studies of new topological quantum states. Studies of strongly correlated systems have been a parallel research topic in condensed matter physics. When combining topological systems with strong correlation, the resulting systems can have novel properties that emerge, such as fractional charge. This thesis summarizes our work that uses the exact diagonalization method to study topological states with strong interaction.

Dedication

To Dad and Mom, you are the ground growing me.

To my wife, you are the sky shining and watering me.

To my daughter, you are the star keeping my imagination.

Acknowledgments

It is a journey in searching the richness of nature and ending up with the richness of the mind. My sincere gratitude goes to my advisor Prof. Vito. W. Scarola, for his continuous guidance. His broad knowledge and insightful vision help me a lot at each stage of my research. I also want to thank him for the care he gave to me beyond research.

I certainly must express my thankfulness to all my other committee members: Prof. Eric R. Sharpe, Prof. Chenggang Tao, Prof. Uwe C. Täuber. It is their insightful comments that inspire me to dig deeper into research.

I also want to thank the previous postdocs in my group: Dr. Fei Lin, Dr. Hoi-Yin Hui. In discussing with them, I was always able to find out solutions to many problems I encountered in research.

I would like to thank everyone appeared in my life. They are the reason why I would never forget my days here. I want to especially thank the people in my group: Mi Yan and Peter Raum, for sharing many interesting research projects.

Finally, I am thankful my parents Zhuxuan and Meichun, and my sister, for their unconditional support in all aspects.

I am thankful to my beautiful wife Naling for her company, understanding, and support.

Contents

List of Figures ix

List of Tables xvii

1 Introduction 1

2 Topological quantum states 8

2.1 Indistinguishable particles 9

2.2 Second quantization 11

2.3 Quantum lattice models 12

2.4 Tight-binding Hamiltonian 14

2.5 The quantum Hall effect 17

2.5.1 Laughlin's gauge argument 19

2.5.2 TKNN formula 21

2.6 Haldane's model 22

3 Exact diagonalization 25

3.1 Overview 26

3.2 Lanczos algorithm 27

3.3 Implementation 30

4 Reordering fractional Chern insulators into stripes of fractional charges with long-range interactions 34

4.1 Introduction 35

4.2 Model 37

4.3 Energetics 38

4.4 Stripe Order 40

4.5 Fractionally Charged Quasiparticles 42

4.6 Constraints on Effective Theories 45

4.7 Summary 45

5 Quantum anomalous Hall state from spatially decaying interactions on the decorated honeycomb lattice 47

5.1 Introduction 48

5.2 Model and methods 51

5.3 Phase diagram 54

5.4 Mean-field theory calculation 56

5.5 Exact diagonalization calculation 57

5.6 Quantum anomalous Hall phase 58

5.7 Spontaneous spatial-symmetry breaking phases 60

5.8 Summary 63

6 Stability of Emergent Kinetics in Optical Lattices with Artificial Spin-Orbit Coupling **65**

6.1 Introduction 65

6.2 Model 69

6.3 Band Dispersion and Band Mixing 75

6.4 Phase Diagram and Stability 80

6.5 Summary 84

7 Summary **87**

Bibliography **89**

List of Figures

2.1 Draw of the honeycomb lattice with A/B (red/blue) sublattices shows the nearest neighbor hopping t_1 defined in this section, and the complex next nearest neighbor hopping in Sec. 2.6. It also indicates the 3 nearest neighbor vectors (green) and 3 of the total 6 next nearest neighbor vectors (orange). . 15

2.2 The Band structure of the tight-binding Hamiltonian on honeycomb lattice with $t_1 = 1$. 16

2.3 Transport data of the two-dimensional electron system at the inversion layer of a silicon metal-oxide-semiconductor field-effect transistor (MOSFET) under constant magnetic field ($18T$) and constant source drain current ($1\mu A$) at temperature $1.5K$. The data shows the quantization of Hall conductance (the plateaus in Hall voltage U_H versus gate voltage V_g) and vanishing of resistance (the dips in potential probes voltage U_{PP}) 17

2.4 Transport data of the two-dimensional electron system at the interface between gallium arsenide (GaAs) and aluminum gallium arsenide (AlGaAs). The Hall resistance R_H shows Hall plateaus with quantized Hall conductance. In addition to the integer quantized Hall plateaus as seen in the integer quantum Hall effect, there are fractional quantized Hall plateaus as labeled in the figures. At the Hall plateaus, resistance R vanish. The dashed line shows the expected classical Hall resistance which is linear in the magnetic field. 18

2.5 Schematic plotting the ribbon used in Laughlin's gauge argument. 20

4.1 Energy spectrum for Coulomb interaction, showing 15-fold degeneracy of stripe phase 39

4.2 Top: Energy spectrum of Eq. (4.1) for $N = 10$ plotted as a function of the screening length. The colors correspond to the same (K_x, K_y) as in Fig. 4.1. The transition from an FCI to stripes at $\lambda \approx 6.5$ is signaled by a change in degeneracy from 3 to 15. For $\lambda \gtrsim 6.5$ each of the 3 FCI states acquire a 5-fold degeneracy. Bottom: The ground state structure factor peak plotted for the same parameters as the top panel. Inset: Schematic of a one-dimensional slice along the x-direction (perpendicular to the stripes). Spheres represent charge excess atop the uniform liquid. The $L_x = 5$ ($L_x = 6$) case fits a non-integer (integer) number of stripes and shows one of 5 (2) configurations. 40

4.3 The left panel plots the ground state structure factor versus wavevector for the uniform FCI for $\lambda = 1$ in Eq. (4.1). The right panel demonstrates the formation of a stripe state for the Coulomb interaction, $\lambda = \infty$. 42

4.4 Spectral flow of the FCI ($\lambda = 1$, top panel) and stripe state ($\lambda = \infty$, bottom panel) as a function of the flux in units of $\Phi_0 = h/e$ for $N = 10$. Both panels show a Φ_0 spectral periodicity and a $3\Phi_0$ eigenstate periodicity with respect to the flux. The spectral flows are adiabatic within the ground state manifold. The insets zoom in on the ground state manifolds. The colors correspond to the same (K_x, K_y) as in Fig. 4.1. 43

5.1 (a) Band structure along the high-symmetry path $M \to \Gamma \to K \to M$ [dashed line in Fig. (c)] in the first Brillouin zone. (b) The decorated honeycomb lattice and the 24-site cluster (red dots) studied by exact diagonalization. (c) The first Brillouin zone of the decorated honeycomb lattice and the band (color map) right above the Fermi point (a QBCP). 50

5.2 Density patterns for the Nematic Insulator (NI), Stripe, and Charge Density Waves (CDWs). The QAH pattern draws bond currents computed with arrows indicating the direction of the currents $\mathrm{Im}\langle c_i^\dagger c_j \rangle$. All plots are the result of mean field calculations but exact diagonalization produced the same configurations where comparisons could be made (see Sec. 5.5). 52

5.3 (a) Phase diagram obtained using exact diagonalization on Eq. (5.1). The symbols are results from calculations and the lines are a guide to the eye. The bond ordered (BO) phase is an uniform phase that results from the superposition of bond-ordered crystal configurations (see Sec. 5.7). (b) The same as (a) but the lines plot transitions obtained from self-consistent mean field theory on an infinite lattice. The dashed lines indicate second order phase transitions. The agreement between panels (a) and (b) shows strong evidence for a robust QAH phase. The QAH order appears to survive in non-interacting limits near the origin but here the QAH gap vanishes asymptotically with interaction strength. 53

5.4 Exact diagonalization calculation of the lowest 5 energies as a function of V_2 for $V_1 = 4$. The vertical dashed lines mark phase transitions determined by level crossings and order parameters. The numbers after '$\times$' label the ground state degeneracy. 54

5.5 Energy gap, $E_2 - E_0$, obtained from exact diagonalization, where E_0 is the lowest energy level, and E_2 is the third lowest level. (The second level, E_1, is always degenerate with E_0 within the QAH phase.) The gapped QAH and QAH* phases are separated by a nearly horizontal gap-closing line. The QAH gap also closes along the axes. 55

5.6 Bond currents computed from exact diagonalization on one of the two QAH states at $V_1 = 4$ and $V_2 = 3$. Arrows indicate the direction of the bond currents $\mathrm{Im}\langle c_i^\dagger c_j \rangle$, in agreement with mean field results plotted in Fig. 2 of the main text. 56

5.7 Top: Exact diagonalization calculation of the QAH order parameter measuring loop current as a function of interactions strength with $V_1 = V_2$. The sudden vanishing of λ_J indicates a transition from QAH ($\lambda_J \neq 0$) to CDW ($\lambda_J = 0$) along the $V_1 = V_2$ line in the phase diagram. Bottom: The same but for the CDW order parameter measuring the maximum density difference to show a phase transition from QAH (uniform, $\delta n = 0$) to CDW (nonuniform, $\delta n > 0$) along the $V_1 = V_2$ line in the phase diagram. 58

5.8 Left: The density-density correlations, $\langle n_i n_j \rangle - \langle n_i \rangle \langle n_j \rangle$, obtained from exact diagonalization and plotted as a function of the position of site j for the NI at $V_1 = 0.8$ and $V_2 = 2.4$, where the size of the dots represents the magnitude of the correlation and blue (orange) indicates positive (negative) sign. The reference site at i is indicated by a red cross. The NI breaks C_6 rotation symmetry down to C_3, while preserving translational symmetry. Right: The same but for the stripe phase at $V_1 = 20$ and $V_2 = 14$. The stripe phase breaks translational symmetry by doubling the unit cell along the direction of unit vectors. 59

5.9 Bond average $\left\langle c_i^\dagger c_j \right\rangle$ computed using exact diagonalization for an excitation of the BO phase at $V_1 = 5$ and $V_2 = 0.2$, where the bond averages are always real. The width of the line along a bond indicates the magnitude of the average and bonds with the same color have the same magnitude. This BO crystal excitation breaks rotational symmetry, but preserves translational symmetry. 62

6.1 Schematic plotting the stability of the Wigner crystal phase (lobe) in the parameter space of single-particle band gap versus bandwidth. F defines the flatness ratio. Increasing the single-particle bandwidth makes the single-particle band more dispersive whereas increasing the single-particle band gap suppresses band mixing between the partially filled lower band and the upper band. $W \to 0$ corresponds to a perfectly flat band and $\Delta_s \to \infty$ leads to a single band at low filling. The work presented here considers a more physical model with experimentally realistic numbers for W and Δ_s. The lobe shows that the Wigner crystal with emergent Luttinger liquid properties remains stable and is adiabatically connected to the Wigner crystal in the physical model considered here. 67

6.2 Single-particle energies as a function of wavevector for the two bands, $\alpha = \pm$. The solid lines plot Eq. (6.11) for $\Omega = 2.5t$ and $k_R = k_L/2$ which lead to a flatness ratio $F \approx 7$. The dashed lines plot the same but for Eqs. (6.23) and (6.24) with the dimensionless parameters $\varepsilon = 0.6$ and $\eta = 0.9$ introduced to tune the single-particle bandwidth and the band gap, respectively. 72

6.3 Many-body energies versus total wavevector obtained from diagonalizing Eq. (6.25) in four distinct limits of the parameters ε and η. The energy zero is the ground state energy, E_g. The projected model, Eq. (6.21), is retrieved for $\varepsilon = \eta = 0$ (upper left). A non-zero bandwidth is introduced for $\varepsilon = 1$ and $\eta = 0$ (upper right) while a second flat band is introduced for $\eta = 1$ and $\varepsilon = 0$ (lower left). The full physical model, Eq. (6.20), is retrieved for $\varepsilon = \eta = 1$ (lower right). The ground state remains a Wigner crystal with 2-fold sublattice degeneracy in all four panels and we have checked that the ground state energy and ground state wave functions are adiabatically connected between the four limits. Comparing the $\eta = 0$ to $\eta = 1$ cases shows that band mixing lowers the many-body band gap, Δ_m, by a factor of ≈ 20. We have used the following parameters: $N = 6$, $L = 12$, $t = 0.01U$, $\Omega = 0.025U$, $k_R = k_L/2$, i.e., $\Delta_s = 0.05U$, and $W = 0.007U$. This corresponds to $F \approx 7$. 76

6.4 The many-body gap (top) and many-body wavefunction overlap (bottom) obtained from diagonalizing Eq. (6.25) as a function of the dimensionless parameter η. Here we see that the many-body gap is significantly lowered as we introduce a second single-particle band by increasing η. The bottom panel plots the overlap between the $\eta = 0$ wavefunction and the wavefunction for $\eta \geq 0$ for both the ground state ($n = 0$) and the first excited state ($n = 1$) to show that the second single-particle band alters the nature of just the first excited state. The parameters are the same as Fig. 6.3 but for $\varepsilon = 1$. 77

6.5 The same as Fig. 6.3 but for the full physical model, Eq. (6.20), where the squares (diamonds) are for $N = 6$ ($N = 8$) particles on $L = 12$ ($L = 16$) sites. The data collapse shows that the ground and first excited states are already in the thermodynamic limit. 78

6.6 The many-body energy gap plotted as function of bandwidth. The parameters are the same as Fig. 6.3 but for the full physical model, Eq. (6.20), with the band gap held constant, $\Delta_s = 0.08U$. Here we see that at zero bandwidth the single-particle basis states have no spread and, as a result, the interaction remains onsite and cannot lift the degeneracy. But as the bandwidth increases, the nearest-neighbor interaction terms lift the degeneracy to reveal the Wigner crystal ground state and opens a gap to a set of emergent excitations captured by an effective Luttinger liquid theory. But as the bandwidth increases further the gap closes as the Wigner crystal transitions to a conventional Luttinger liquid regime. 80

6.7 Characteristic many-body spectrum of Eq. (6.20) computed for a weakly interacting case (left panel, $U = t/2$) and the non-interacting case (right panel, $U = 0$). We have also set $N = 6$, $L = 12$, $\Omega = 2.5t$, and $k_R = k_L/2$. These parameters lead to a flatness ratio used in the other figures as well, $F \approx 7$. A comparison of both panels shows that the spectra are qualitatively similar, i.e., states occur at the same wavevectors and nearly the same energies. We can therefore think of the ground state in both cases as a partially filled band of weakly interacting fermions. The weakly interacting case conforms to conventional Luttinger liquid theory. 81

6.8 Stability phase diagram of the Wigner crystal with emergent kinetics plotted as function of both the single-particle band gap and the bandwidth. The color coding plots the size of the many-body gap obtained from diagonalization of Eq. (6.20) for $N = 6$, $L = 12$, and $k_R = k_L/2$. The circles plot the points where the many-body gap vanishes and the line is a guide to the eye. The Wigner crystal is stable within the lobe. Outside the lobe we have a conventional Luttinger liquid with a gap set by finite-size effects. 82

6.9 Strength of leading diagonal terms $V_1\tilde{n}_i\tilde{n}_{i+1}$ and leading off-diagonal terms $-t_1\chi^\dagger_{i+2}\tilde{n}_{i+1}\chi_i$ and $t_2\chi^\dagger_{i+3}\tilde{n}_i\chi_{i+1}$ (note that the signs before t_1 and t_2 are different) plotted as function of both the single-particle band gap Δ_s and the bandwidth W. 85

List of Tables

3.1 Estimated memory needed to store basis states of the half filled Hubbard model on the square lattice 31

Chapter 1

Introduction

Our world is built from only 98 elements. The complexity of the rich collection of phases emerging out of this simplicity can be attributed to the large number of ways collections of particles can interact with each other. As pointed out by P. W. Anderson, "more is different" [1]. Even with systems as simple as only two elements, hydrogen and oxygen, one can form different phases found in common phenomena, e.g, rain, hail, snow, fog.

Rich phase diagrams exist even for systems containing only electrons. The electronic properties of many materials serve as the foundation of modern technologies. There can be insulators, conductors, semiconductors or novel topological phases discussed in this thesis. Understanding the existence of, transitions between, and the stability of these phases is extremely important for building technologies utilizing the novel properties of these phases. For a long time, Landau theory was the general framework for understanding these phases in terms of symmetry breaking and local order parameters. Examples include magnetism and superconductors. However, the experimental discovery of the integer quantum Hall (IQH) effect in 1980 [2], and, later, the fractional quantum Hall (FQH) effect [3] in 1982, suggested phases beyond Landau's theory. These phases are featureless incompressible liquids with edge states that are robust to local perturbation. They also have quantized observables, such as conductance. FQH states can also have fractionally charged excitations and excitations with anyon statistics [4]. These phases are usually called topological quantum phases.

Quantized conductance is a special feature of topological phases. It can be attributed to the topological invariant given by the TKNN formula [5], which is mathematically robust to deformation. For a long time, IQH and FQH states were the only two topological phases confirmed by experiments. The theoretical proposal and later experimental discovery of the quantum spin Hall state and topological insulators in the 2000s broadened the set of realized topological quantum phases with topologically protected quantum numbers. It turns out that IQH and FQH states are just the tip of the iceberg of a far richer set of topological quantum phases, examples are $\mathcal{Z}_2$ topological insulators [6, 7], quantum anomalous Hall insulators [8, 9], fractional Chern insulators [10], and Weyl semimetals [11, 12], all of which have been discovered in experiments. There are also many other proposed topological quantum phases confirmed by numerical results, but waiting for experimental discovery. In this thesis, I will discuss two topological phases: the fractional Chern insulator (FCI) phase and topological Mott insulator (TMI) phase. The strong interaction between particles plays an essential role in forming these phases.

An FCI phase is the lattice analog of a FQH phase and is adiabatically connected to the FQH phase discussed in the continuum. Topological properties of IQH and FQH phases arise from Berry's phase which is, in turn, caused by external magnetic fields that break time-reversal symmetry (TRS). Unlike IQH and FQH phases, FCIs have topological properties originating from complex hoping in a lattice that explicitly break TRS. Similar to FQH states, the kinetic energy is quenched in an FCI. But the kinetic energy is not quenched by a strong external magnetic field. It is instead quenched by destructive interference derived from hopping between sites in a lattice. The destructive intereference leads to dispersionless bands (or called flat bands). The quenched kinetic energy makes the system sensitive to interactions, even at small interaction energy scales. Flat band systems are, therefore, strongly correlated system in the presence of any interactions. FCIs were first confirmed by

numerical calculations in various quantum lattice models [13–16]. There is also recently a report of experimental realization of FCIs in bilayer graphene [10]. Our work presented in this thesis is a reproduction of our previous publications on the stability of the FCI phase under long-range interactions. We have found a quantum phase transition between the FCI phase and a stripe phase of quasiparticles.

The second topic of this thesis is the TMI phase [17]. A TMI phase is an analog of an IQH phase, but without either the external magnetic field needed for an IQH state or the complex hopping found in Chern insulators (the non-interacting version of FCIs). Different from both IQH and FCIs, TMIs have topological properties arising solely from interaction effects. TRS in TMIs is spontaneously broken through interaction effects. TMIs arise from the instability of quadratic band crossing point (QBCP) under interaction. The work presented in this thesis is a reproduction of our previous publications of the phase diagram of a model Hamiltonian on the decorated Honeycomb lattice. We consider the creation of TMIs from a more realistic spatially decaying interaction. We also consider a model Hamiltonian on the kagome lattice. Or primary goal is to aid the experimental community in discovering the TMI phase.

This thesis describes numerical simulations of quantum lattice models, using exact diagonalization. Although topological insulators can be well described by single-particle topological band theory, there are essentially no very few analytic tools for studying strongly correlated topological quantum phases in an unbiased fashion. Numerical methods, mostly in the setting of quantum lattice models, are the only feasible approach for studying these phases. There have been many numerical methods that deal with quantum many-particle systems, such as exact diagonalization (ED), numerical mean field theory (MFT), quantum Monte Carlo (QMC), density matrix renormalization group (DMRG) or its generalization, tensor networks (TNs). Each of these methods has its own limitation. Generally, ED can only deal with small systems, MFT is not usually valid for strongly-correlated systems due to

quantum fluctuations, QMC is subject to the sign problem, and DMRG/TN can only deal with systems that satisfy a specific entanglement ansatz.

Of all of these methods, exact diagonalization, is often the most useful because of its versatility. It is capable of obtaining the wave function and energy spectrum while dealing with any system, including fermions, bosons, spins in one dimension, two dimensions, or three dimensiond. That makes it very suitable for studying new models when you do not want to apply an approximation. ED can provide almost every aspect of the low energy physics of those models since it directly obtains the wavefunction. These results can provide great insights into real physics. An example is the use of ED results by Laughlin to help guess the Laughlin wavefunction [18].

Although ED is subject to finite size effects, there are many techniques to help overcome this issue. For example, we can do finite size scaling by simulating different system sizes or we can change boundary conditions to detect bulk properties. We can also apply small perturbations to select the unique ground state wave function and compute many observables. For example, we will see how to compute microscopic loop currents directly using exact diagonalization to show spontaneous TRS breaking in topological Mott insulators.

ED is not limited to the study of topological phases discussed above. The primary advantage of ED is that it is such a generic method. This thesis also presents applications to flat band physics in one-dimensional optical lattices, which is also a reproduction of our previous publication. By taking into account band mixing effects and dispersive band effects, we use ED to study the stability of emergent kinetics found in previous work [19] and map out the stability phase diagram.

A by-product of this Ph.D. work is a package of generic ED codes written in C++ that can solve a broad class of models of interactions fermions, bosons, and spins on many types

of lattices. The lattices include the one-dimensional chain and also include more complicated patterns such as the decorated honeycomb lattice which contains six sublattices. The code can also take a generic interaction form that is not just limited to the density-density interaction as in other packages, such as ALPS [20].

The chapters are organized as follows:

The first part of this thesis, chapter 2 and 3, reviews the existing study of topological quantum phases and the ED technique. In chapter 2, I review the two topological quantum phases: the IQH and FQH states discovered in the 1980s. The understanding of the quantization of Hall conductance in these two states inspired many theories of new topological quantum phases studied in the last decades. For example, Laughlin's argument has been recently used in numerical methods including ED and DMRG as a signature of a topological phase [16, 21]. The TKNN formula has been used to directly compute Chern numbers from Berry curvatures [22]. I also review Haldane's lattice model [23] which is the first model demonstrating the possibility of having quantum Hall states without a net external magnetic field. This model can be viewed as the building block of the quantum spin Hall states. It also inspires the study of similar models containing fractional Chern insulators. In chapter 3, I review the Lanczos algorithm [24] which is an iterative eigenvalue solver. I also describe our generic ED implementation as well as parallelization for speedup.

In chapter 4, for the proposed FCI model on checkerboard lattice, we explored the stability of FCIs under a screened Coulomb interaction. Our motivation for this study is to find the analogue of collective excitations of composite fermions (CFs). It is well known that FQH liquid states can transform to states of quasiparticles such crystals and stripes. Different from regular long-range ordered states, these are the ordered states of CFs instead of electrons. As an analog of FCIs, we are interested in finding the same phenomena. Specifically, we would like to study the instability of FCIs to long-range interaction. Despite obtaining

numerical evidence of FCIs, previous studies all focused on short-range interaction, typically only nearest neighbor interaction. To study the instability, we use a Yukawa interaction with tunable screening length. Our Hamiltonian then interpolates between nearest neighbor and Coulomb interaction. Using exact diagonalization on these Hamiltonians at different screening lengths, we are able to find a quantum phase transition between FCIs to stripes of quasiparticles. The results in this chapter were published in [25].

In chapter 5, we discuss work searching for topological quantum phases without complex hoppings (as discussed for FCIs). Our research was inspired by previous mean-field theory results on various lattices [26]. The mean-field theory analysis suggests the existence of TRS breaking IQH analog states (or called quantum anomalous Hall states) in frustrated lattices with interaction. In such models, the Hamiltonian preserves TRS. The chiral QAH state spontaneously breaks TRS due to interactions. It is called a TMI. Following the MFT study, several ED results further confirmed TMIs in kagome lattices and checkerboard lattices. However, these models features nonspatially decaying interactions and/or anisotropic hopping, which is not realistic. We instead studied the more complicated decorated honeycomb lattice which has QBCPs too. We use complementary methods of MFT and ED to calculate density patterns and microscopic current loops. We map out the phase diagram of TMIs and neighboring charge ordered phases in the space of interaction strengths. The results show the existence of TMIs with spatially decaying interactions in this model. The results in this chapter were published in [27].

The work in chapter 6 discusses flat band physics akin to what was discussed in FCIs. We discuss flat bands in one-dimensional lattices that can be engineered by artificial spin-orbit coupling (SOC) and Zeeman fields in optical lattices. Because the band is nearly flat, even small interactions can drive rich physics. The work in this chapter is particularly interesting because it shows emergent kinetics. Previous work [19] made an approximation that excluded

band mixing and finite band width effects. in on a one-component model. We instead studied the full two-component model which takes into account both effects. We found the same data collapse of excitation modes. We further gave a realistic estimate of experimental parameters to find such states in optical lattice loaded with ^{40}K atoms. The results in this chapter were published in Ref. [28].

Chapter 2

Topological quantum states

This chapter reviews topological quantum states, particularly integer quantum Hall states, fractional quantum Hall states, Chern insulators, and fractional Chern insulators. These are the topological quantum states presented in this thesis. I start this chapter with a short review of second quantization and quantum lattice models to help clarify the notation used in this thesis. It is also critical for a correct implementation of the exact diagonalization method. This chapter then reviews Haldane's model on the honeycomb lattice which is the first Chern insulator model.

2.1 Indistinguishable particles

We start with the formalism for dealing with quantum states of non-interacting particles. For a single particle, an arbitrary state can be written as a linear combination of a complete, orthonormal basis states, denoted by $\{|\alpha\rangle\}$. The space containing these states is a single-particle Hilbert space, denoted $\mathcal{H}_1$. Mathematically we have

$$\langle\alpha|\beta\rangle = \delta_{\alpha\beta} \tag{2.1}$$

and

$$\sum_{\alpha} |\alpha\rangle\langle\alpha| = 1. \tag{2.2}$$

Now for two non-interacting particles, naively we would write down the state of the two-particle system as a whole by putting together the state of each particle. Let us say particle 1 is in state $|\alpha_1\rangle$ and particle 2 is in state $|\alpha_2\rangle$. We would then write the total state as a tensor product: $|\alpha_1\rangle|\alpha_2\rangle$. In the above notation, the first bracket is for particle 1 and the second is for particle 2. Note that the subscript α does not index particles, they just serve as different values for labeling different states.

For indistinguishable particles we can only say that one particle is in state $|\alpha_1\rangle$ while the other is in state $|\alpha_2\rangle$. So it is also possible that particle 1 in state $|\alpha_2\rangle$, particle 2 is in state $|\alpha_1\rangle$, and the total state is $|\alpha_2\rangle|\alpha_1\rangle$. This leads to the fact that the total state should be written as the superposition of all possible permutations while forming the tensor product of single-particle states. Depending on the statistics of the particles, the superposed state must be either symmetric (bosons) or antisymmetric (fermions) under permutation of single-

particle states. For two particles, it is

$$|\alpha_1\alpha_2\rangle = \frac{1}{\sqrt{2}}(|\alpha_1\rangle|\alpha_2\rangle \pm |\alpha_2\rangle|\alpha_1\rangle). \tag{2.3}$$

We denote such states, either symmetric or antisymmetric as $|\alpha_1\alpha_2\rangle$. Note that the Hermitian adjoint of $|\alpha_1\alpha_2\rangle$ is denoted as $\langle\alpha_1\alpha_2| = \frac{1}{\sqrt{2}}(\langle\alpha_1|\langle\alpha_2| \pm \langle\alpha_1|\langle\alpha_2|)$.

Generalizing to N non-interacting particles, the symmetrized state can be written as

$$|\alpha_1\alpha_2\cdots\alpha_N\rangle = \frac{1}{\sqrt{N!}}\sum_P \xi^P |\alpha_{P(1)}\rangle|\alpha_{P(2)}\rangle\cdots|\alpha_{P(N)}\rangle, \tag{2.4}$$

where $\xi = +1$ for bosons, $\xi = -1$ for fermions, ξ^P denotes the parity of permutation P, and $P(i)$ denotes the result of interger i under the permutation P.

The inner product of two states $|\alpha_1\alpha_2\cdots\alpha_N\rangle$ and $|\beta_1\beta_2\cdots\beta_N\rangle$ then can be written in a compact form

$$\langle\alpha_1\alpha_2\cdots\alpha_N|\beta_1\beta_2\cdots\beta_N\rangle = \begin{vmatrix} \langle\alpha_1|\beta_1\rangle & \langle\alpha_1|\beta_2\rangle & \cdots & \langle\alpha_1|\beta_N\rangle \\ \langle\alpha_2|\beta_1\rangle & \langle\alpha_2|\beta_2\rangle & \cdots & \langle\alpha_2|\beta_N\rangle \\ \vdots & \vdots & \ddots & \vdots \\ \langle\alpha_N|\beta_1\rangle & \langle\alpha_N|\beta_2\rangle & \cdots & \langle\alpha_N|\beta_N\rangle \end{vmatrix}_\xi, \tag{2.5}$$

where, when $\xi = -1$, the right hand side is a determinant, and when $\xi = +1$, the right hand side is a permanent. For bosons, note that $|\alpha_1\alpha_2\cdots\alpha_N\rangle$ is not normalized, only $\frac{1}{\sqrt{n_1!n_2!\cdots n_N!}}|\alpha_1\alpha_2\cdots\alpha_N\rangle$ is normalized, where n_i is the number of particles in state $|\alpha\rangle$.

2.2 Second quantization

Second quantization offers a major simplification in dealing with many-particle systems. Second quantization simplifies the above notation by converting the symmetrization process into commutation relations. We can introduce an operator $c_\gamma^\dagger$ corresponding to the state $|\gamma\rangle$ by defining

$$c_\gamma^\dagger|\alpha_1\alpha_2\cdots\alpha_N\rangle = |\gamma\alpha_1\alpha_2\cdots\alpha_N\rangle, \tag{2.6}$$

where as defined previously, $|\gamma\alpha_1\alpha_2\cdots\alpha_N\rangle$ is the properly symmetrized many-body state of $N+1$ particles. Hence, $c_\gamma^\dagger$ is called the creation operator of state $|\gamma\rangle$ because it creates a particle in state $|\gamma\rangle$. The adjoint of $c_\gamma^\dagger$ is called the annihilation operator c_γ.

By the definition of $c_\gamma^\dagger$ and c_γ and the explicit form of $|\alpha_1\alpha_2\cdots\alpha_N\rangle$, we can have the following commutation relations: (see Ref. [29])

$$[a_\alpha^\dagger, a_\beta^\dagger]_{-\xi} = [a_\alpha, a_\beta]_{-\xi} = 0, \tag{2.7}$$

$$[a_\alpha, a_\beta^\dagger]_{-\xi} = \delta_{\alpha\beta}, \tag{2.8}$$

where the notation $[A, B]_{-\xi}$ is defined as $AB - \xi BA$ for any two operators A and B.

The many-particle state can then be written as

$$|\alpha_1\alpha_2\cdots\alpha_N\rangle = c_{\alpha_1}^\dagger c_{\alpha_2}^\dagger \cdots c_{\alpha_N}^\dagger|0\rangle \tag{2.9}$$

and

$$\langle\alpha_1\alpha_2\cdots\alpha_N| = \langle 0|c_{\alpha_N}\cdots c_{\alpha_2}c_{\alpha_1}, \tag{2.10}$$

where $|0\rangle$ is the vacuum state. As can be seen here, the order of the single particle states matters. The rule of thumb is to stick to a particular order while representing basis states.

This would become extremely important when applying operators on basis states, as for fermions there will be additional signs entering the Hamiltonian matrix elements.

2.3 Quantum lattice models

Second quantization provides a convenient formalism for building models of many-particles hopping on a lattice. In this framework, the first step is to represent operators in second quantization form. For one-body operators, we can write $\hat{\mathcal{O}}^{(1)} = \sum_i \hat{o}_i$, which is the sum of single-particle operators $\hat{o}_i$. Examples include the total kinetic energy operator or total spin operator, written as

$$\hat{\mathcal{O}}^{(1)} = \sum_{\alpha\beta} \langle\alpha|\hat{o}|\beta\rangle c_\alpha^\dagger c_\alpha, \tag{2.11}$$

where $|\alpha\rangle$, $|\beta\rangle$ are the single-particle basis states.

Two-body operators $\hat{\mathcal{O}}^{(2)}$ capture the pair interactions between particles with interaction potential $\hat{o}^{(2)}$. An example includes the Coulomb interaction. Its second quantized form is

$$\hat{\mathcal{O}}^{(2)} = \frac{1}{2} \sum_{\alpha\beta\gamma\delta} \langle\alpha\beta|\hat{o}^{(2)}|\gamma\delta\rangle c_\alpha^\dagger c_\beta^\dagger c_\delta c_\gamma, \tag{2.12}$$

where $|\alpha\beta\rangle$, $|\gamma\delta\rangle$ are the basis states of the two-particle Hilbert space. As an illustration, if the basis states are position eigenstates $|x_1 x_2\rangle$ of a one dimensional system that has symmetric pair interaction $V(x_1, x_2)$, then the total interaction energy is:

$$\begin{aligned} H_I &= \frac{1}{2} \int \mathrm{d}x_1 \mathrm{d}x_2 \mathrm{d}x_3 \mathrm{d}x_4 V(x_1, x_2) \delta(x_4 - x_1) \delta(x_3 - x_2) c_{x_4}^\dagger c_{x_3}^\dagger c_{x_2} c_{x_1}, \\ &= \frac{1}{2} \int \mathrm{d}x_1 \mathrm{d}x_2 V(x_1, x_2) c_{x_1}^\dagger c_{x_2}^\dagger c_{x_2} c_{x_1}. \end{aligned} \tag{2.13}$$

We can now address a model with competing terms. A general N-particle Hamiltonian that consist of one-body and two-body operators in its first quantized form is

$$H = \sum_{i=1}^{N} \frac{\hat{p}_i^2}{2m} + U(r_i) + \frac{1}{2} \sum_{i \neq j}^{N} V(r_i, r_j), \tag{2.14}$$

where i indexes particles. We can further simplify this problem by choosing a basis. In quantum condensed matter, many systems studied are periodic systems that form lattices. A widely used single-particle basis is a set of Wannier wavefunction $\phi_{R_i}(r)$ which are usually chosen to be localized at position R_i and satisfy the property $\phi_{R_i+R}(r+R) = \phi_{R_i}(r)$, where R is any lattice vector.

We can now convert H into a form that incorporates the commutation relations. Using a second quantized Wannier basis, the Hamiltonian can be written as

$$H = \sum_{i,j} t_{ij} c_i^\dagger c_j + \frac{1}{2} \sum_{ijmn} V_{ijmn} c_i^\dagger c_j^\dagger c_n c_m, \tag{2.15}$$

where

$$t_{ij} = \int \mathrm{d}r \phi_i^*(r) \left[\frac{\hat{p}^2}{2m} + U(r) \right] \phi_j(r), \tag{2.16}$$

$$V_{ijmn} = \int \mathrm{d}r \mathrm{d}r' \phi_i^*(r) \phi_j^*(r') V(r, r') \phi_m(r) \phi_n(r'). \tag{2.17}$$

Here $\phi_i(r)$ is a simplified notation for the Wannier state localized at R_i. Hamiltonians in this form are usually called lattice models. The t_{ij} are called hopping amplitudes, and V_{ijmn} are called interaction matrix elements. The following will use numerical exact diagonalization to solve such models.

2.4 Tight-binding Hamiltonian

The Wannier basis yields a simple Hamiltonian with fewer terms. Because of the localized nature of Wannier states, the integrals that give hopping amplitudes and interaction matrix elements decay very quickly as the separation between Wannier states increases. This results in hopping amplitudes and interaction matrix elements that are only significant for neighboring sites and vanish otherwise. For interaction matrix elements, terms involving more than two sites are usually not significant. This results in keeping only density-density interaction terms of the form $c_i^\dagger c_j^\dagger c_j c_i$.

The approximate Hamiltonian obtained after throwing away negligible terms are called tight-binding Hamiltonians. Tight-binding Hamiltonians allow us to conveniently solve single particle Hamiltonians by transforming to momentum space. For example, consider an N_c-site one-dimensional lattice with only nearest neighbor hopping. The Hamiltonian reads

$$H_{1D} = t_1 \sum_{\langle i,j \rangle} c_i^\dagger c_j, \tag{2.18}$$

where $\langle i, j \rangle$ indicates a sum over all nearest neighbor sites, t_1 is the nearest neighbor hopping amplitude. We can solve this model by performing a Fourier transform on c_i. We then have

$$c_i = \frac{1}{\sqrt{N_c}} \sum_k e^{ik \cdot R_i} c_k, \tag{2.19}$$

where c_k is the annihilation operator for Bloch state $|k\rangle$, with $k = n\frac{2\pi}{Na}$, and $n = 0, \cdots, N-1$. Using this we can substitute c_i, c_j in Eq. (2.18) with Eq. (2.19), and consider translational symmetry. We then get

$$H_{1D} = \sum_k t_1 \left(\sum_\delta e^{ik\delta} \right) c_k^\dagger c_k = \sum_k 2t_1 \cos(ka) c_k^\dagger c_k. \tag{2.20}$$

Here we see that the Hamiltonian is diagonalized in the Bloch basis. The eigenvalues immediately yield the band structure $\varepsilon_k = 2t_1 \cos k$.

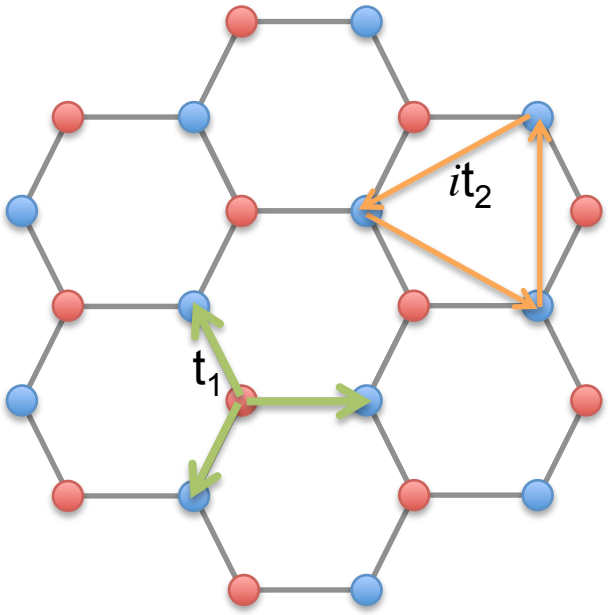

Figure 2.1: Draw of the honeycomb lattice with A/B (red/blue) sublattices shows the nearest neighbor hopping t_1 defined in this section, and the complex next nearest neighbor hopping in Sec. 2.6. It also indicates the 3 nearest neighbor vectors (green) and 3 of the total 6 next nearest neighbor vectors (orange).

For more complicated models that have extra degrees of freedom at each site, the same process follows, but the Hamiltonian will be a matrix over the extra degrees of freedom. The honeycomb lattice has more degrees of freedom due to sub-lattice symmetry. The honeycomb lattice is used to describe Graphene [30] and is used in the Haldane model [23] discussed in Sec. 2.6. If we consider only nearest neighbor hopping, the Hamiltonian in momentum space takes the form

$$H = \sum_k \begin{pmatrix} a_{\vec{k}}^\dagger & b_{\vec{k}}^\dagger \end{pmatrix} \begin{pmatrix} 0 & t_1\gamma_{\vec{k}} \\ t_1\gamma_{\vec{k}}^* & 0 \end{pmatrix} \begin{pmatrix} a_{\vec{k}} \\ b_{\vec{k}} \end{pmatrix}, \tag{2.21}$$

where we introduce $a_{\vec{k}} = c_{k,A}$ and $b_{\vec{k}} = c_{k,B}$ to simplify the notation. Here A and B index

the extra sublattice degree of freedom. The nearest neighbhor tunneling in momentum space is captured by:

$$\gamma_{\mathbf{k}} = \sum_{\vec{\delta}} e^{i\vec{k}\cdot\vec{\delta}}, \tag{2.22}$$

where $\vec{\delta}$ is the nearest neighbor vector pointing from A to B. Diagonalizing the 2×2 matrix, transforms the model to the band basis to effectively solve the non-interacting honeycomb lattice problem. The band structure reads

$$\varepsilon_k = \pm\sqrt{|\gamma_{\vec{k}}|^2}. \tag{2.23}$$

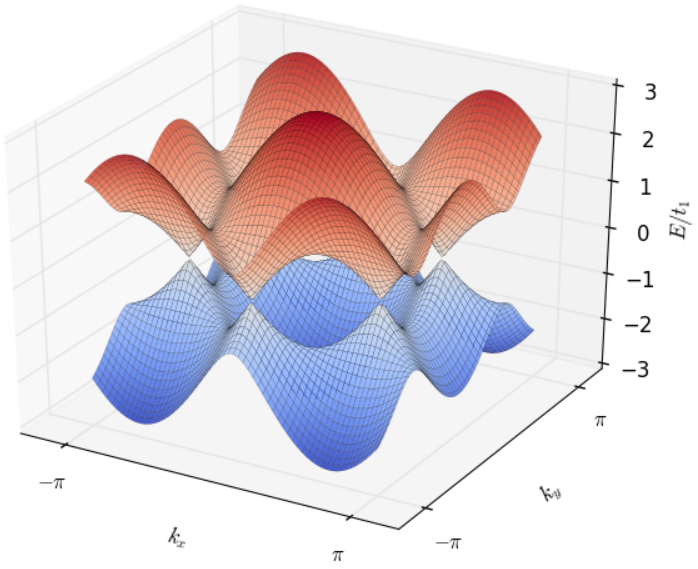

Figure 2.2: The Band structure of the tight-binding Hamiltonian on honeycomb lattice with $t_1 = 1$.

We will see in the Sec. 2.6 that next nearest neighbor hopping can open a gap in the above band structure, making this system an insulator. If the hopping amplitudes are complex

numbers, the system can be an insulator with nontrivial topology.

2.5 The quantum Hall effect

In this section, I will review the two topological quantum phases discovered experimentally in the 1980s: the integer quantum Hall states [2] and the fractional quantum Hall states [3]. These phases underlie the physics of the topological phases we study in this thesis.

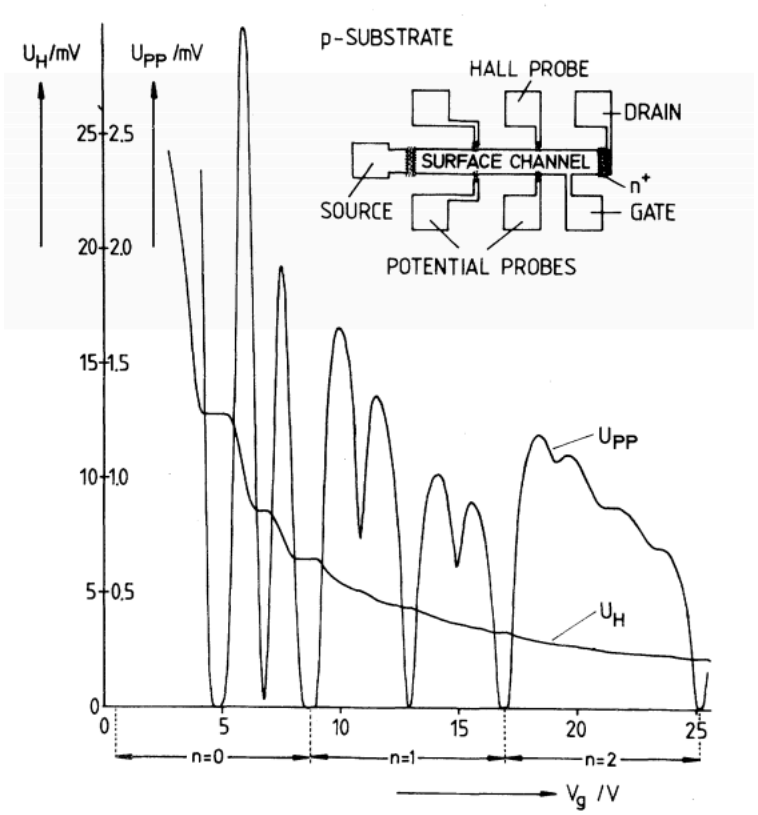

Figure 2.3: Transport data of a silicon metal-oxide-semiconductor field-effect transistor (MOSFET) under constant magnetic field ($18T$) and constant source drain current ($1\mu A$) at temperature $1.5K$. The data shows the quantization of Hall conductance (the plateaus in Hall voltage U_H versus gate voltage V_g) and vanishing of resistance (the dips in potential probes voltage U_{PP}). This figure is adopted from [2].

The quantum version of the Hall effect was observed in two-dimensional electron systems,

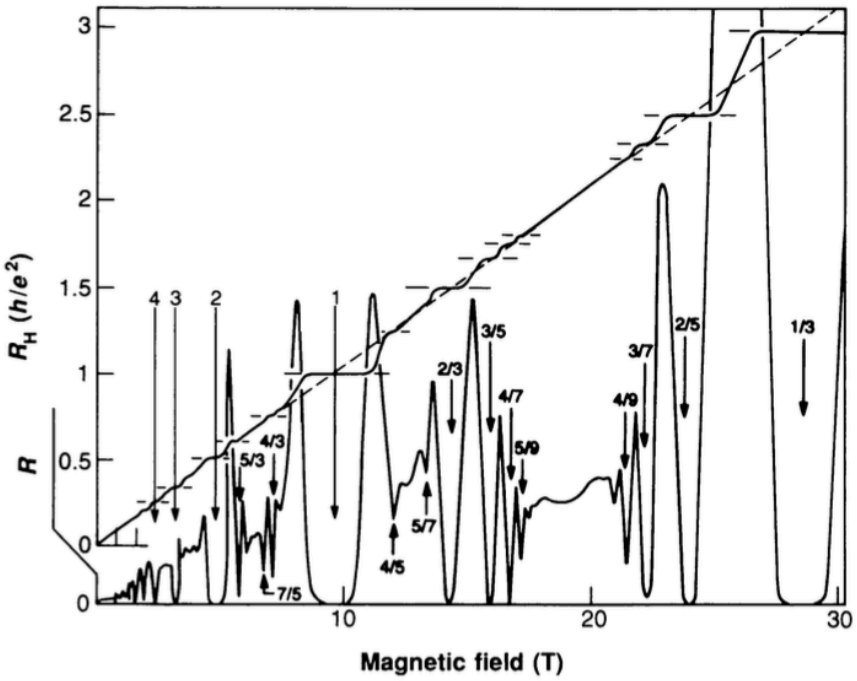

Figure 2.4: Transport data of the two-dimensional electron system at the interface between gallium arsenide (GaAs) and aluminum gallium arsenide (AlGaAs). The Hall resistance R_H shows Hall plateaus with quantized Hall conductance. In addition to the integer quantized Hall plateaus as seen in the integer quantum Hall effect, there are fractional quantized Hall plateaus as labeled in the figures. At the Hall plateaus, resistance R vanish. The dashed line shows the expected classical Hall resistance which is linear in the magnetic field. This figure is adopted from [31].

originally in the inversion layer of MOSFETs and under strong magnetic fields. This new phase of electrons, now called the quantum Hall state or more precisely, the integer quantum Hall state, was first discovered by von Klitzing in 1980 through the measurement of electron transport properties [2]. The most significant property is the so-called Hall plateau (Fig. 2.3), which shows extremely precise quantization of Hall conductance

$$\sigma_{xy} = n\frac{e^2}{h}, \tag{2.24}$$

where $n = 1, 2, 3, \cdots$, e is the elementary charge and h is Planck's constant. Concomitant

with the Hall plateau is the vanishing of the dissipative resistivity. Later in 1982, D. C. Tsui and H. L. Stormer et al. further discovered the fractional quantized version of quantum Hall effect (Fig. 2.4), now called fractional quantum Hall states. Unlike the IQH states, FQH states are fundamentally strongly correlated systems. The FQH states can have fractional charge excitations and fractional statistics that are not found in IQH states. Despite the difference, the theories in understanding the quantization of Hall conductance can be applied to both IQH and FQH states. For simplicity, we reviewed the theories for the noninteracting IQH states below. Similar theories for FQH states can be found in the literature [32, 33].

The quantization of Hall conductance is independent of the underlying materials or the amount of disorder. This suggests that it is a new phase with novel features related to transport. The key step of understanding this new phase is to understand the reason behind the quantized Hall conductance. There are two ways to understand the quantization which we describe below. We first describe the quantization from the perspective of gauge symmetry of the Hamiltonian. We then describe quantization resulting from topological invariants computed from the wavefunction.

2.5.1 Laughlin's gauge argument

We first consider quantization from the perspective of gauge symmetry. In a seminal paper [34], Laughlin considered an ideal setup of two-dimensional non-interacting electrons on a ribbon. The ribbon is bent into a loop (see Fig. 2.5). The electrons are subjected to a magnetic field perpendicular to the ribbon. There is also an in-plane uniform electric field from one edge to the other edge creating a potential difference across the ribbon. We now perturb the system by applying a magnetic flux ϕ through the loop formed by the ribbon and parallel to the ribbon. The magnetic flux is applied by adiabatically increasing its value.

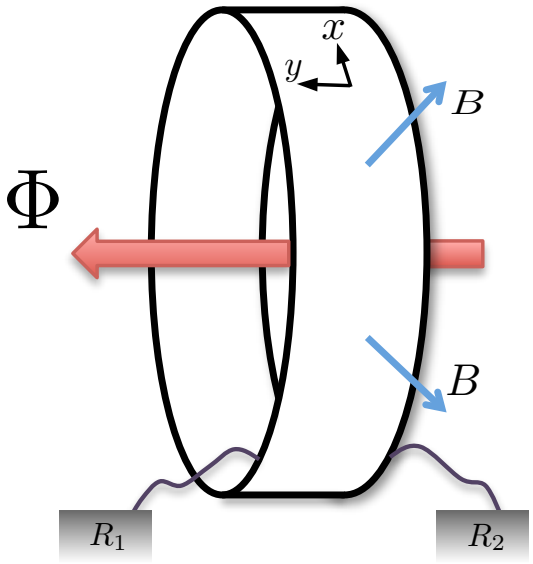

Figure 2.5: Schematic plotting the ribbon used in Laughlin's gauge argument. The magnetic field forming the FQH states is perpendicular to the ribbon. Flux Φ is idiomatically changing to pump electrons from one edge to another age. R_1 and R_2 are two electron reservoirs.

The change of flux will induce current along the loop, which can be computed as a derivative:

$$I = c\frac{\partial U}{\partial \phi}, \tag{2.25}$$

where U is the energy of electrons. Labeling the direction along the loop as $\hat{x}$ and across the ribbon as $\hat{y}$, we have the Hamiltonian

$$H = \frac{1}{2m}(\vec{p} - \frac{e}{c}\vec{A})^2 + eE_0 y. \tag{2.26}$$

Using the Landau gauge for the magnetic field piercing the ribbon:

$$A = H_0 y\hat{x} \tag{2.27}$$

there are vector fields along the ribbon loop. Meanwhile, adiabatically changing the flux can be treated as adiabatically changing the vector field along the ribbon loop too. So the

flux is effectively changing $\vec{A}$ of the original system. When the change of the flux is one flux quantum, $\frac{hc}{e}$, the Hamiltonian stays the same because of gauge invariance. The resulting change of energy must be due to n electrons being transferred from one edge to the other edge (assuming the two edges are connected to electron reservoirs).

Using this argument we can compute the current induced by the flux:

$$I = \frac{ne^2V}{h}, \tag{2.28}$$

where V is the potential drop between the two edges. The resulting Hall conductance is:

$$\sigma_{xy} = n\frac{e^2}{h} \tag{2.29}$$

This shows that gauge symmetry leads to a quantized Hall conductance.

We use a similar approach in our numerical simulations. Using Laughlin's argument we apply an additional phase to the hopping across the system boundary. This phase induces another boundary condition besides the periodic boundary condition. This so-called twisted boundary condition is used to generate the spectra flow discussed in chapter 4. The twisted boundary condition implements an effective flux which characterizes the robustenss of the spectra and, as in Laughlin's gauge argument, certifies quantized resitance.

2.5.2 TKNN formula

We now turn to the wavefunction-based analysis of quantized conductivity. A more general treatment of the quantization of the Hall conductance was first formulated by Thouless, Kohmoto, Nightingale, and den Nijs (TKNN) in 1982 [5]. The TKNN formula is a formula

for the Hall conductance

$$\sigma_{xy} = \frac{e^2}{h} \sum_{occ} \frac{1}{2\pi i} \int_{BZ} d^2k (\langle \partial_{k_1} u | \partial_{k_2} u \rangle - \langle \partial_{k_2} u | \partial_{k_1} u \rangle), \tag{2.30}$$

where the sum is over the occupied bands, the integral is over the Brillouin zone, and u is the simplified notation of the $u_{\mathbf{k}}(\mathbf{r})$ in Bloch wavefunction $\psi_{\mathbf{k}}(\mathbf{r}) = e^{i\mathbf{k}\cdot\mathbf{r}} u_{\mathbf{k}}(\mathbf{r})$.

The TKNN fomula shows that the quantization of the Hall conductance is the result of the fact that the value of the integral can only be multiples of 2π. Here the integral of the Gaussian curvature on a closed manifold is itself quantized. The idea of expressing observables as a topological invariant goes beyond describing quantum Hall states and has been found in many places in the very active area of topological quantum physics. The next section discusses the Haldane model and will demonstrate the use of the TKNN formula to identify topologically non-trivial states.

2.6 Haldane's model

We have seen in the last section that the external magnetic field causes the Berry phase in Bloch states which in turn leads to a topologically nontrivial IQH. In this section, we will see that topologically nontrivial states can occur even without external magnetic fields. In his 1989 paper [23], Haldane constructed a model on honeycomb lattices, now called Haldane's model. The model demonstrates the idea that an IQH state can occur in band-insulators with zero net magnetic field. Such states are now called Chern insulators (CIs) or quantum anomalous Hall (QAH) insulators. They show persistent topological properties: quantized Hall conductance and chiral edge modes, but without the need for an external magnetic field.

Haldane's model puts non-interacting particles on a honeycomb lattice. In addition to the conventional nearest hopping tight-binding Hamiltonian considered in Sec. 2.4, Haldane's model adds the second nearest neighbor hoppings which will open a gap in the band structure. To break time-reversal symmetry as needed for a quantum Hall state, the second nearest neighbor hoppings are chosen to be complex numbers, taken as it_2 in the following calculation. The hoppings from sublattice A to B and from B to A are now not equivalent. As a result, TRS is broken.

We can diagonalize the Haldane model following the same procedure discussed earlier in 2.4. Transforming the Hamiltonian to momentum space we have

$$H = \sum_k \begin{pmatrix} a_{\vec{k}}^\dagger & b_{\vec{k}}^\dagger \end{pmatrix} \begin{pmatrix} 2t_2\gamma'_{\vec{k}} & t_1\gamma_{\vec{k}} \\ t_1\gamma^*_{\vec{k}} & 2t_2\gamma'_{\vec{k}} \end{pmatrix} \begin{pmatrix} a_{\vec{k}} \\ b_{\vec{k}} \end{pmatrix} = \sum_k \begin{pmatrix} a_{\vec{k}}^\dagger & b_{\vec{k}}^\dagger \end{pmatrix} h(\vec{k}) \begin{pmatrix} a_{\vec{k}} \\ b_{\vec{k}} \end{pmatrix}, \quad (2.31)$$

where

$$\gamma'_{\vec{k}} = \sum_i \sin(\vec{k}\cdot\vec{\delta}'_i)$$

and $\vec{\delta}'_i$ is the second nearest neighbor vectors. Diagonalizing the 2×2 matrix $h(\vec{k})$ to obtain Bloch states, the Hall conductance given by the TKNN formula, becomes [35]:

$$\sigma_{xy} = \frac{e^2}{h}\frac{1}{4\pi}\int_{\mathrm{BZ}} \mathrm{d}^2\mathbf{k}\hat{\mathbf{h}}(k)\cdot\left(\frac{\partial\hat{\mathbf{h}}(k)}{\partial k_x}\times\frac{\partial\hat{\mathbf{h}}(k)}{\partial k_x}\right), \quad (2.32)$$

where we have decomposed $h(\vec{k})$ into Pauli matrices $\vec{\sigma} = (\sigma_x, \sigma_y, \sigma_z)$:

$$h(\vec{k}) = \vec{h}(\mathbf{k})\cdot\vec{\sigma}, \quad (2.33)$$

$$\vec{h}(\mathbf{k}) = \left(t_1\textstyle\sum_i\cos(\vec{k}\cdot\vec{\delta}_i),\quad -t_1\sum_i\sin(\vec{k}\cdot\vec{\delta}_i),\quad 2t_2\sum_i\sin(\vec{k}\cdot\vec{\delta}'_i)\right), \quad (2.34)$$

$$\widehat{\mathbf{h}}(\mathbf{k}) = \frac{\vec{h}(\mathbf{k})}{|\vec{h}(\mathbf{k})|}. \tag{2.35}$$

Here $\hat{\mathbf{h}}\,(\mathbf{k})$ is a unit vector and the quantity being integrated is just the infinitesimal area on a unit sphere caused by changes in $\mathbf{k}$. The integral in Eq. (2.32) is therefore the total area swept by $\widehat{\mathbf{h}}(\mathbf{k})$ while varying $\widehat{\mathbf{h}}(\mathbf{k})$. Because $\mathbf{k}$ forms a closed manifold (a torus because of periodic boundary condition), the integral value divided by 4π will be the number of times $\widehat{\mathbf{h}}(\mathbf{k})$ covers a sphere. It must be an integer. If we plot $\widehat{\mathbf{h}}(\mathbf{k})$ at each $\mathbf{k}$ in two dimensions, we can visualize counting nonzero coverage as checking the existence of a skyrmion. A skyrmion is a topological field configuration [36]. The above $\vec{h}(\mathbf{k})$ shows a skyrmion configuration.

The Haldane model offers a lattice model showing quantized Hall conductance without an external magnetic field. Haldane's model was initially invented as a toy model. It has served as a platform for, more generally, studying CIs. Advances in optical lattice technology have even experimentally implemented this model [37].

Chapter 3

Exact diagonalization

This chapter reviews the general components of the exact diagonalization method. We discuss how to enumerate basis states, build the Hamiltonian matrix, and solve for the lowest eigenvalues of the Hamiltonian matrix using iterative solvers. I also describe my implementation of exact diagonalization in the last section of this chapter.

3.1 Overview

Exact diagonalization starts by finding a complete set of basis states. For a Hamiltonian in second quantized form, the most natural choice of basis is the occupation number basis. Placing all single-particle states in a particular order, all the possible configurations of occupying these states form a complete orthonormal basis $\{|b_i\rangle\}$.

The matrix representation of Hamiltonian is then:

$$H_{ij} = \langle b_i|H|b_j\rangle. \tag{3.1}$$

When generating the matrix elements numerically, however, we do not naively take all pairs of i and j, and compute H_{ij}. Instead, we compute $H|b_j\rangle$ first. For most Hamiltonians, terms in it, such as nearest neighbor hoppings, only couple nearby basis states. So $H|b_j\rangle$, if written as a linear combination $H|b_j\rangle = \sum_i c_i|b_i\rangle$ where c_i is the coefficients, many c_i will be zero. The process of generating matrix elements is then to find the $|b_i\rangle$ with a nonzero coefficient, and determine the index of $|b_i\rangle$ in the basis, to add to the coefficient to the corresponding row. Techniques of determining the index of a basis state in a basis include Lin tables [38], hash [39], and binary search [40]. Note that constructing the full matrix is not always needed. We will find in the next section that only matrix-vector multiplication needs to be defined. However, the above procedure for defining the matrix-vector multiplication is the same. The next two sections discuss the Lanczos algorithm for solving low eigenenergy states and our implementation for the work of this thesis.

3.2 Lanczos algorithm

We are typically interested in low energy states of a quantum many-body system, especially the ground state. Among methods of getting to the ground state, the variational method may be most familiar. It minimizes the energy E by varying the wavefunction $|\Psi\rangle$:

$$E_{\min} = \min_{\psi} \frac{\langle\psi|H|\psi\rangle}{\langle\psi|\psi\rangle}. \tag{3.2}$$

The Lanczos algorithm [24] works in a similar fashion by following the spirit of a steepest descent search, starting from a random initial vector which is not orthogonal to the lowest eigenvector and stepping toward a more accurate representation of the desired state vector.

To outline the Lanczos procedure, assume that H is an $n \times n$ matrix that we want to diagonalize. $\lambda_{\min}$ is the minimal eigenvalue and $\mathbf{x}$ is a vector used for iterating. We can then write the minimum eigenvalue as:

$$\lambda_{\min} = \min_{\mathbf{x}} r(\mathbf{x}) = \min_{\mathbf{x}} \frac{\mathbf{x}^\dagger H\mathbf{x}}{\mathbf{x}^\dagger\mathbf{x}}. \tag{3.3}$$

For fast minimization, intuitively, we want to vary $\mathbf{x}$ in the opposite direction of the gradient of $r(\mathbf{x})$

$$\frac{\partial r(\mathbf{x})}{\partial \mathbf{x}} = \frac{2}{\mathbf{x}^\dagger\mathbf{x}}(H\mathbf{x} - r(\mathbf{x})\mathbf{x}). \tag{3.4}$$

This direction is within the space spanned by two vectors $\mathbf{x}$ and $H\mathbf{x}$. At each step of the iteration, we want to change $\mathbf{x}$ for some amount in the above direction. In other words, we want to find a vector within the space span$\{\mathbf{x}, H\mathbf{x}\}$. In the next step, we still want to search in the oppose direction of the gradient vector but using the vector in span$\{\mathbf{x}, H\mathbf{x}\}$ obtained from the last step. That finds a vector within the space span$\{\mathbf{x}, H\mathbf{x}, H^2\mathbf{x}\}$. After k iterations, the best $\mathbf{x}$ that minimizes $r(\mathbf{x})$ should live in the Krylov space $\mathcal{K}(H, \mathbf{x}, k) =$

span$\{\mathbf{x}, H\mathbf{x}, H^2\mathbf{x}, \cdots, H^{k-1}\mathbf{x}\}$. Now suppose we construct the orthonormal basis $Q_k = [\mathbf{q}_1\mathbf{q}_2\cdots\mathbf{q}_k]$ of space $\mathcal{K}(H, \mathbf{x}, k)$ at each step k, we will see we will be able to tri-diagonalize H using Q_n. That implies $Q_n^\dagger \mathrm{H}\mathrm{Q}_n = T$ is a tri-diagonal matrix. The following proves the tri-diagonalization.

The matrix elements of T can be written as $T_{ij} = \mathbf{q}_i^\dagger H \mathbf{q}_j$. By assumption, Q_k forms the orthonormal basis of the space $\mathcal{K}(H, \mathbf{x}, k)$. At each step k, we have $\mathbf{q}_j \in \mathcal{K}(H, \mathbf{x}, j)$, and $H\mathbf{q}_j \in \mathcal{K}(H, \mathbf{x}, j+1)$. And also by definition, $\mathbf{q}_i$ is orthogonal to $\mathcal{K}(H, \mathbf{x}, k)$ for any $i > k$. So $T_{ij} = \mathbf{q}_i^\dagger H \mathbf{q}_j$=0 if $i > j+1$. By symmetry, $T_{ij} = 0$ for $i < j-1$ too. So by constructing an orthonormal basis at each step, we are able to tri-diagonalize H.

If we write the tri-diagonal matrix T in the following form

$$T = \begin{pmatrix} \alpha_1 & \beta_1 & & & & \\ \beta_1 & \alpha_2 & \beta_2 & & & \\ & \beta_2 & \alpha_3 & \ddots & & \\ & & \ddots & \ddots & \beta_{n-2} & \\ & & & \beta_{n-2} & \alpha_{n-1} & \beta_{n-1} \\ & & & & \beta_{n-1} & \alpha_n \end{pmatrix} \tag{3.5}$$

and expand $Q^\dagger \mathrm{H}\mathrm{Q} = T$, we have

$$H\mathbf{q}_k = \beta_{k-1}\mathbf{q}_{k-1} + \alpha_k \mathbf{q}_k + \beta_k \mathbf{q}_{k+1}. \tag{3.6}$$

Multiplying both sides by $\mathbf{q}_k$, we can write

$$\alpha_k = \mathbf{q}_k^\dagger H \mathbf{q}_k. \tag{3.7}$$

So the next $\mathbf{q}_{k+1}$ is constructed by

$$\beta_k \mathbf{q}_{k+1} = (H - \alpha_k)\mathbf{q}_k - \beta_{k-1}\mathbf{q}_{k-1} \tag{3.8}$$

and β_k is determined by normalization. If we denote $\mathbf{r}_k = (H - \alpha_k)\mathbf{q}_k - \beta_{k-1}\mathbf{q}_{k-1}$, we have $\beta_k = \sqrt{\mathbf{r}_k^\dagger \mathbf{r}_k}$ with $\mathbf{q}_{k+1} = \mathbf{r}_k/\beta_k$. This iterative procedure defines the core of the Lanczos procedure.

The process of generating the orthogonal basis Q as well as the tri-diagonal matrix T is called Lanczos iteration. Its algorithm can be described as follows:

Algorithm 1 Lanczos iteration

Initialize:
  $k \leftarrow 1$, $\mathbf{q}_1 =$ random vector, $\mathbf{r}_1 = \mathbf{q}_1$, $\beta_1 = 1$
while $\beta_k \neq 0$ **do**
  $\mathbf{q}_{k+1} = \mathbf{r}_k/\beta_k$
  $k \leftarrow k + 1$
  $\alpha_k \leftarrow \mathbf{q}_k^\dagger H \mathbf{q}_k$
  $\mathbf{r}_k \leftarrow (H - \alpha_k)\mathbf{q}_k - \beta_{k-1}\mathbf{q}_{k-1}$
  $\beta_k \leftarrow \sqrt{\mathbf{r}_k^\dagger \mathbf{r}_k}$
end while

So far we have only transformed H into a tri-diagonal matrix with the same dimension. To reduce the computational complexity, we can limit the number of iterations. The intuition is that, as the dimension of the Krylov space increases, it gets closer to an invariant subspace of H. We then have the approximation $Q_k^\dagger H Q_k \approx T$, where $k < n$. Clearly, the eigenvalue of Q_k can serve as an approximation of the eigenvalue of H. A formal mathematical proof concerning the convergence of the Lanczos iteration is given by the Kaniel-Paige convergence theorem [41]. The theorem states that at step k, the difference between the estimated

minimal eigenvalue $\tilde{\lambda}_0$ and the real minimal eigenvalue λ_0 is bounded by

$$\frac{\tilde{\lambda}_0 - \lambda_0}{\lambda_{\max} - \lambda_0} \leq \left(\frac{\tan(\phi)}{c_{k-1}(1+2\rho)} \right)^2, \tag{3.9}$$

where $\rho = \frac{\lambda_1 - \lambda_0}{\lambda_{\max} - \lambda_0}$, λ_1 is the second smallest eigenvalue, c_k is the Chebyshev polynomial of degree k, and $\cos\phi = \mathbf{x}_0^\dagger \mathbf{x}_0$. The Lanczos algorithm discussed in this section makes it possible to obtain the low energy eigenstates for meaningful system sizes. It is the computational kernel of our exact diagonalization implementation.

3.3 Implementation

For the results shown in this thesis and the corresponding publications, we have developed a generic exact diagonalization program. The codes are capable of diagonalizing a broad class of quantum lattice models of fermions, bosons, and spins on different lattices. While keeping the implementation as generic as possible, our implementation also uses parallel computing allowing us to solve large-size systems with up to 10^9 basis states.

Exact diagonalization programs for quantum many-body systems run into the problem of the exponential increase of the Hilbert space size with respect to the system size. The memory needed to represent the basis states and the Hamiltonian matrix will quickly exceed the capacity of a single workstation with shared memory. For example, the memory needed for various system sizes of a half filled Hubbard model on the square lattice is listed in Table 3.1. From the table we see that, even if we adopt the approach of not storing the Hamiltonian matrix, merely storing all the basis states that are needed to construct the Hamiltonian matrix will quickly exceed the memory capacity of workstations. Therefore, we have to resort to high-performance computing (HPC) clusters that use distributed memory.

# of particles	# of basis states	memory needed
8	12,870	0.1 MB
10	184,756	1.4 MB
12	2,704,156	21 MB
14	40,116,600	306 MB
16	601,080,390	4.6 GB
18	9,075,135,300	70 GB

Table 3.1: Estimated memory needed to store basis states of the half filled Hubbard model on the square lattice

There has been a considerable amount of work on large-scale exact diagonalization on HPC clusters. The protocols are based on Message Passing Interface (MPI) and high throughput and low latency communication standard such as InfiniBand. Using these methods, recent work has shown considerable progress using these implementations. For example, diagonalization of the 42-spin Heisenberg model on the kagome lattice was reported in 2011 [42]. Using improvements, diagonalization of 48 spins was reported in 2016 [43]. Recently, diagonalization of 50 spins was reported [44]. Most of these large-scale exact diagonalization implementations are tailored towards specific models to minimize the communication cost of exchanging data between different compute nodes within the cluster. Our codes, by contrast, seek to tackle a wide array of different models.

With generic implementation goals in mind, the implementation in this work uses another approach to generate the Hamiltonian matrix and store the matrix across compute nodes. Our implementation lets the mature large-scale linear algebra library handle the lower level communication. Because of its sparsity, storing the Hamiltonian matrix is actually feasible for computer clusters which typically have tens to hundreds of TB of memory. This approach provides two advantages. First, the implementation can be very generic allowing treatment of different models without modification. All the computationally intensive parts are decoupled from the model representation. This leads to the second advantage. We have the freedom

to select algorithms for the diagonalization. For example, the Krylov-Schur algorithm is capable of identifying degeneracies and is an improvement on the Lanczos algorithm that allows us to resolve topological degeneracies, thus allowing considerable speedup.

We used the large-scale linear algebra libraries PETSc [45–47] and SLEPc [48–51]. PETSc provides a high-level interface that lets users treat matrices and vectors as objects while automating communication of data between compute nodes. It also provides profiling utilities for performance tuning. SLEPc, on the other hand, provides implementation of many algorithms to solve eigenproblems based on PETSc. To incorporate these two libraries, we load the Hamiltonian matrix to PETSc. Once the matrix is loaded to PESTc, calling the SLEPc solvers on PETSc matrix objects is straightforward.

Listing 3.1 shows a code snippet for generating and storing the matrix in PETSc. PETSc provides different sparse matrix formats, the most commonly used is the compressed sparse row (CSR) format, where each process owns a subrange of rows. The generation of the Hamiltonian matrix can be carried out in parallel by each process that works on generating the rows from `row_start row_end`. And finally, we call `MatAssemblyBegin` to make each process aware of the location of rows that it does not own. For even larger matrices that cannot fit into the entire cluster memory, PETSc also provides a `ShellMatrix` interface for doing matrix-vector multiplication without actually constructing the matrix.

Listing 3.1: The code snippet for setting up the Hamiltonian matrix in PETSc

```
1
2 MatCreate(PETSC_COMM_WORLD, p_h_mat);
3 MatSetSizes(*p_h_mat, PETSC_DECIDE, PETSC_DECIDE, basis_size,
      basis_size);
4 MatSetType(*p_h_mat, MATMPIAIJ);
5 MatMPIAIJSetPreallocation(*p_h_mat, d_nz, d_nnz, o_nz, o_nnz);
```

```
6
7  PetscInt row, row_start, row_end, col;
8  MatGetOwnershipRange(*p_h_mat, &row_start, &row_end);
9
10 particles_t bsbra;
11 double coff_r, coff_l;
12 std::complex<double> coff;
13 for(row=row_start; row<row_end; ++row){
14   const particles_t& bsket = this->_basis[row];
15
16   for(begin(); ! at_end(); next()){ // for each Hamiltonian term
17     bsbra = bsket;
18     coff = act(bsbra);
19     if (0.==coff) continue;
20     col = this->_basis.index(bsbra);
21     MatSetValue(*p_h_mat, row, col, std::conj(coff), ADD_VALUES);
22   }
23 }
24 MatAssemblyBegin(*p_h_mat, MAT_FINAL_ASSEMBLY);
25 MatAssemblyEnd(*p_h_mat, MAT_FINAL_ASSEMBLY);
```

Chapter 4

Reordering fractional Chern insulators into stripes of fractional charges with long-range interactions

This chapter is taken from our publication:

Mengsu Chen, V.W. Scarola, *Reordering fractional Chern insulators into stripes of fractional charges with long-range interactions*, Physical Review B, 92, 035138 (2015). Reprinted with permission from APS.

I wrote all the code for the numerical simulation, collected data and drew all the graphs under the supervision of Prof. Scarola.

4.1 Introduction

The collective behavior of quasiparticles can lead to non-Fermi liquids that set new paradigms. The FQH regime offers one of the best known examples [52, 53]. Here uniform quantum liquids of fractionally charged quasiparticles, called composite fermions (CFs) [54], form at certain fractional Landau level (LL) fillings. Wavefunction analyses of CF exciton [55] and Cooper pair instabilities [56] show that FQH liquids transition to other intriguing quasiparticle states: crystals [57] and paired states [58], respectively. CFs have even been argued to form, much like electrons [59–61], their own stripe states [62, 63]. These studies show that some of the richness of the quasiparticle phase diagram in the FQH regime derives from the long-range part of the Coulomb interaction between electrons.

Recent work on short-range Hubbard models found an intriguing analogue of FQH states in a flat band but in the absence of a net magnetic field [64–71]. This uniform quantum liquid, the FCI, should also display its own FQH effect derived from fractionally charged quasiparticles. Refs. [72, 73] have further shown that increasing the single-particle bandwidth drives the uniform FCI state into a CDW of the original particles via nesting.

Since FCI and FQH models are adiabatically connected [74], we can understand such transitions by appealing to the two distinct CDWs considered in the FQH regime: CDWs of electrons and CDWs of CFs. CDWs of electrons at filling ν of higher LLs are well approximated by Hartree-Fock analyses in the electron degrees of freedom [59–61, 75], with, e.g., a Hartree-Fock wavefunction: ϕ_ν, dictated by the electron-electron interaction. The FCI-CDW transition found in Refs. [72, 73] is similar to transitions between FQH liquids and CDWs of electrons in higher FQH LLs [59–61]. But in lower LLs, CFs can form distinct CDWs [57, 62, 63, 76] captured by wavefunctions [54, 57, 62, 63]: $J^{2p}F_{\rho_{\mathbf{Q}}}\phi^{\mathrm{CF}}_{\nu^*}$, that are not perturbatively connected to electron CDW wavefunctions. Here the Jastrow factor J^{2p} at-

taches $2p$ vortices to each electron to yield a wavefunction at filling $\nu^*/(2p\nu^*+1)$. $\phi^{\rm CF}_{\nu^*}$ is a uniform Hartree-Fock wavefunction of CFs. Inter-CF interactions can cause CDW ordering that favors application of the density wave operator, $\rho_{\mathbf{Q}}$, in certain combinations, defined by the function $F_{\rho_{\mathbf{Q}}}$, to generate a CDW of CFs ordered at wavevector $\mathbf{Q}$ [62, 63, 76]. It is currently unknown if FCI quasiparticles can themselves form CDWs to define rich phase diagrams akin to what has been found for CFs in the lowest LL.

Stability to long-range interactions and screening defines a crucial difference between the FCI and FQH regimes. In the FQH regime, only the *short*-range part of the bare electron-electron interaction is screened, leaving a Coulomb tail [77, 78]. But if flat bands defining FCIs are to be found in materials, the basis must be defined by band structure effects (e.g., interactions in combination with multi-orbital states [73, 79]), not strong magnetic fields. The relevant FCI interaction to study is therefore a Coulomb interaction that has its *long*-range part screened. It is currently unknown if FCIs and related quasiparticle collective states are too unstable, even for screened interactions, to be found in nature. But promising work [80–82] suggests that FCIs might be robust.

In this chapter we study a screened Coulomb interaction in the FCI regime to explore stability of the quantum liquid and search for collective behavior of quasiparticles. We project a Yukawa potential, with a screening length λ, into the flat band used to define the FCI [70, 83]. We find that the FCI is surprisingly stable for λ as large as 6 lattice constants. We also find a transition to a unidirectional CDW, a stripe phase, as the screening length is increased into the Coulomb limit.

The stripe phase we find here is distinct from stripe phases of electrons normally discussed in the FQH regime in high LLs. We find that the instability to the stripe phase in the FCI Coulomb model is driven by the rearrangement of fractionally charged quasiparticles, from a uniform liquid into the stripe phase. The stripe phase we find here is akin to the stripe phases

of CFs studied in the lowest LL driven by inter-CF interactions [62, 63] and complements recent work on FCIs [84]. We show this conclusively by explicitly computing the charge of each stripe to find an exact rational fraction. Our findings have important consequences in the search for FCI physics in materials because we show that they are stable for large screening lengths and we have found at least one intriguing collective state of quasiparticles, a stripe state, derived from excitations of the FCI state.

4.2 Model

We consider a single-particle basis derived from the following model on the checkerboard lattice [83]: $\sum_{\mathbf{k},m} \psi^\dagger(\mathbf{k}) d_m(\mathbf{k}) \sigma_m \psi(\mathbf{k})$, where the fermion pseudo-spinor basis states are defined on sublattices A and B in the 2-site unit cell: $\psi(\mathbf{k}) \equiv (c_{\mathbf{k},A}, c_{\mathbf{k},B})^T$, the flat band Hamiltonian parameters are $d_1(\mathbf{k}) = 2\sqrt{2}\cos(k_x/2)\cos(k_y/2)$, $d_2(\mathbf{k}) = 2\sqrt{2}\sin(k_x/2)\sin(k_y/2)$, $d_3(\mathbf{k}) = (2-\sqrt{2})[\cos(k_x) - \cos(k_y)]$, and σ are the Pauli matrices. We work in the lowest flat band but we have checked that including a finite bandwidth does not qualitatively change the results presented below.

Recent work found numerical evidence for a gapped uniform quantum liquid at a filling of 1/3 by projecting the nearest neighbor Hubbard interaction into the lowest flat band defined by d_m [64–66]. The resulting states, in direct analogy to FQH states, demonstrate a 3-fold topological degeneracy, a fractionalized Chern number and should, in principle, exhibit a FQH effect if found in materials. The role of long-range interactions derived from the Coulomb interaction remains a key issue.

To study the interplay between screening and FCIs we consider a model defined by a Yukawa

interaction:

$$H = \mathcal{P}\frac{e^2}{2\epsilon}\sum_{i\neq i'}\frac{e^{-r_{ii'}/\lambda}}{r_{ii'}}n_i n_{i'}\mathcal{P}, \tag{4.1}$$

where the projectors $\mathcal{P}$ imply that the model acts only in the Fock space of the lowest single-particle flat band and n_i is the fermion number operator. Both $r_{ii'}$ (the inter-site separation before projection) and λ are in units of the spacing between the unit cells. We set the energy unit to $V \equiv \exp(-1/\sqrt{2}\lambda)[\sqrt{2}e^2/\epsilon]$ to ensure that the $\lambda \to 0$ limit of H reduces to the nearest neighbor interaction while $\lambda \to \infty$ reduces to the Coulomb limit. ϵ is the dielectric constant. In the following we study the eigenstates of Eq. (4.1) at $N/N_c = 1/3$ filling on a periodic $L_x \times L_y$ lattice, where N_c is the number of unit cells.

4.3 Energetics

We numerically diagonalize Eq. (4.1) using the Lanczos algorithm. We study $N = 6$, 8, 10, and 12 and present results for $L_x \times L_y = (N/2) \times 6$. We are limited to $N \leq 12$ because larger Hilbert space sizes ($\sim 1 \times 10^9$ states for $N = 12$) are prohibitive. We studied other aspect ratios and have also considered tilted periodic boundary conditions which, only for $N = 6$ at this filling, allows us to access an additional system size. In all systems studied we find uniform FCI states with the requisite 3-fold topological degeneracy and a robust gap, Δ_λ, in the nearest neighbor limit, $\lambda \to 0$. But the Coulomb limit reveals a different state.

Fig. 4.1 shows representative data for the eigenvalues of Eq. (4.1) in the Coulomb limit. Similar results were obtained for all accessible N and large λ. The 15-fold degeneracy found here stems from a 5-fold increase in the 3-fold degeneracy expected for the FCI state. In general, we find that the degeneracy increases to $3 \times L_x$ (3×2) for L_x odd (even). The degeneracies occur at wavevectors corresponding to a stripe modulation of the underlying uniform FCI

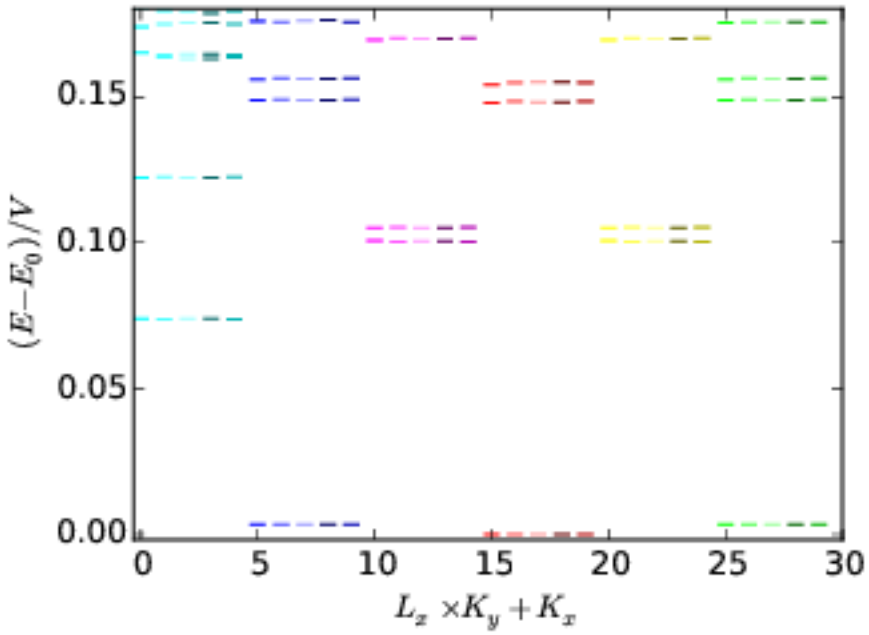

Figure 4.1: Energy spectrum of Eq. (4.1) for $N = 10$ particles for the Coulomb interaction ($\lambda = \infty$) plotted as a function of integers (K_x, K_y), where the total momentum is $2\pi(K_x/L_x, K_y/L_y)$. The ground state energy is E_0. For comparison, the FCI state occurs at $L_x \times K_y + K_x = 5, 15$, and 25 for the short range interaction. The 15-fold degenerate stripe state manifold therefore includes the states at the same wavevectors as the FCI.

states: $K_{FCI} + (n_x, 0)$, where K_{FCI} is any of the 3 topologically degenerate wavevectors of the FCI state, $n_x = 0$ and $L_x/2$ when L_x is even (i.e., when L_x an integer multiple of the stripe spacing), and $n_x = 0, 1, ..., L_x - 1$ otherwise. We discuss these degeneracies in the following sections.

The top panel of Fig. 4.2 depicts the evolution of the low energy spectrum as a function of the screening length. The low λ limit shows an FCI liquid with 3 degenerate ground states and $\Delta_\lambda > 0$ up to $\lambda \approx 6.5$ where a transition to a 15-fold degenerate state is found. We found the same transition in the regime $\lambda = 3.2 - 6.5$ for $N = 6 - 10$.

The wavevectors and persistence of the underlying 3-fold topological degeneracy of the FCI suggests that the degenerate ground states in Figs. 4.1-4.2 for $\lambda > 6.5$ are stripes of quasipar-

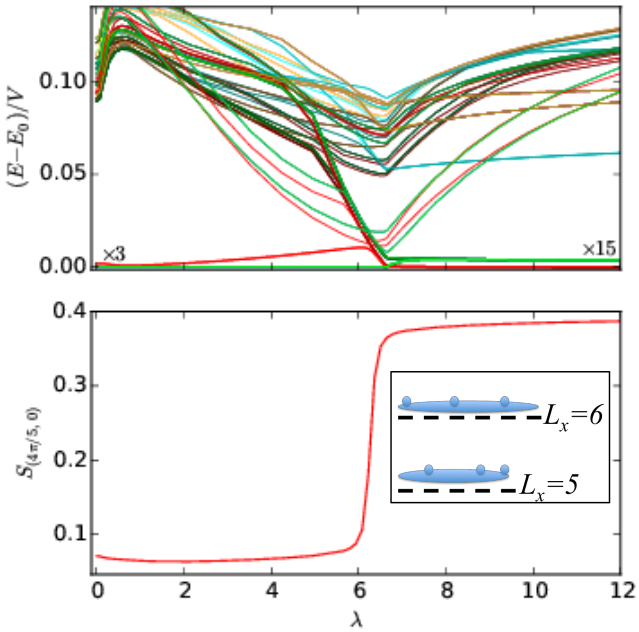

Figure 4.2: Top: Energy spectrum of Eq. (4.1) for $N = 10$ plotted as a function of the screening length. The colors correspond to the same (K_x, K_y) as in Fig. 4.1. The transition from an FCI to stripes at $\lambda \approx 6.5$ is signaled by a change in degeneracy from 3 to 15. For $\lambda \gtrsim 6.5$ each of the 3 FCI states acquire a 5-fold degeneracy. Bottom: The ground state structure factor peak plotted for the same parameters as the top panel. Inset: Schematic of a one-dimensional slice along the x-direction (perpendicular to the stripes). Spheres represent charge excess atop the uniform liquid. The $L_x = 5$ ($L_x = 6$) case fits a non-integer (integer) number of stripes and shows one of 5 (2) configurations.

ticles. To show this we first study the spatial symmetry of the charge order. We then show that the stripe states are best described as ordering of quasiparticles instead of electrons.

4.4 Stripe Order

We use the static structure factor to study the charge order:

$$S_{\mathbf{q}} = \frac{1}{N_c^2} \sum_{j,j'} e^{-i\mathbf{q}\cdot\mathbf{r}_{jj'}} \langle \tilde{n}_j \tilde{n}_{j'} \rangle, \tag{4.2}$$

where the tilde indicates projection to the lowest flat band of the single-particle Hamiltonian so that j and j' label unit cells. We have verified that the low λ side of the transition demonstrates uniform ground states, i.e., there are no peaks in $S_{\mathbf{q}}$. But in the large λ regime we find evidence for a peak at $\mathbf{q} = (\pi, 0)$ in $S_{\mathbf{q}}$ in the thermodynamic limit, i.e., stripes aligned along the y-direction. The unprojected structure factor leads to qualitatively similar results.

The bottom panel of Fig. 4.2 shows the evolution of the structure factor peak with screening length. For low λ, $S_{\mathbf{q}}$ remains at its background value until an apparently first order transition at $\lambda \approx 6.5$. (The transition softens for $N < 10$) The peak of $S_{\mathbf{q}}$ here occurs at, $(4\pi/5, 0)$ and $(6\pi/5, 0)$.

Fig. 4.3 plots the structure factor by combining data for $N = 8, 10$, and 12. The left (right) panel indicates the FCI (stripe) state. In the right panel, lattices with $N = 8$ and 12 particles show peaks at $\mathbf{q} = (\pi, 0)$, while the $N = 10$ data shows peaks at $\mathbf{q} = (4\pi/5, 0)$ and $(6\pi/5, 0)$, centered at $\mathbf{q} = (\pi, 0)$. Different system sizes allow different values for the peak. There is one peak, at $(\pi, 0)$, for L_x even and two peaks, at $((L_x \pm 1)\pi/L_x, 0)$, for L_x odd. We therefore conclude that the peak of $S_{\mathbf{q}}$ converges to $\mathbf{q} = (\pi, 0)$ for large system sizes.

$S_{\mathbf{q}}$ indicates that the ground states are uniform stripes along the y-direction spaced by two lattice constants along the x-direction. The ground state degeneracy can then be explained as the number of ways [L_x (2) for odd (even) L_x] to translate the stripes along x (perpendicular to the stripes) and obtain the same state for each of the 3 topological sectors of the FCI. The even L_x case allows stripes to occupy only two distinct sublattices whereas the L_x odd case frustrates the two-lattice constant spacing forcing an L_x degeneracy (See inset Fig. 4.2). Excited states in Fig. 4.1 then correspond to density modulation along the y-direction which have $\Delta_\lambda > 0$ in our finite-size simulation.

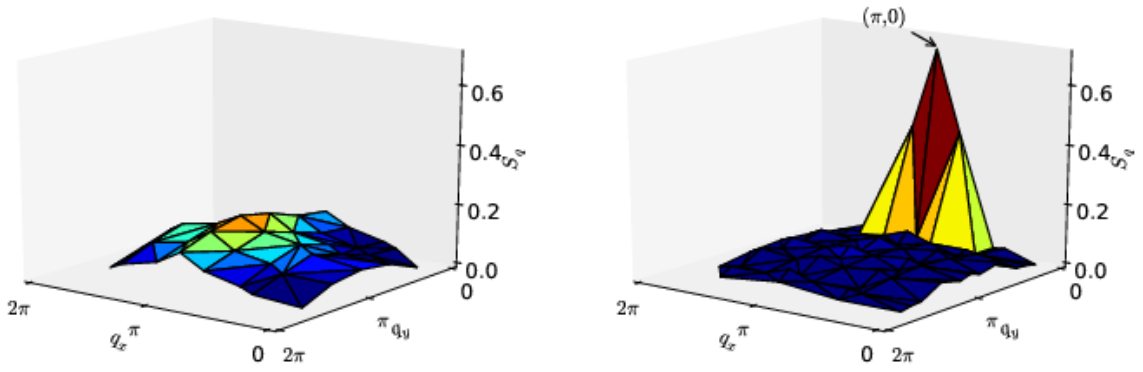

Figure 4.3: The left panel plots the ground state structure factor versus wavevector for the uniform FCI for $\lambda = 1$ in Eq. (4.1). The right panel demonstrates the formation of a stripe state for the Coulomb interaction, $\lambda = \infty$.

4.5 Fractionally Charged Quasiparticles

We find that the stripe state is a CDW of fractionally charged quasiparticles atop the otherwise uniform FCI liquid. We note that the charge of the FCI excitations is $e/3$ [66]. The charge of quasiparticle stripes must therefore be an integer multiple of $e/3$. To verify this connection we perform flux insertion [64–66] and compute the density in real space to extract the charge of each stripe.

Laughlin's gauge argument [85] points out that flux inserted along a cylinder axis induces perpendicular current on the surface. Gauge invariance implies that the periodicity with respect to the flux reveals the charge of quasiparticles because we can make the replacement $eA \to e^*A$, where A is the vector potential and e^* is the renormalized charge. An added condition, $\Delta_\lambda > 0$, allows for adiabatic spectral flow [86]. When both conditions are met they imply a quantized Hall resistance with a value dictated by the charge of the quasiparticles [85–87].

The top panel of Fig. 4.4 shows adiabatic spectral flow with respect to flux insertion in the

FCI regime but with $\lambda = 1$. Here a test flux is inserted along the x direction. The spectra (eigenstates) show Φ_0 ($3\Phi_0$) periodicity in Φ. $\Delta_\lambda > 0$ and the $3\Phi_0$ eigenstate periodicity imply a Hall conductivity quantized at 1/3. Our results therefore show that the FCI is favored for interactions with a non-zero screening length, $\lambda \lesssim 6.5$.

The bottom panel of Fig. 4.4 shows representative flux insertion data in the Coulomb limit. Here the flux pumps charge parallel to the stripes. The eigenstates of the stripe phase show a $3\Phi_0$ periodicity. Gauge invariance therefore implies that flux evolution of the ground state is consistent with stripes of quasiparticles with charge $e/3$. There also appears to be a spectral gap and adiabatic spectral flow consistent with fractionally quantized Hall conductivity in the stripe phase. Our finite-size simulations cannot rule out the possibility that the gap collapses in the thermodynamic limit due to long wavelength fluctuations in the stripe phase.

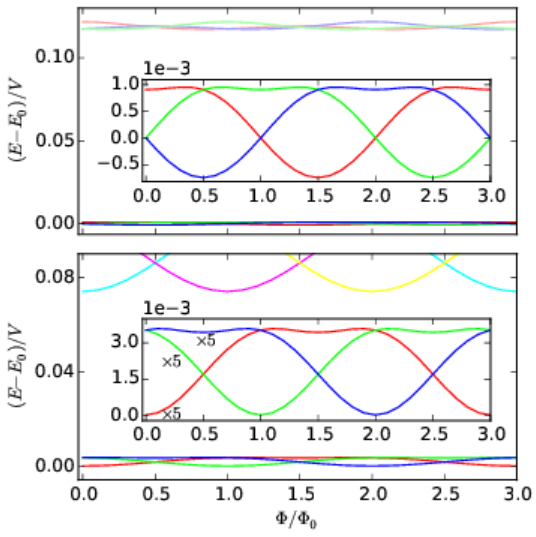

Figure 4.4: Spectral flow of the FCI ($\lambda = 1$, top panel) and stripe state ($\lambda = \infty$, bottom panel) as a function of the flux in units of $\Phi_0 = h/e$ for $N = 10$. Both panels show a Φ_0 spectral periodicity and a $3\Phi_0$ eigenstate periodicity with respect to the flux. The spectral flows are adiabatic within the ground state manifold. The insets zoom in on the ground state manifolds. The colors correspond to the same (K_x, K_y) as in Fig. 4.1.

To conclusively show that the stripes are fractionally charged quasiparticles atop an otherwise uniform state, we compute the charge of a single stripe. We add a weak symmetry breaking term to Eq. (4.1):

$$\sum_j \epsilon_j \tilde{n}_j. \tag{4.3}$$

For $\epsilon_j \ll \Delta_\lambda$ we obtained the same stripe density regardless of our choice for ϵ_j, i.e., the stripes spontaneously break the C_4 lattice symmetry. We also find that 3 of the degenerate stripe states at K_{FCI} are uniform in the single-particle density, i.e.,

$$F_{\rho_{\mathbf{Q}}} \sim 1 + \mathcal{O}(\rho^2_{\mathbf{Q}}) \tag{4.4}$$

in the wavefunction. This is in contrast to the other stripe states in the degenerate manifold showing charge modulation,

$$F_{\rho_{\mathbf{Q}}} \sim \rho_{\mathbf{Q}} + \mathcal{O}(\rho^2_{\mathbf{Q}}). \tag{4.5}$$

The inhomogeneous density allows us to compute the charge of one stripe:

$$N_{qp} e^*/e = \sum_{j \in R} \langle \tilde{n}_j - \rho_0 \rangle, \tag{4.6}$$

where N_{qp} is the number of quasiparticles, $\rho_0 = 1/3$ is the density of the uniform liquid, and the region R defines summation over a single stripe by choosing j's such that $\langle \tilde{n}_j \rangle > \rho_0$. For the uniform stripes studied here this condition implies that we sum over the entire stripe. We find $N_{qp} e^*/e$ to be a multiple of $1/3$ within numerical accuracy for all system sizes studied by computing the charge within the subspace of stripe states showing charge modulation. For example, for $N = 8$ we find $N_{qp} e^*/e = 4/3$. Since the FCI quasiparticles have charge $1/3$ it is natural to conclude that we have $N_p = 4$ and $e^*/e = 1/3$. We have tested that this results is robust against different choices for ϵ_j. We have therefore found that increasing λ

orders quasiparticles atop the otherwise uniform liquid into stripes.

4.6 Constraints on Effective Theories

Constraints on effective theories illustrate the difference between CDWs of electrons and CDWs of quasiparticles. A minimal effective model must reproduce the lowest energies and momenta. Truncation of Eq. (4.1) does not accomplish this. For example, a classical model derived by dropping off-diagonal terms in Eq. (4.1), $H_{\rm c}$, leads to a non-degenerate CDW in the ground state, e.g., at $(K_x, K_y) = (2, 4)$ for N=8. Adding the largest off-diagonal terms: $\tilde{c}^{\dagger}_{x,y}\tilde{n}_{x,y\pm1}\tilde{c}_{x\pm1,y} + h.c.$, to $H_{\rm c}$, leads to a CDW with degeneracies and momentum sectors that are very different from the full model.

An effective theory of quasiparticles must also satisfy an exact constraint of fractional charge. Consider, for example, an effective model built from anisotropic hopping and interaction terms: $-t\sum_{\langle j,j'\rangle}|\hat{r}_{j,j'}\cdot\hat{y}|(\tilde{c}^{\dagger}_{j}\tilde{c}_{j'} + h.c.) + \sum_{j\neq j'}(1 - c|\hat{r}_{j,j'}\cdot\hat{y}|)\tilde{n}_j\tilde{n}_j/(2r_{jj'})$, where t and $c < 1$ are fitting parameters and $\hat{r}_{j,j'}$ and $\hat{y}$ are unit vectors. For large c this theory can be thought of a as weakly coupled Luttinger liquid [88]. We have checked that the low energy states of this model do not order at the same wavevectors as Eq. (4.1). But more importantly, the stripes defined this way can be fractionalized at *any* value. The effective theory must also define an array of FCI quasiparticles with a charge that is a rational fraction [89–92].

4.7 Summary

We tested a model of FCIs that includes *a priori* screening of the underlying Coulomb interaction. Adiabatic flux insertion shows that the FCI survives for sizable screening lengths. The perseverance of the FCI state (and its quasiparticles) allowed a transition to an intriguing

stripe phase of fractionally charged quasiparticles. Our results show that some of the rich structure considered in the FQH regime, e.g., stripes of quasiparticles, manifests in the FCI regime.

Chapter 5

Quantum anomalous Hall state from spatially decaying interactions on the decorated honeycomb lattice

This chapter is taken from our publication:

Mengsu Chen, Hoi Hui, Sumanta Tewari, V.W. Scarola, *Quantum anomalous Hall state from spatially decaying interactions on the decorated honeycomb lattice*, Physical Review B, 97, 035114 (2018). Reprinted with permission from APS.

I produced the exact diagonalization results. Dr. Hoi Hui produced the mean field theory results. We worked together under the supervision of Prof. Scarola and Prof. Tewari.

5.1 Introduction

Topological insulators (TI) are an exotic state of quantum matter distinguished from ordinary band insulators by the presence of topologically protected edge states [93, 94]. While the bulk spectrum of TIs is gapped, the gapless edge (2D) and surface (3D) states remain conducting as long as time reversal symmetry (TRS) remains unbroken. In addition to TRS-protected TIs, topological states can also occur in TRS-broken systems. The quantum anomalous Hall (QAH) insulator is one such state in which Hall resistance, defined by the voltage across the transverse direction divided by a longitudinal current, can be non-zero and quantized as a result of broken TRS [95]. In these cases the topological states of matter are characterized by a $\mathcal{Z}_2$ invariant (TI) and a $\mathcal{Z}$ invariant or Chern number (QAH). For non-trivial values of the invariants, the topological properties are controlled by the band inversion phenomena and are essentially encoded at the level of the band structure, while the role of inter-particle interactions is minimal.

It has been realized that an alternative route to topological phenomena may be driven exclusively by interparticle interactions [96, 97]. The possibility of realizing interaction-generated topological states of matter in the charge sector – known as topological Mott insulators [98] –even when the non-interacting band structure is topologically trivial, can greatly expand the availability of topologically non-trivial systems, and is thus of paramount importance.

Noninteracting electronic systems in which the Fermi surface shrinks to a discrete number of Fermi points is an emerging frontier in condensed matter physics. A number of proposals have been recently put forward where QAH states are induced in mean field theory (MFT) purely by interactions in a model of band structure with Fermi points, TRS, and trivial band topology [98, 99]. Such states have been proposed to appear from interactions leading

to microscopic loop currents and spontaneous breakdown of TRS [82, 98–106, 106–119]. However, in the most common example of Fermi points–Dirac points with emerging low energy relativistic invariance as in graphene–MFT and numerical techniques such as exact diagonalization (ED) and density matrix renormalization group fail to agree thus casting doubt on the existence of interaction-induced spontaneous QAH ground state as the true ground state [98, 102, 109–111, 113, 115, 116, 120–123]. But according to these calculations, the key condition for the emergence of the QAH state (if at all) is that second and/or third nearest neighbor repulsive interactions need to be equal to or larger than nearest-neighbor repulsion, or having long-range hopping with direction-dependent phases in the hopping amplitudes [100, 119]. Both of these conditions are difficult to achieve [Ref. [124] proposes that the Ruderman-Kittel-Kasuya-Yosida (RKKY) interaction could offer a workaround for the former condition].

Most MFT studies find that non-spatially decaying interactions are important for establishing the QAH phase but there are exceptions. Studies of spinless fermions on certain lattices with a quadratic band crossing point (QBCP) as the non-interacting Fermi surface offer a different starting point [99–101, 114]. One example, mentioned above, is the checkerboard lattice [100]. An ED study [119] found a QAH phase arising from spatially decaying interactions but anisotropic hopping and equal hopping amplitude for different sublattices were needed to stabilize the phase [119]. MFT studies on a different lattice with a QBCP, a decorated honeycomb (or star) lattice, indicate that spatially decaying interactions might support a robust QAH phase [99] even with just nearest-neighbor interactions. But MFT is notoriously susceptible to quantum fluctuations that can significantly impact phase diagrams. Therefore the realizability of the QAH phase from spatially decaying interactions on the decorated honeycomb lattice remains an open issue.

In this chapter, we investigate the prospect of generating interaction-driven QAH states

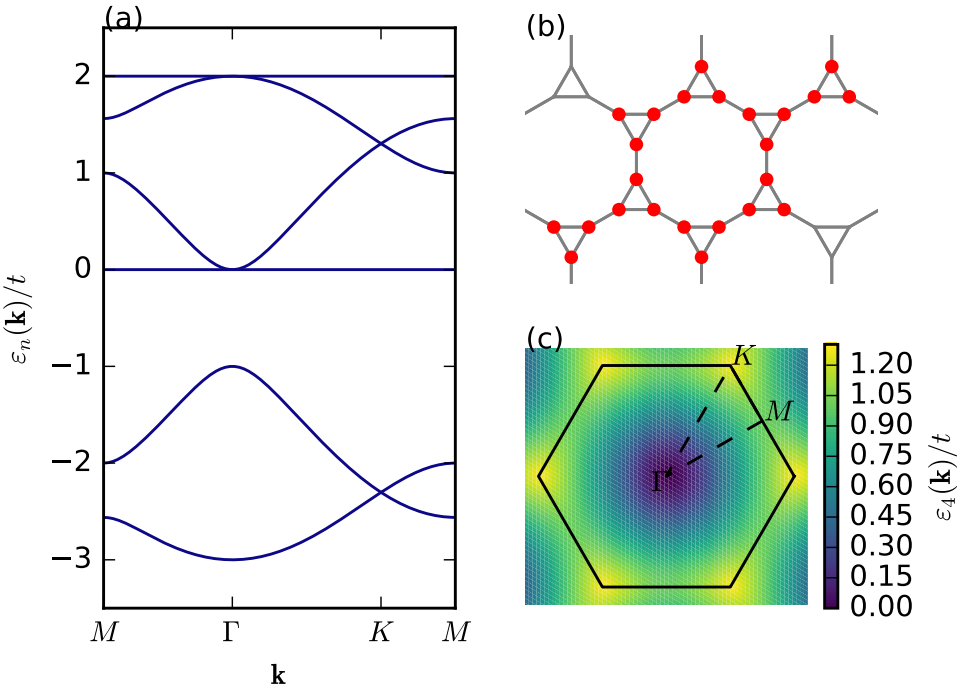

Figure 5.1: (a) Band structure along the high-symmetry path $M \to \Gamma \to K \to M$ [dashed line in Fig. (c)] in the first Brillouin zone. (b) The decorated honeycomb lattice and the 24-site cluster (red dots) studied by exact diagonalization. (c) The first Brillouin zone of the decorated honeycomb lattice and the band (color map) right above the Fermi point (a QBCP).

on a decorated honeycomb lattice at half filling. Our principal objective is to investigate if the QAH state occurs for physically realizable interaction parameters that can be used to model realistic systems, e.g., electrons in solids or dipolar fermions in optical lattices. We present ED results which incorporate quantum fluctuations but are applicable only to small system sizes, as well as mean-field results [99] which are approximate (could not capture quantum fluctuations) but can handle the system in the thermodynamic limit. The complementary nature of the two approaches, coupled with qualitatively very similar phase diagrams obtained from both of them, gives us confidence about the reliability of our calculations. Remarkably, in both ED and MFT, we find that a QAH state occurs on the decorated honeycomb lattice at the QBCP, for interaction parameters that *progressively decrease with*

separation. The agreement between MFT and ED implies that quantum fluctuations allow a robust QAH phase in this lattice. Our work sets the stage for observations of QAH under realistic conditions of spatially decaying interactions.

This chapter is organized as follows. In Sec. 5.2 we present the model of interacting fermions on a decorated honeycomb lattice. We also review the complementary methods used to solve the model: numerical ED and a MFT obtained from the Hartree-Fock approximation. In Section 5.3 we present the phase diagram obtained from both methods. Here we show that both methods agree at weak to moderate interaction strengths. Sec. 5.6 and 5.7 discuss, respectively, the uniform QAH phase and the CDWs found from both methods. We summarize by discussing possible connections to materials and ultracold atom gas experiments in Sec. 5.8.

5.2 Model and methods

We consider a tight-binding Hamiltonian,

$$H = -t \sum_{\langle i,j \rangle} c_i^\dagger c_j + V_1 \sum_{\langle i,j \rangle} n_i n_j + V_2 \sum_{\langle\langle i,j \rangle\rangle} n_i n_j, \tag{5.1}$$

where $c_i^\dagger$ creates a spinless fermion on site i. The summation is over nearest- ($\langle i,j \rangle$) or next-nearest- ($\langle\langle i,j \rangle\rangle$) neighbors on a decorated honeycomb lattice [Fig. 5.1(b)]. Henceforth we consider $V_1, V_2 \geq 0$ and set $t = 1$ as the energy scale.

Fig. 5.1(a) shows the non-interacting band structure of Eq. (5.1). At 1/2 or 5/6 filling ratios, the Fermi surface shows a QBCP at the Γ point, which is an important component to realizing a QAH ground state. For definiteness we focus on half-filling.

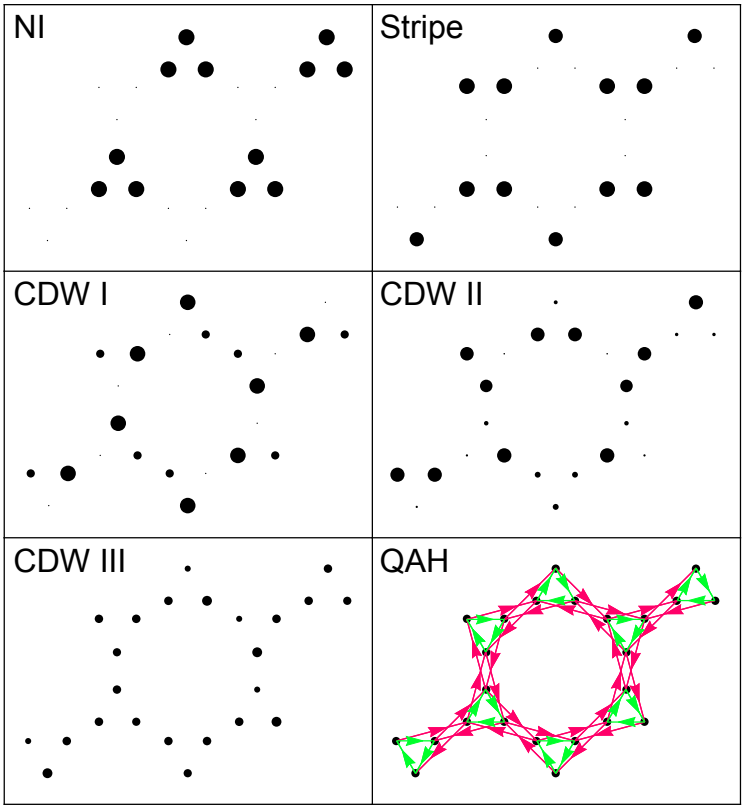

Figure 5.2: Density patterns for the Nematic Insulator (NI), Stripe, and Charge Density Waves (CDWs). The QAH pattern draws bond currents computed with arrows indicating the direction of the currents $\mathrm{Im}\langle c_i^\dagger c_j\rangle$. All plots are the result of mean field calculations but exact diagonalization produced the same configurations where comparisons could be made (see Sec. 5.5).

To study the phase diagram where the hopping strength is on the order of the interaction strength we use two complementary methods. We employ a modified Arnolidi algorithm (the Krylov-Schur algorithm [125]) which allows study of large sparse matrices with degenerate eigenvalues. We refer to application of this method as ED because it is unbiased and gives the same results as other unbiased methods on small lattices. With ED we work on a finite system size ($N_e = 12$ fermions on 24 sites, i.e., 2×2 unit cells). ED yields the lowest energy states and includes all interaction terms without approximation.

We use periodic boundaries. Periodic boundary conditions are widely used to study bulk

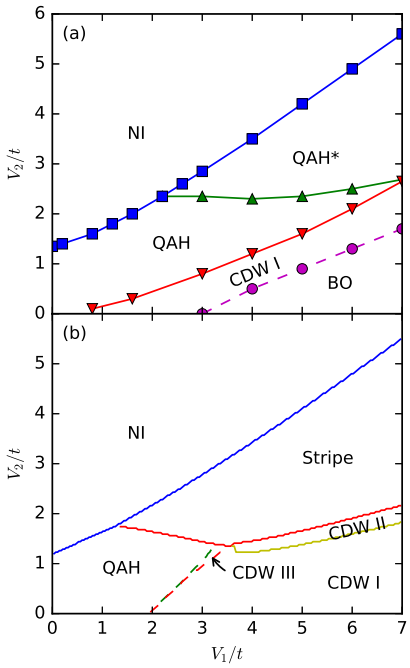

Figure 5.3: (a) Phase diagram obtained using exact diagonalization on Eq. (5.1). The symbols are results from calculations and the lines are a guide to the eye. The bond ordered (BO) phase is an uniform phase that results from the superposition of bond-ordered crystal configurations (see Sec. 5.7). (b) The same as (a) but the lines plot transitions obtained from self-consistent mean field theory on an infinite lattice. The dashed lines indicate second order phase transitions. The agreement between panels (a) and (b) shows strong evidence for a robust QAH phase. The QAH order appears to survive in non-interacting limits near the origin but here the QAH gap vanishes asymptotically with interaction strength.

properties by eliminating boundary effects [116, 118, 119]. Prior work has found that boundary effects could produce level crossings that are not related to topological transitions [116]. We use periodic boundary conditions to avoid possible artificial phase transitions and minimize finite size effects.

We also employ MFT on an infinite lattice to complement the results of ED which is limited

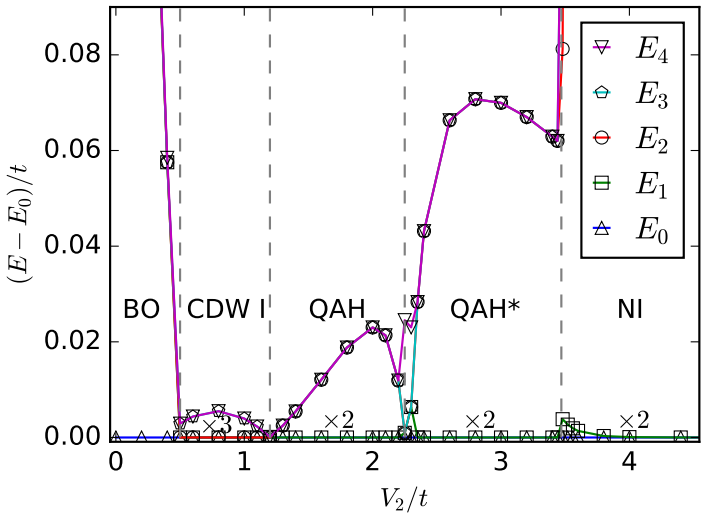

Figure 5.4: Exact diagonalization calculation of the lowest 5 energies as a function of V_2 for $V_1 = 4$. The vertical dashed lines mark phase transitions determined by level crossings and order parameters. The numbers after '×' label the ground state degeneracy.

to a small lattice. MFT first decouples the interaction terms as:

$$\begin{aligned} n_i n_j \quad \rightarrow \quad & n_i \langle n_j \rangle + \langle n_i \rangle n_j - \langle n_i \rangle \langle n_j \rangle - c_i^\dagger c_j \left\langle c_j^\dagger c_i \right\rangle \\ & - \left\langle c_i^\dagger c_j \right\rangle c_j^\dagger c_i + \left\langle c_i^\dagger c_j \right\rangle \left\langle c_j^\dagger c_i \right\rangle , \end{aligned} \tag{5.2}$$

and then follows with a self-consistent computation of $\langle c_i^\dagger c_j \rangle$ with the same unit cell as ED but on an infinite lattice (see Sec. 5.4 for details). With our chosen unit cell of 24 sites, there are 108 independent values of $\langle c_i^\dagger c_j \rangle$ which need to be self-consistently solved.

5.3 Phase diagram

Extreme limits of the phase diagram can be computed very precisely. For infinitely large interaction strengths the phases of Eq. (5.1) are classical states that spontaneously break spatial lattice symmetries. For $V_1 \rightarrow \infty$ a degenerate manifold of classical states that avoid

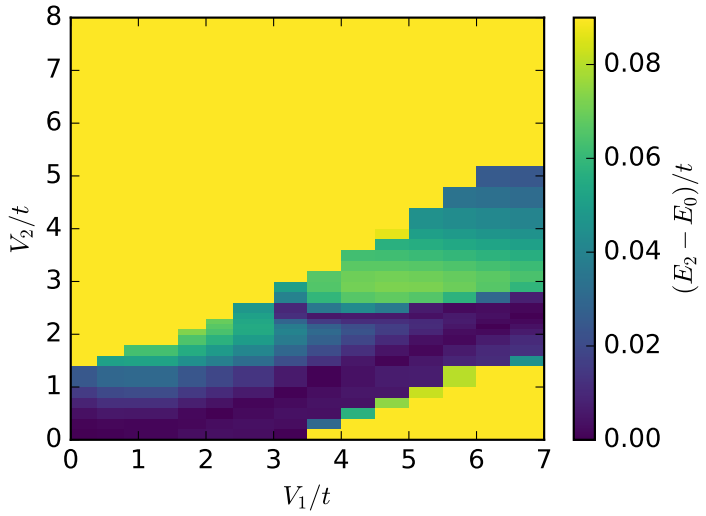

Figure 5.5: Energy gap, $E_2 - E_0$, obtained from exact diagonalization, where E_0 is the lowest energy level, and E_2 is the third lowest level. (The second level, E_1, is always degenerate with E_0 within the QAH phase.) The gapped QAH and QAH* phases are separated by a nearly horizontal gap-closing line. The QAH gap also closes along the axes.

nearest neighbor pairs forms. For $V_2 \to \infty$ the lowest energy ground state at half filling is a nematic insulator (NI) which avoids forming next-nearest neighbor pairs. For $V_1 \sim V_2 \to \infty$ a stripe phase sets in. Fig. 5.2 depicts the charge configurations of the NI and stripe phases. We have checked that both ED and MFT give the same ground states for infinitely large interaction strengths. These and other classical phases compete with the uniform QAH phase as the interaction energies are lowered to be on the order of t.

We expect quantum phases when energy scales compete, i.e., $t \sim V_1 \sim V_2$. Fig. 5.3 shows our central result, the phase diagrams obtained by both ED and MFT in this regime. We see qualitative agreement between both methods in several parts of the phase diagram. Most importantly, we see that the QAH phase arises for nearly the same parameters in both ED and MFT. For example, in the limit of $V_1 \to 0$, both ED and MFT find QAH for $V_2 < 1.2t$ and NI for $V_2 > 1.2t$. We now discuss important aspects of these phases and our method for obtaining the phase boundaries.

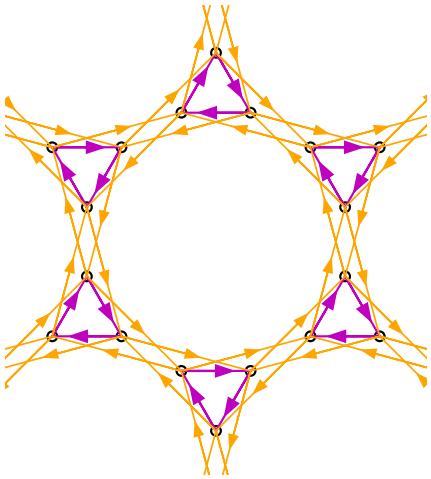

Figure 5.6: Bond currents computed from exact diagonalization on one of the two QAH states at $V_1 = 4$ and $V_2 = 3$. Arrows indicate the direction of the bond currents $\mathrm{Im}\langle c_i^\dagger c_j \rangle$, in agreement with mean field results plotted in Fig. 2 of the main text.

5.4 Mean-field theory calculation

The goal of the MFT is to approximate the many-body state by a state with non-interacting particles. Consider the set of all possible states formed by non-interacting fermions only. To compute the energy $\langle H \rangle$, we need to compute the expectation value of the interaction terms, each with four operators. Since non-interacting fermions are Gaussian states, Wick's theorem can be used to compute those four-operator terms, which leads to the decomposition presented in Eq. 5.2 in the main text.

The self-consistent approach we adopt initializes the correlations $\langle c_i^\dagger c_j \rangle$ randomly. Then, at each iteration, the correlations are updated with the ground state of the resulting Hamiltonian. This process is iterated until convergence.

5.5 Exact diagonalization calculation

Within ED ground states are often degenerate. Within the QAH phase arbitrary superpositions of the time reversal pairs of QAH states appear to prevent us from directly computing currents. But we can compute current by solving for a superposition of the two degenerate ground states which maximizes the expectation value of the current operator.

We consider the current $J_{\alpha\beta} = \langle\Psi_\alpha|\hat{J}|\Psi_\beta\rangle$ and denote by $|\Psi_{A/B}\rangle$ the pair of degenerate ground states. In this subspace we compute the 2×2 matrix $J_{\alpha\beta}$. Since $\hat{J}$ anticommutes with the time-reversal operator $\mathcal{T}$ and $\mathcal{T}|\Psi_A\rangle = |\Psi_B\rangle$, it is straightforward to show that the two eigenvalues of $J_{\alpha\beta}$ are $\pm\lambda_J$ and their eigenstates are also time-reversal pairs. Taking one of the eigenstates and computing is current pattern and magnitude, we find qualitative agreement with that obtained from MFT. Fig. 5.6 shows the results from an ED calculation of the current patterns for the QAH phase which agrees with MFT patterns presented in Fig. 2 of the main text.

To demonstrate the adequacy of λ_J as an order parameter in the QAH phase, the top panel of Fig. 5.7 plots λ_J against V_1 along the $V_1 = V_2$ line. We see a sharp transition from finite and stable values of λ_J to $\lambda_J = 0$ at around $V_1 = V_2 \approx 2.7$, indicative of a phase transition.

In the case of ED with multiple degenerate ground states we can apply a similar method to compute δn. It is computed as the difference between the maximum and minimum eigenvalues of the matrix of a single-site number operator acting on the ground state subspace, similar to the procedure of computing λ_J. As an example, we plot this order parameter along a transition line from QAH to NI in the bottom panel of Fig. 5.7. The jump in the order parameter is at the same location as the jump in QAH order parameter, consistent with the QAH-NI transition. On the QAH side of the transition, we also find nonzero bond current for the eigenvectors of the single-site number operator on ground state subspace,

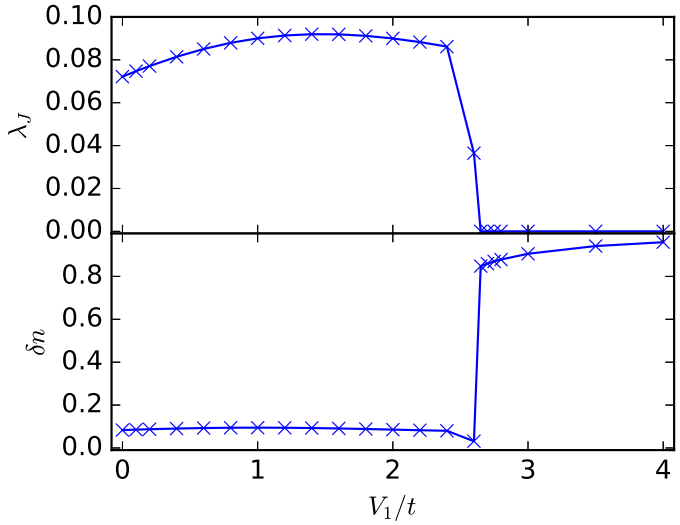

Figure 5.7: Top: Exact diagonalization calculation of the QAH order parameter measuring loop current as a function of interactions strength with $V_1 = V_2$. The sudden vanishing of λ_J indicates a transition from QAH ($\lambda_J \neq 0$) to CDW ($\lambda_J = 0$) along the $V_1 = V_2$ line in the phase diagram. Bottom: The same but for the CDW order parameter measuring the maximum density difference to show a phase transition from QAH (uniform, $\delta n = 0$) to CDW (nonuniform, $\delta n > 0$) along the $V_1 = V_2$ line in the phase diagram.

and uniform density for the eigenvectors of current operator on ground state subspace. This indicates the stability of QAH under the time reversal invariant perturbation.

5.6 Quantum anomalous Hall phase

The QAH phase has uniform density and is gapped in the bulk. It can carry current along its edge. Although the ground state is two-fold degenerate (one state for each direction of current flow) it spontaneously breaks TRS so that only one direction of edge current is chosen for arbitrarily small perturbations. The QAH state is therefore a topological phase with a definite Chern number and should reveal quantized Hall resistance.

At small (but non-zero) interaction strengths, both ED and MFT predict the existence of

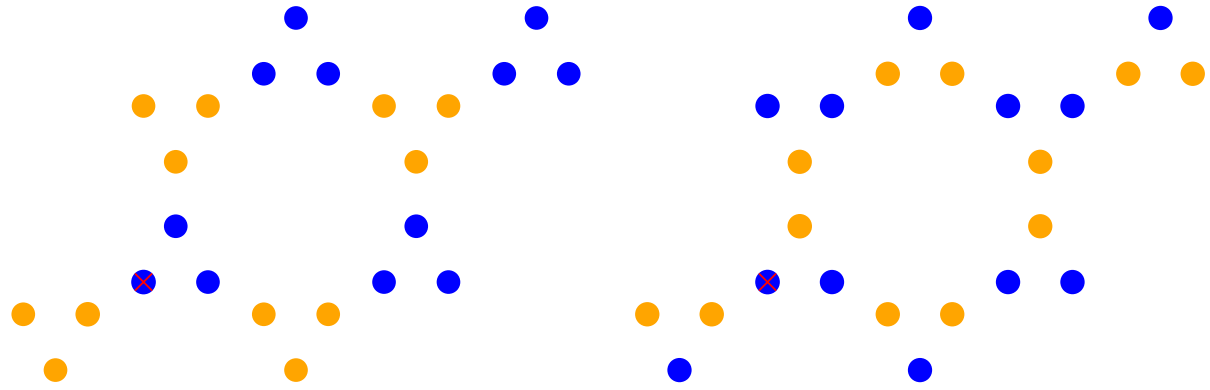

Figure 5.8: Left: The density-density correlations, $\langle n_i n_j \rangle - \langle n_i \rangle \langle n_j \rangle$, obtained from exact diagonalization and plotted as a function of the position of site j for the NI at $V_1 = 0.8$ and $V_2 = 2.4$, where the size of the dots represents the magnitude of the correlation and blue (orange) indicates positive (negative) sign. The reference site at i is indicated by a red cross. The NI breaks C_6 rotation symmetry down to C_3, while preserving translational symmetry. Right: The same but for the stripe phase at $V_1 = 20$ and $V_2 = 14$. The stripe phase breaks translational symmetry by doubling the unit cell along the direction of unit vectors.

a QAH state. Since these methods make distinct approximations, we take the qualitative agreement between the results as definitive evidence for the presence of a QAH state (even for decaying interactions, $V_1 > V_2$). To find the QAH phase we compute local currents:

$$J_{ij} = i(\langle c_i^\dagger c_j \rangle - \langle c_j^\dagger c_i \rangle), \tag{5.3}$$

that can be non-zero only in a phase with spontaneously broken TRS. Fig. 5.2 shows the current pattern in the QAH phase found using both methods.

At first glance, ED should not be able to detect QAH phase since each of the two ground states obtained numerically are arbitrary superpositions of the time reversal pair of QAH states. To reveal broken TRS we use the two degenerate ground states to compute a loop

current in ED:

$$\hat{J} = \sum_{i,j \in \text{loop}} \hat{J}_{ij}, \tag{5.4}$$

where the summation is over a closed loop of sites, e.g., a small triangle. We then compute the local current pattern that maximizes $\langle \hat{J} \rangle$ (see Sec. 5.5).

Interestingly, ED and MFT disagree at moderate values of the interaction. Fig. 5.4 shows that ED finds a second QAH phase (QAH*) separated from QAH by a gap closing indicative of a phase transition. This phase is absent in the MFT calculations. The QAH* phase is characterized by the same current pattern but in the opposite direction. Fig. 5.5 shows ED results for the energy difference between one of the degenerate ground states and the next highest energy state. Here we see that the QAH gap vanishes as the interactions (either V_1 or V_2) vanish near the origin and at the transition between QAH and QAH*.

The existence of a gap and chiral currents in the QAH phases implies that the Chern number is well defined in both MFT and ED. In the QAH phase we can rely on a finite angular momentum in the gapped ground state to define a Chern number directly because the QAH state is adiabatically connected to the non-interacting limit [99, 126].

5.7 Spontaneous spatial-symmetry breaking phases

Moving parameters away from the QAH regime, we find topological phase transitions to conventional phases that spontaneously break spatial symmetries. We detect these phases using density and density-density correlation functions to reveal long-range spatial order in the density. We find that the current vanishes in all density-ordered phases.

To capture the transition from the uniform QAH liquid to the spontaneous spatial-symmetry breaking phases we define the maximum density difference, $\delta n = \max_i \langle n_i \rangle - \min_i \langle n_i \rangle$, which

detects density modulation. The phase boundaries between CDW phases, and that of the QAH uniform phase, can be identified as a sudden jump in δn (see Sec. 5.5). The dashed lines in the bottom panel of Fig. 5.3 show second order transitions found within MFT. In the case of ED with degenerate ground states, δn is computed as the difference between the maximum and minimum eigenvalues of the matrix of a single-site number operator on the ground state subspace. Similar transitions were found with ED. In particular, the QAH-NI phase boundary computed using ED and MFT gives very close agreement.

We also use density-density correlations, $\langle n_i n_j \rangle - \langle n_i \rangle \langle n_j \rangle$, to reveal long range correlation, particularly to identify transitions to the NI phase. Fig. 5.8 plots the density-density correlation function for the NI and stripe phases obtained from ED. Here we see agreement with the MFT calculation plotted in Fig. 2. In the NI phase the energy spectrum obtained from ED shows a two-fold degenerate ground state. The two-fold degeneracy originates from the symmetry breaking of C_6 rotation symmetry in the Hamiltonian down to the C_3 symmetry in the NI ground state.

At large interactions strengths ($V_1 \sim V_2 \gg 1$) both ED and MFT show a stripe phase. The stripe phase breaks translation symmetry by doubling the unit cell along the direction of one primitive vector. It also breaks C_6 rotational symmetry to C_2. Therefore, the ground state degeneracy should be $2 \times 3 = 6$ fold. The energy spectrum from ED does show a 6-fold degeneracy and a stripe pattern in the density but the comparison between MFT and ED breaks down for $V_1 \sim V_2 \sim 1$, as shown in Fig. 5.3.

There are differences between the MFT and ED phase diagrams. ED imposes finite size effects, while MFT ignores precise treatment of quantum fluctuations. As a result of these differences MFT favors a stripe phase while ED finds the QAH* phase for $V_1 \sim V_2 \sim 3$. Both methods return to agreement for $V_1 \sim V_2 \gg 1$.

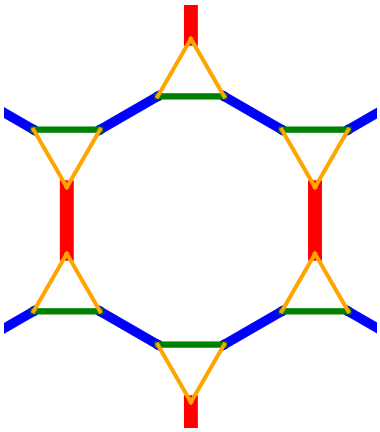

Figure 5.9: Bond average $\left\langle c_i^\dagger c_j \right\rangle$ computed using exact diagonalization for an excitation of the BO phase at $V_1 = 5$ and $V_2 = 0.2$, where the bond averages are always real. The width of the line along a bond indicates the magnitude of the average and bonds with the same color have the same magnitude. This BO crystal excitation breaks rotational symmetry, but preserves translational symmetry.

The most striking difference arises for $V_2 \to 0$ and $V_1 \sim 5$. Here MFT predicts a CDW I phase while ED finds a BO phase. Within ED, the ground state here is non-degenerate and uniform with a massively degenerate excitation space. We also find no currents in the ground state. An example bond-average pattern for one of the excitations is shown in Fig. 5.9. Here we see that certain bonds have large tunneling but others are near zero. A particle and hole form a bonding state along these bonds.

We interpret the uniform ground state as a unique superposition of excitations of the type depicted in Fig. 5.9. The gap between the ground and excited states is near t. We therefore conclude that tunneling superposes these excitations into a uniform BO state.

So, in the BO regime we find a uniform state with excitations that superpose a particle and hole along certain bonds of the hexagon separately. The resulting excitations are BO crystals. But in the ground state the hopping superposes these crystals to form a uniform state, the BO phase. Further work will include quantum fluctuations above MFT to see

if the BO phase is favored over the CDW I in the thermodynamic limit. For $V_2 \to 0$ and $V_1 \to \infty$ the BO gap vanished and the ED ground states becomes massively degenerate at an energy that agrees with MFT.

5.8 Summary

Topological phases typically encode effects of topology at the level of band structure through the band inversion phenomena. The effects of interactions in topological insulators are usually considered to be minimal. Here we instead consider spinless fermions on the decorated honeycomb lattice with the Fermi surface tuned to a quadratic band touching point which is topologically trivial. Using the complementary methods of MFT and ED we show that the QBCP on the decorated honeycomb lattice is unstable to short range interactions and produces a QAH phase with spontaneously broken TRS driven exclusively by interactions. The interaction-driven QAH phase survives quantum fluctuations while arising from spatially decaying interactions.

The model considered here can serve as a toy model for certain systems. We note that this lattice structure has been realized in Iron(III) acetate [127] and discussed in the context of $Mo_3S_7(dmit)_3$ [128, 129]. Electrons in these materials can, in principle, be polarized to be spinless fermions discussed in this work. Evaluation of a possible mechanism of polarization (e.g., g-factor engineering or ferromagnetic exchange coupling) is beyond the scope of the present work. The decorated honeycomb lattice can also be generated in optical lattices via three groups of lasers intersecting at equal angles, with each group containing three frequencies.

Spatially decaying interactions are an important criterion for realistic modeling with electrons in solids or dipoles in optical lattices. Our results therefore set the stage for realizing

interaction-driven QAH and related topological states such as chiral spin liquids [97, 108] in optical lattices with physically realizable spatially decaying interactions.

Chapter 6

Stability of Emergent Kinetics in Optical Lattices with Artificial Spin-Orbit Coupling

This chapter is taken from our publication:

Mengsu Chen, V.W. Scarola, *Stability of Emergent Kinetics in Optical Lattices with Artificial Spin-Orbit Coupling*, Physical Review A, 94, 043601 (2016). Reprinted with permission from APS.

I wrote all the code for the numerical simulation, collected data and drew all the graphs under the supervision of Prof. Scarola.

6.1 Introduction

Precise control over the band structure of ultracold atoms and molecules placed in optical lattices enables access to strongly correlated states [130–132]. Recent work shows that optical lattices allow further exploration of extreme regimes of strong correlation where the single-particle dispersion can be flattened to emphasize interactions, much like the lowest Landau level in the fractional quantum Hall regime [133]. Examples in the optical lattice

context include flat single-particle bands in triangular [134, 135], honeycomb [136–138], and kagome [70, 134, 139] optical lattices. Another example includes flat bands generated from artificial spin-orbit coupling (SOC) [140–146] in one dimensional chains [147] and the two dimensional square lattice [148]. In all of these cases, there is an opportunity for emphasized interaction effects to lead to emergent physics wherein interactions operating within the flat band generate entanglement, as in the fractional quantum Hall regime [54, 76, 149].

In general, interacting flat band models are captured by two distinct classes of Hamiltonian that lead to either quantum or classical states [148]. Classical flat band models are defined by only diagonal interaction terms in a site basis. They are trivial and exhibit only classical (unentangled) configurations of particles in the absence of kinetics because the single-particle basis states are highly localized and cannot overlap via interactions. Examples of classical flat band problems include basic Hubbard models [130] of atoms in very deep optical lattices without applied fields. But in quantum flat band models, interactions are off-diagonal in a site basis and entangle particles even in the absence of any dispersive single-particle bands because the single-particle basis states are only quasi-localized and can effectively overlap via interactions. Recent work showed that flat SOC bands in optical lattices define quantum flat bands [148, 150].

Recent work [150] modeling fermions in one dimensional optical lattices with a quantum flat band defined by SOC shows that they can be described with an emergent Luttinger liquid theory [134, 150] that contrasts with ordinary Luttinger liquid theory [151–154]. In an emergent Luttinger liquid the fermions experience an effective band (generated entirely by interactions) in which Luttinger liquid-like properties appear from the interaction alone. The emergent Luttinger liquid theory (and numerical diagonalization) showed that the ground state of the system is a Wigner crystal of spinors. The low energy excitations of the crystal displayed emergent kinetics and fractionalized charge. The ground and excited states

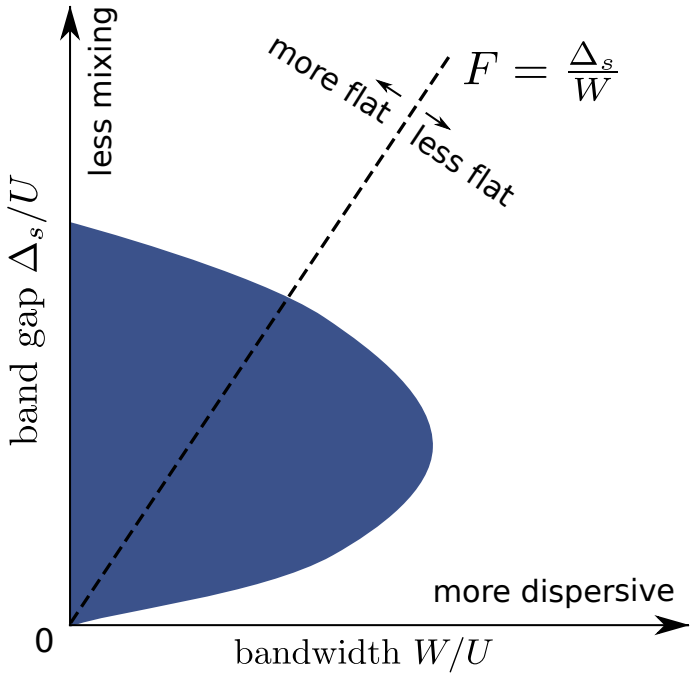

Figure 6.1: Schematic plotting the stability of the Wigner crystal phase (lobe) in the parameter space of single-particle band gap versus bandwidth. F defines the flatness ratio. Increasing the single-particle bandwidth makes the single-particle band more dispersive whereas increasing the single-particle band gap suppresses band mixing between the partially filled lower band and the upper band. $W \to 0$ corresponds to a perfectly flat band and $\Delta_s \to \infty$ leads to a single band at low filling, a limit discussed in Ref. [150]. The work presented here considers a more physical model with experimentally realistic numbers for W and Δ_s. The lobe shows that the Wigner crystal with emergent Luttinger liquid properties found in the approximate model of Ref. [150] remains stable and is adiabatically connected to the Wigner crystal in the physical model considered here.

stemmed from just the s-wave interaction that was effectively extended in range because the single-particle basis states (Wannier functions) where elongated.

In this work we build on the results of Ref. [150] to model a more realistic Hamiltonian to test the robustness of the emergent Luttinger liquid properties. Ref. [150] made a flat band approximation which assumed zero single-particle bandwidth. It was argued that a small dispersion would not impact the essential properties of the states found in Ref. [150]. Furthermore, a single band was assumed thereby explicitly ruling out the possibility that

band mixing would qualitatively change the nature of the states found. The realistic model we consider here systematically includes both effects (non-zero bandwidth and band mixing from a second band) to explore the robustness of the Wigner crystal with emergent kinetics.

Fig. 6.1 schematically summarizes our findings. Fig. 6.1 plots the single-particle band gap, Δ_s, versus the single-particle bandwidth, W, for a one-dimensional optical lattice in the presence of SOC. The slope of a straight line in this plane quantifies the band flatness ratio [147] ($F \equiv W/\Delta_s$). The lobe in Fig. 6.1 plots the regime where we find, in this work, that the Wigner crystal is stable and can be described by an emergent Luttinger liquid theory. In the far right part of the graph, the highly dispersive band favors particles nesting in band minima. Here a conventional Luttinger liquid theory applies. In the upper left corner of the diagram, the Wigner crystal destabilizes because the single-particle basis states do not overlap and the nearest neighbor interaction stemming from overlapping Wannier functions vanishes. Here the interactions cannot lift the degeneracy of the lowest flat band.

We find that the spinor Wigner crystal with emergent kinetics survives realistic effects expected in an optical lattice experiment: a non-zero bandwidth and band mixing. Studying spectra within the lobe reveals that emergent dispersive states are adiabatically connected to states found in the approximate model studied in Ref. [150]. We use numerical exact diagonalization to map out the phase diagram and rigorously quantify the location of the lobe for various flatness ratios. We also find that (within the lobe) band mixing lowers the gap of the Wigner crystal making it less stable than predicted in Ref. [150]. We also verify that realistic trapping parameters for a common example atom, ^{40}K, still allow a Wigner crystal near the trap center even without assuming that a Feshbach resonance can increase the interaction strength.

The outline of the chapter is as follows: In Sec. 6.2 we construct the full physical model and relate it to the flat-band projected model studied previously in Ref. [150]. We analytically

solve the single-particle part of the Hamiltonian to construct the basis in which we represent the full interacting Hamiltonian. In Sec. 6.3 we study the impact of non-zero bandwidth and band mixing by diagonalizing an interacting model that extrapolates between the single-band projected model and the full physical model. In Sec. 6.4 we map out the phase diagram by numerically diagonalizing the full physical model. We find a sizable region of stability for the Wigner crystal. We summarize in Sec. 6.5.

6.2 Model

In this section we derive a tight-binding model of N fermions in a one-dimensional optical lattice with an equal population of two hyperfine states. We incorporate the lowest (nearly flat) band and the second band. We solve the single-particle tight-binding limit analytically to obtain the band gap and the bandwidth. We then derive the tight-binding form of the s-wave interaction term. We include all intra and inter-band interaction terms. The full model constructed in this section will then be diagonalized in later sections to compare with results reported previously [150] on the projected flat band model.

We start with a first-quantized non-interacting Hamiltonian that adds SOC to the optical lattice potential [147, 150]:

$$H_0^s = \frac{p_x^2}{2m} - sE_R \cos^2(k_L x) + \left(\frac{\hbar k_R}{m}\right) p_x \sigma_z + \Omega \sigma_x, \tag{6.1}$$

where p_x is the momentum of particles of mass m, the second term is the optical lattice potential created by counter-propagating lasers with wave vector k_L, and the lattice depth is sE_R, where $E_R = \hbar^2 k_L^2/2m$ is the recoil energy. The third term describes spin-orbit coupling created by Raman lasers with wave vector k_R, and $\boldsymbol{\sigma} = (\sigma_x, \sigma_y, \sigma_z)$ are the Pauli

spin matrices. In the last term, Ω is the Rabi frequency which acts as the Zeeman field strength. In the following, we choose a lattice spacing π/k_L as the length unit. In these units, $k_R = \pi/2$ implies $k_R = k_L/2$.

To pass to the tight binding limit we rewrite the Hamiltonian in second quantized form [150]:

$$H_0 = -2t \sum_{k,\sigma} \cos(k + k_R\sigma) c^\dagger_{k\sigma} c_{k\sigma} + \Omega \sum_{k,\sigma\neq\bar{\sigma}} c^\dagger_{k\sigma} c_{k\bar{\sigma}}, \tag{6.2}$$

where $c^\dagger_{k,\sigma}$ creates a fermion at wavevector k in one of two hyperfine states with pseudo-spin indices $\sigma = \uparrow, \downarrow$. We set $k_R\sigma = \pm k_R$ for $\sigma = \uparrow, \downarrow$ respectively. We have checked, by directly solving the continuum model, that the tight binding model presented here reproduces the bands of the continuum model to within 5% for the parameters studied here.

Eq. ((6.2)) can be solved analytically by passing to the band basis, labeled by $\alpha = +, -$. We start by rewriting the single-particle tight-binding model, Eq. (6.2), in matrix form:

$$\begin{aligned} H_0 &= -2t \sum_{k,\sigma} \cos(k + k_R\sigma) c^\dagger_{k\sigma} c_{k\sigma} + \Omega \sum_{k,\sigma\neq\bar{\sigma}} c^\dagger_{k\sigma} c_{k\bar{\sigma}} \\ &= C^\dagger_k [h_0(k) I + \mathbf{h}(k) \cdot \boldsymbol{\sigma}] C_k, \end{aligned} \tag{6.3}$$

where I is the identity matrix, vector $C_k = (c_{k\uparrow}, c_{k\downarrow})^T$, $h_0(k) = -2t \cos k \cos k_R$, and $\mathbf{h}(k) = (\Omega, 0, 2t \sin k \sin k_R)$. We can rewrite $\mathbf{h}(k)$ in spherical coordinates:

$$\mathbf{h}(k) = h_k(\sin\theta_k \cos\phi_k, \sin\theta_k \sin\phi_k, \cos\theta_k), \tag{6.4}$$

where h_k is the magnitude, θ_k is the polar angle, ϕ_k is the azimuthal angle. In the case studied here we have $\cos\theta_k = 2t \sin k \sin k_R / h_k$ and $\phi_k = 0$.

We can now diagonalize eigenvalues H_0 to obtain the eigenvalues $E_\pm(k)$ and eigenvectors

$v_{k\pm}$ using a unitary transformation:

$$U^{\dagger}(k)[h_0(k)I + \mathbf{h}(k)\cdot\boldsymbol{\sigma}]U(k) = \mathrm{diag}\{E_+(k), E_-(k)\}, \tag{6.5}$$

where we find:

$$E_{\pm}(k) = h_0(k) \pm |\mathbf{h}(k)|, \tag{6.6}$$

with:

$$U(k) = \begin{pmatrix} v_{k+} & v_{k-} \end{pmatrix} = \begin{pmatrix} \cos(\theta_k/2) & \sin(\theta_k/2) \\ \sin(\theta_k/2) & -\cos(\theta_k/2) \end{pmatrix}. \tag{6.7}$$

We can then use the unitary transform to define the band operators $\chi_{k\pm}$:

$$C_k = U(k)\mathrm{X}_k, \tag{6.8}$$

where $\mathrm{X}_k = (\chi_{k+}, \chi_{k-})^T$, so that:

$$H_0 = \sum_k \left[E_-(k)\chi^{\dagger}_{k-}\chi_{k-} + E_+(k)\chi^{\dagger}_{k+}\chi_{k+}\right]. \tag{6.9}$$

This shows that the single-particle tight-binding model, Eq. (6.2), in the spin basis can be diagonalized by rewriting the model in the band basis, Eq. (6.10).

So the unitary transformation leads to a diagonal form of Eq. ((6.2)):

$$H_0 = \sum_{k,\alpha} E_\alpha(k)\chi^{\dagger}_{k\alpha}\chi_{k\alpha} \tag{6.10}$$

with eigenvalues:

$$E_{\pm}(k) = -2t\cos k\cos k_R \pm \sqrt{\Omega^2 + 4t^2\sin^2 k\sin^2 k_R}. \tag{6.11}$$

The eigenvectors are: $\chi_{k\alpha} = \sum_\sigma v^*_{k\alpha,\sigma} c_{k\sigma}$ with coefficients

$$v_{k+} = (\cos(\theta_k/2),\ \sin(\theta_k/2))^T \tag{6.12}$$

and

$$v_{k-} = (\sin(\theta_k/2),\ -\cos(\theta_k/2))^T, \tag{6.13}$$

where $\cos(\theta_k) = 2t\sin(k)\sin(k_R)/h_k$. The basis states $\chi_{k\alpha}$ define spinors with a magnetic moment orientation that depends on θ_k.

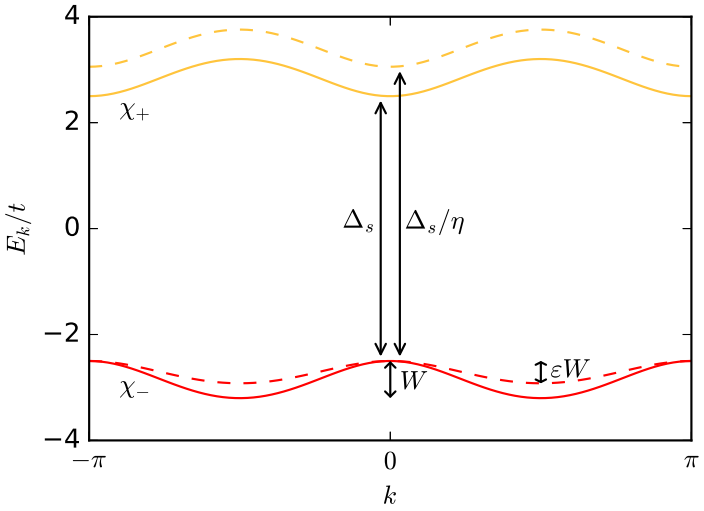

Figure 6.2: Single-particle energies as a function of wavevector for the two bands, $\alpha = \pm$. The solid lines plot Eq. (6.11) for $\Omega = 2.5t$ and $k_R = k_L/2$ which lead to a flatness ratio $F \approx 7$. The dashed lines plot the same but for Eqs. (6.23) and (6.24) with the dimensionless parameters $\varepsilon = 0.6$ and $\eta = 0.9$ introduced to tune the single-particle bandwidth and the band gap, respectively.

Fig. 6.2 plots the band structure defined by Eq. (6.11) in the case of maximal spin-orbital coupling $k_R = k_L/2$. Here we see that the lowest of the two bands is very flat, $F \approx 7$. We quantify the band flatness ratio here using the single-particle bandwidth:

$$W = \sqrt{\Omega^2 + 4t^2} - |\Omega|, \tag{6.14}$$

and the single-particle band gap:

$$\Delta_s = 2|\Omega|. \tag{6.15}$$

We now use the single-particle basis to represent the inter-atom interaction term. We consider s-wave scattering between atoms. The interaction in the basis before application of spin-orbit coupling leads to the usual Hubbard interaction between atoms:

$$H_{\text{int}} = \frac{U}{2} \sum_{i,\sigma\neq\bar{\sigma}} c^\dagger_{i\sigma} c^\dagger_{i\bar{\sigma}} c_{i\bar{\sigma}} c_{i\sigma}. \tag{6.16}$$

This interaction is purely onsite because of the local nature of the Wannier functions (before the application of spin-orbit coupling). After a Fourier transform to momentum space the Hubbard interaction becomes:

$$H_{\text{int}} = \sum_{\{k\},\sigma\neq\bar{\sigma}} V_{\{k\}} c^\dagger_{k_4\sigma} c^\dagger_{k_3\bar{\sigma}} c_{k_2\bar{\sigma}} c_{k_1\sigma}, \tag{6.17}$$

where $V_{\{k\}} = (U/2L)\delta'_{k_4+k_3=k_2+k_1}$, δ' indicates momentum conservation up to multiples of the reciprocal lattice vector, and L is the number of sites.

The application of spin-orbit coupling has a drastic effect on the single-particle basis states. The basis states can, for low to intermediate F, elongate in real space and overlap between nearest neighbors. We incorporate spin-orbit coupling by rewriting the interaction in terms of single-particle eigenstates of Eq. (6.2):

$$H_{\text{int}} = \sum_{\{k,\alpha\}} \tilde{V}_{\{k\alpha\}} \chi^\dagger_{k_4\alpha_4} \chi^\dagger_{k_3\alpha_3} \chi_{k_2\alpha_2} \chi_{k_1\alpha_1}, \tag{6.18}$$

where the interaction matrix elements

$$\tilde{V}_{\{k,\alpha\}} = (U/2L) \sum_{\sigma \neq \bar{\sigma}} v^*_{k_4\alpha_4,\sigma} v^*_{k_3\alpha_3,\bar{\sigma}} v_{k_2\alpha_2,\bar{\sigma}} v_{k_1\alpha_1,\sigma} \delta'_{k_4+k_3=k_2+k_1} \tag{6.19}$$

incorporate both the interaction and spin-orbit coupling. Passing back to Wannier functions in real space one can see that, for low to intermediate F, the Wannier functions have been considerably elongated by spin-orbit coupling [150] to overlap in neighboring sites. The interaction can therefore include nearest-neighbor interaction terms when written in the χ basis.

The total Hamiltonian becomes:

$$H = H_0 + H_{\text{int}}, \tag{6.20}$$

where H_0 is diagonal in the χ basis, Eq. (6.10). The interaction term is off-diagonal and, for certain parameters, yields a formidable non-perturbative problem because the lowest band becomes nearly degenerate. The study of H will form the focus of the rest of the chapter.

Ref. [150] used a flat band approximation to study Eq. (6.20) for $N/L = 1/2$. In the flat band approximation, two limits were taken. First, all particles are projected onto the lowest band, $\alpha = -$. At partial filling, lowest band projection can be thought of as setting $\Delta_s \to \infty$. Second, the single-particle dispersion was assumed to be irrelevant and H_0 was dropped. In this approximation, the projected Hamiltonian becomes:

$$H^P = \sum_{\{k\}} V^P_{\{k\}} \chi^\dagger_{k_4-} \chi^\dagger_{k_3-} \chi_{k_2-} \chi_{k_1-}, \tag{6.21}$$

where

$$V^P_{\{k\}} = (U/L) v^*_{k_4-,\uparrow} v^*_{k_3-,\downarrow} v_{k_2-,\downarrow} v_{k_1-,\uparrow} \delta'_{k_4+k_3=k_2+k_1} \tag{6.22}$$

We see explicitly that H^P defines a non-perturbative problem because there are no other terms in the model. The flat band approximation assumes that inclusion of single-particle terms (H_0) will merely perturb the physics found by diagonalizing Eq. (6.21) while the low energy eigenstates remain in the same universality class. We test the flat band approximation by comparing solutions to Eqs. (6.20) and (6.21). Non-zero bandwidth and mixing due to interaction effects should perturb the low energy eigenstates. We consider the impact of both finite bandwidth and inter-band mixing in the following.

6.3 Band Dispersion and Band Mixing

In this section we use exact diagonalization to study the impact of finite bandwidth and band mixing separately. We introduce tuning parameters to H so we can extrapolate between H and H^P to thus allow separate analyses of each effect. By examining the spectrum and computing eigenstate overlaps we find that band mixing alone lowers the gap between the ground and first excited state by a factor of at least ≈ 20. When we include both band mixing and non-zero bandwidth we also find that the many-body dispersion shifts in wave-vector.

We start by inserting tuning parameters into the single-particle energy to allow a separation of effects. For the lowest band we tune the width of the lowest band using an artificial tuning parameter, ε:

$$E_-(\varepsilon, k) \equiv -\Omega + [E_-(k) + \Omega]\varepsilon \tag{6.23}$$

while for the second band we tune the band gap with η:

$$E_+(\eta, k) \equiv E_+(k)/\eta \tag{6.24}$$

The dashed lines in Fig. 6.2 show the effect of the parameters ε and η. For $\varepsilon = 0$ we recover

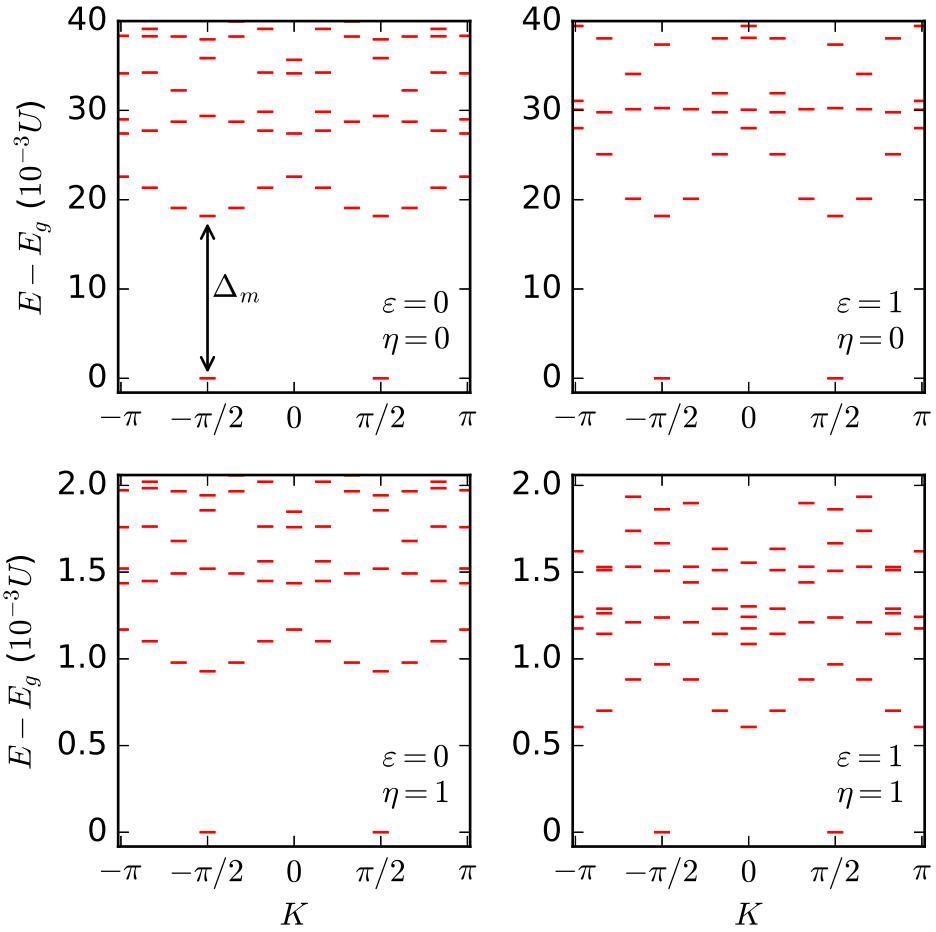

Figure 6.3: Many-body energies versus total wavevector obtained from diagonalizing Eq. (6.25) in four distinct limits of the parameters ε and η. The energy zero is the ground state energy, E_g. The projected model, Eq. (6.21), is retrieved for $\varepsilon = \eta = 0$ (upper left). A non-zero bandwidth is introduced for $\varepsilon = 1$ and $\eta = 0$ (upper right) while a second flat band is introduced for $\eta = 1$ and $\varepsilon = 0$ (lower left). The full physical model, Eq. (6.20), is retrieved for $\varepsilon = \eta = 1$ (lower right). The ground state remains a Wigner crystal with 2-fold sublattice degeneracy in all four panels and we have checked that the ground state energy and ground state wave functions are adiabatically connected between the four limits. Comparing the $\eta = 0$ to $\eta = 1$ cases shows that band mixing lowers the many-body band gap, Δ_m, by a factor of ≈ 20. We have used the following parameters: $N = 6$, $L = 12$, $t = 0.01U$, $\Omega = 0.025U$, $k_R = k_L/2$, i.e., $\Delta_s = 0.05U$, and $W = 0.007U$. This corresponds to $F \approx 7$.

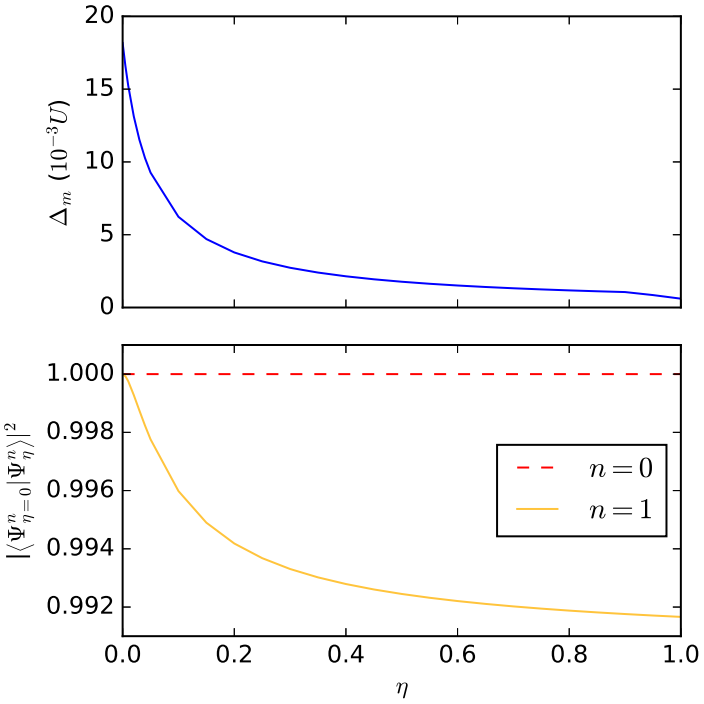

Figure 6.4: The many-body gap (top) and many-body wavefunction overlap (bottom) obtained from diagonalizing Eq. (6.25) as a function of the dimensionless parameter η. Here we see that the many-body gap is significantly lowered as we introduce a second single-particle band by increasing η. The bottom panel plots the overlap between the $\eta = 0$ wavefunction and the wavefunction for $\eta \geq 0$ for both the ground state ($n = 0$) and the first excited state ($n = 1$) to show that the second single-particle band alters the nature of just the first excited state. The parameters are the same as Fig. 6.3 but for $\varepsilon = 1$.

the flat band limit and for $\eta = 0$ we set the band gap to infinity to recover the single band limit. The limit $\varepsilon = \eta = 1$ returns us to the physical single-particle energy, Eq. (6.11).

By adding interactions we construct a model that allows us to tune between different limits:

$$H_{\varepsilon,\eta} = \sum_k \left[E_-(\varepsilon, k)\chi^\dagger_{k-}\chi_{k-} + E_+(\eta, k)\chi^\dagger_{k+}\chi_{k+} \right] + H_{\text{int}} \tag{6.25}$$

For $\varepsilon \to 0$ and $\eta \to 0$ we have, at partial filling, the flat single-band limit: $\lim_{\varepsilon,\eta\to 0} H_{\varepsilon,\eta} = H^P$ and for $\varepsilon = \eta = 1$ we have the full physical model $H_{\varepsilon=1,\eta=1} = H$.

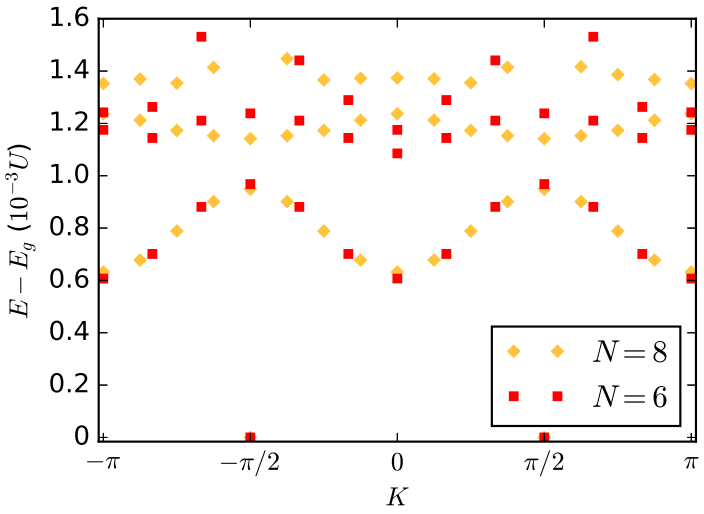

Figure 6.5: The same as Fig. 6.3 but for the full physical model, Eq. (6.20), where the squares (diamonds) are for $N = 6$ ($N = 8$) particles on $L = 12$ ($L = 16$) sites. The data collapse shows that the ground and first excited states are already in the thermodynamic limit.

We diagonalize Eq. (6.25) in different limits to explore the impact of single-particle band effects on interaction-driven physics. Fig. 6.3 shows the results of diagonalizing Eq. (6.25) in four different limits. The top left panel reproduces the results found in Ref. [150] for the flat single-band model, H^P. Here we see that the lowest energy state is two-fold degenerate and corresponds to a Wigner crystal of spinors that can be generated by just the diagonal density-density interaction term in Eq. (6.21). The two degenerate states arise because of the sublattice degeneracy for the two ways of placing the crystal on the one-dimensional lattice. There is a gap to the lowest band of excitations. Ref. [150] pointed out that these states show emergent kinetics due to the finite many-body bandwidth driven entirely by off-diagonal terms in Eq. (6.21). The focus of our work here is to probe the stability of this low-energy structure as we introduce a second band and allow non-zero bandwidth.

The top-right and bottom-left panels of Fig. 6.3 show the result of adding finite bandwidth ($\varepsilon = 1$) and band mixing ($\eta = 1$), respectively. Here we see that setting $\varepsilon = 1$ does very

little to the many-body spectrum at low energies. For $F = 7$ the band is so flat that the small but finite single-particle dispersion does not perturb the large interaction much. But for $\varepsilon = 0$ and $\eta = 1$ we see that bringing two flat bands relatively near each other causes the many-body gap, Δ_m, to decrease by a factor of ≈ 20 while keeping the structure of the low energy states qualitatively the same.

The bottom-right panel of Fig. 6.3 shows the spectrum for the full model, H. Here we see that including both finite bandwidth and band mixing not only lowers the gap appreciably but the many-body excited states are shifted in K-space so that the many-body dispersion has a minimum at $K = 0$ instead of $K = \pm\pi/2$. Here the non-zero single-particle dispersion mixed the lowest energy many-body excited states. Otherwise the qualitative features of the low energy states remains the same as we go from $\varepsilon = \eta = 0$ to $\varepsilon = \eta = 1$.

The top panel of Fig. 6.4 shows the decrease in the many-body gap as the single-particle band gap is lowered. Here we keep a non-zero single-particle dispersion ($\varepsilon = 1$) but we tune the single-particle gap from infinity to Δ_s. The gap never drops to zero thus signaling that the low energy states in the full Hamiltonian, H, are adiabatically connected to the those of the projected Hamiltonian, H^P.

The mixing of the many-body excited states drives the lowering of the gap. To see this we plot the overlap of the lowest two many-body states in the lowest panel of Fig. 6.4. Here we see that the ground state remains unperturbed but the mixing of the excited states somewhat lowers the overlaps from the single-band ($\eta = 0$) limit. Nonetheless we see that the overlap remains large and does not show any cusps. There are therefore no transitions as we lower the band gap for $F = 7$. In the following sections we will vary F to find transitions (where the many-body gap vanishes).

We have checked that our results presented here do not change as we increase particle

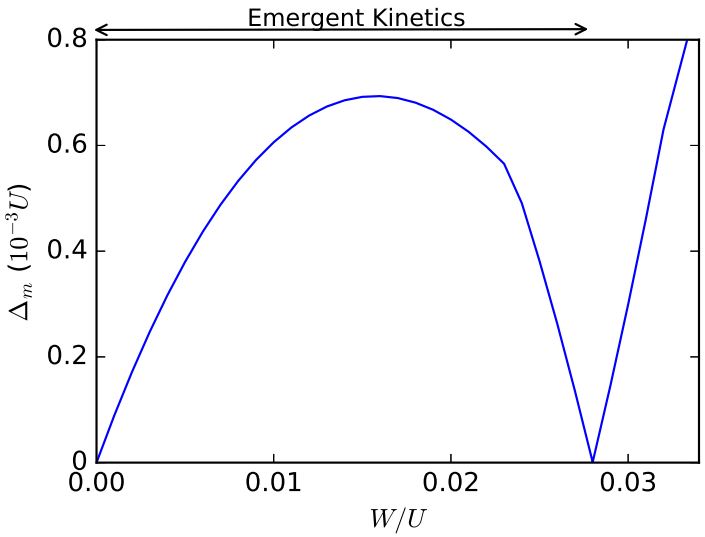

Figure 6.6: The many-body energy gap plotted as function of bandwidth. The parameters are the same as Fig. 6.3 but for the full physical model, Eq. (6.20), with the band gap held constant, $\Delta_s = 0.08U$. Here we see that at zero bandwidth the single-particle basis states have no spread and, as a result, the interaction remains onsite and cannot lift the degeneracy. But as the bandwidth increases, the nearest-neighbor interaction terms lift the degeneracy to reveal the Wigner crystal ground state and opens a gap to a set of emergent excitations captured by an effective Luttinger liquid theory. But as the bandwidth increases further the gap closes as the Wigner crystal transitions to a conventional Luttinger liquid regime.

number and are therefore valid in the thermodynamic limit. Fig. 6.5 shows data collapse in the spectrum. The low energy states fall on one another indicating a consistency in scaling to the thermodynamic limit. This was also found for H^P in Ref. [150] further showing that the low energy eigenstates of both H and H^P are in the same universality class.

6.4 Phase Diagram and Stability

We now map out the stability phase diagram of the interaction-only spinor Wigner crystal phase of Eq. (6.20). Instabilities arise as we increase the single-particle bandwidth. For large W the particles gain in energy by nesting in the single-particle band minima. There

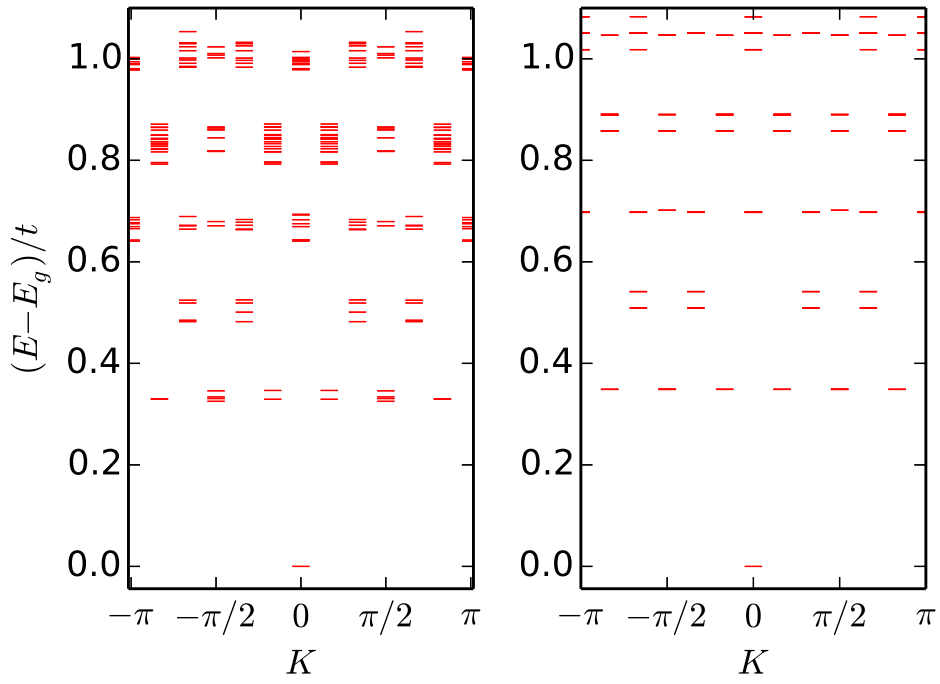

Figure 6.7: Characteristic many-body spectrum of Eq. (6.20) computed for a weakly interacting case (left panel, $U = t/2$) and the non-interacting case (right panel, $U = 0$). We have also set $N = 6$, $L = 12$, $\Omega = 2.5t$, and $k_R = k_L/2$. These parameters lead to a flatness ratio used in the other figures as well, $F \approx 7$. A comparison of both panels shows that the spectra are qualitatively similar, i.e., states occur at the same wavevectors and nearly the same energies. We can therefore think of the ground state in both cases as a partially filled band of weakly interacting fermions. The weakly interacting case conforms to conventional Luttinger liquid theory.

is therefore a transition from the interaction-dominated regime (with emergent kinetics) to a weakly interacting state (a conventional Luttinger liquid) as the bandwidth is increased. Increasing the single-particle band gap also drives a transition. At first we expect that increasing Δ_s might favor the approximation that led to emergent kinetics. But note that large F implies that the lowest-band Wannier functions have little overlap between nearest neighbor sites [150]. As a result, increasing F decreases density assisted hopping terms between neighbors and therefore suppresses emergent kinetics. We thus expect a transition to a weakly interacting regime as Δ_s and therefore F is increased.

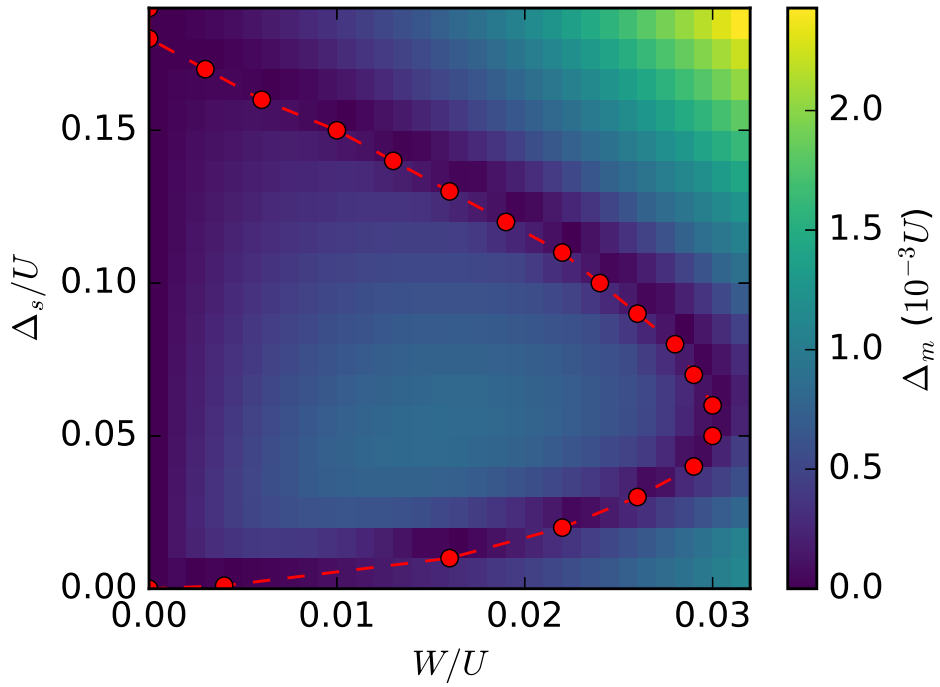

Figure 6.8: Stability phase diagram of the Wigner crystal with emergent kinetics plotted as function of both the single-particle band gap and the bandwidth. The color coding plots the size of the many-body gap obtained from diagonalization of Eq. (6.20) for $N = 6$, $L = 12$, and $k_R = k_L/2$. The circles plot the points where the many-body gap vanishes and the line is a guide to the eye. The Wigner crystal is stable within the lobe. Outside the lobe we have a conventional Luttinger liquid with a gap set by finite-size effects.

We increase W and diagonalize Eq. (6.20) to find the lowest energy eigenstates. Note that increasing W impacts H_0 directly and $H_{\rm int}$ indirectly through the change in basis states $\chi_{k\alpha}$. Fig. 6.6 plots the many-body gap as a function of the bandwidth. We see that the many-body gap starts from zero at $W = 0$. For $W \to 0$ we have $F \to \infty$ and Eq. (6.21) is a good approximation to Eq. (6.20). But in this limit the are essentially no nearest neighbor terms to lift the massive degeneracy of spinless particles in the lowest flat band. Here the flat band remains gapless. As we increase W nearest neighbor terms interaction terms (not single-particle terms) drive the formation of a spinor Wigner crystal with emergent kinetics and the many-body gap opens.

Upon increasing W further the many-body gap closes and a new state arises in Fig. 6.6. Here the Wigner crystal destabilizes to a more conventional state where H_0 and interactions compete in Eq. (6.20). Conventional Luttinger liquid theory can be used to show that the particles tend to sit about the single-particle band minimum. The ground state in the large W regime can be understood by filling the lowest single-particle band with weakly interacting fermions. Characteristic spectra that arise for large W are shown in the left panel of Fig. 6.7. The right panel shows that non-interacting spectra give nearly the same results. In both panels the gaps are due to finite-size effects and there is no ground state degeneracy since filling of the lowest single-particle band leads to a unique K. We can therefore understand the large W limit in a weakly interacting picture of band filling of spinless fermions.

We culminate our findings in a phase diagram that plots the stability of the Wigner crystal and its emergent kinetics. The shading in Fig. 6.8 plots the size of the many-body gap as a function of both the single-particle bandwidth and band gap. The circles denote critical points where the many-body gap closes and the ground state degeneracy changes from two (Wigner crystal with emergent kinetics) to one (conventional Luttinger liquid regime). Inside the lobe nearest neighbor interactions establish the many-body gap but outside the lobe the gap is, for our finite size simulations, set by the finite size of the system.

The parameters needed to reach the central part of the lobe are accessible with current experiments. We assume ^{40}K atoms with two hyperfine levels populated to define the pseudospin. To compute the tight-binding parameters we solve the periodic Schrödinger equation using Mathieu functions and compute the Wannier functions in the usual way [130, 148]. We find that for a perpendicular confinement of $60E_R$, a lattice depth of $s \approx 13$, and a bare scattering length of $a_s = 104a_0$ (where a_0 is the Bohr radius) we can achieve $t = 0.01U$, where $t \approx 0.01E_R$ and $U \approx E_R$. The Zeeman field can then be chosen to be $\Omega \approx 0.025E_R$ with $k_R = k_L/2$. This leads to $F \approx 7$ and corresponds to a central part of the lobe in Fig. 6.8

with $\Delta_s/U \approx 0.05$ and $W/U = 0.007$.

The parabolic trapping potential competes with the many-body gap to limit the size of the Wigner crystal near the trap center. We can estimate the size of the Wigner crystal by equating the energy cost required to overcome Δ_m with the trapping potential energy. The trapping potential is $m\omega_{\rm tr}^2 x/2$, where $\omega_{\rm tr}$ is the trapping frequency. We estimate the position x_{max} where the crystal no longer exists using $\Delta_m = m\omega_{\rm tr}^2 x_{max}/2$. For ^{40}K on a lattice formed by lasers with wavelength 826 nm and a realistic trapping strength $\omega_{\rm tr} = 40 - 70$Hz we find a crystal size of $2x_{max} \approx 20 - 34$ lattice sites. This size was estimated using Δ_m from the full Hamiltonian, Eq. (6.20). x_{max} is smaller than the size estimated using the single-band projected model [1] because the band mixing lowered Δ_m. Nonetheless we find that band mixing and finite bandwidth in H still allow a Wigner crystal with emergent kinetics in a small region near the center of the trap. The strength of the crystal can be increased by increasing the strength of the interaction (and therefore U) using a Feshbach resonance.

6.5 Summary

We have studied a model of two-component fermionic atoms in a one-dimensional optical lattice in the presence of SOC. We have mapped out the stability phase diagram of a spinor Wigner crystal with emergent kinetics in its low energy excitation state space. Our results demonstrate the parameter regime of validity of the approximations made in Ref. [150] by showing that the projected approximate model, Eq. (6.21), captures the essential properties of the low energy states of the full model, Eq. (6.20). We find that band mixing lowers the gap of the Wigner crystal by at least a factor of ≈ 20. Band mixing and a finite bandwidth also shift the low energy momenta of the emergent many-body models from a total momentum

[1] We find $x_{max} \approx 100$ sites with Eq. (6.21) [150].

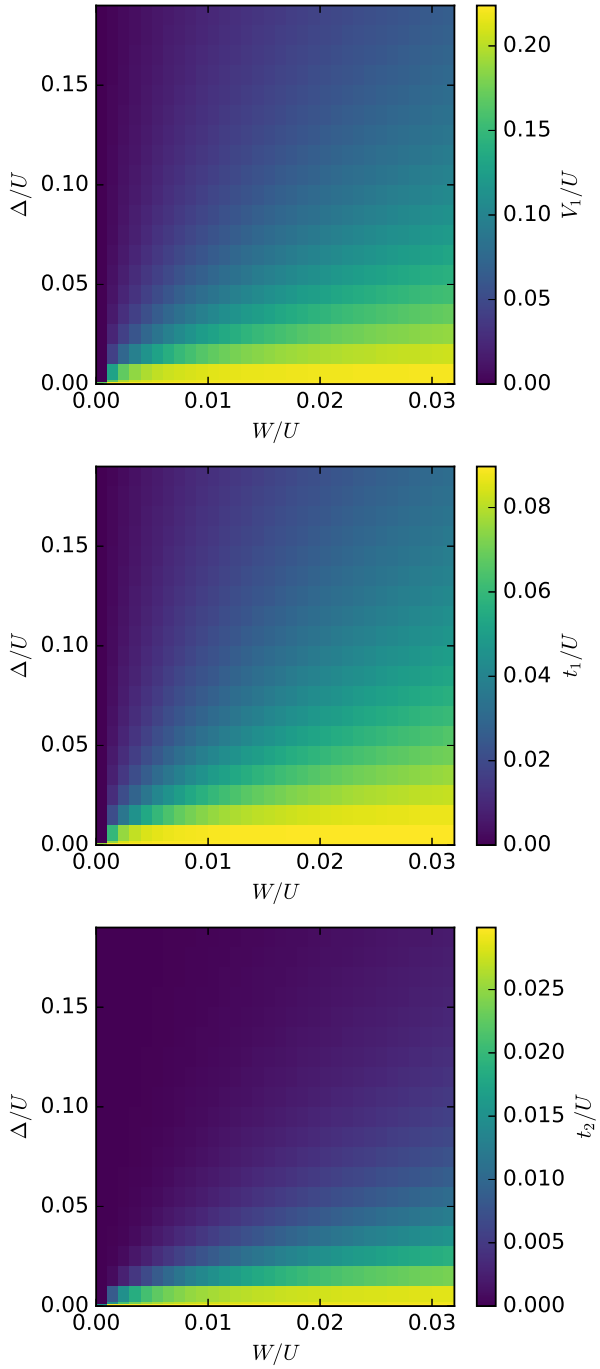

Figure 6.9: Strength of leading diagonal terms $V_1\tilde{n}_i\tilde{n}_{i+1}$ and leading off-diagonal terms $-t_1\chi^\dagger_{i+2}\tilde{n}_{i+1}\chi_i$ and $t_2\chi^\dagger_{i+3}\tilde{n}_i\chi_{i+1}$ (note that the signs before t_1 and t_2 are different) plotted as function of both the single-particle band gap Δ_s and the bandwidth W.

of $K = \pm\pi/2$ in approximate case, Eq. (6.21), to $K = 0$ in the full model, Eq. (6.20). Nonetheless, the Wigner crystal and its emergent modes show sufficient stability to occupy the central region of a trapped optical lattice experiment. We estimate ≈ 30 sites for the bare interaction between ^{40}K atoms in a trap. A Feshbach resonance can be used increase the strength of the states discussed here.

Chapter 7

Summary

The results presented in this thesis demonstrate the rich variety of phases one can find in strongly correlated systems. By utilizing the powerful exact diagonalization method, we have studied systems with complicated projected interactions, systems with spontaneous symmetry breaking, and systems with spin-orbit coupling. We can see the broad and general applicability of ED through these cases. Even though ED is limited to finite-size systems, we also see that the techniques of finite size scaling and varying boundary conditions allows us overcome the finite-size limitation of ED. All of these techniques can be easily used to study new strongly correlated systems or pursue further studies of the models we investigated in this thesis.

FCIs were studied in chapter 4. In this context there are at least two ways in which ED can play an important role in future work on FCIs. First, an analytic wave function of the FCI ground state would help in understanding this phase. It would be helpful (in future work) to have a Laughlin-like wavefunction for this state. Examining the wavefunction output of ED for different geometries can help to get insight into protocols for constructing such wavefunctions. Second, to understand phases formed by FCI quasiparticles, it will be better to have an effective theory describing the dynamics of quasiparticles themselves. ED can help in trying different types of effective Hamiltonians by verifying wavefunction overlap.

TMIs were studied in chapter 5. Here we found that realistic spatially decaying interactions support the TMI on the decorated honeycomb lattice. But this lattice may still be too

complicated for realization in optical lattice systems. Simpler lattices with different types of interactions may also allow realization of TMI. For example, a kagome lattice with dipolar interaction [155] offers a much simpler route. For any type of interaction, ED can help in confirming the existence of the TMI phase. Also, the rich phases surrounding the TMI phase need more in-depth studies.

The emergent kinetics studied in chapter 6 serves as a great example of exotic states that can emerge out of strongly correlated systems.

Quantum condensed matter physics has entered the age of theoretical/numerical predictions that in turn guide experimental discoveries. The discovery of topological insulators, Chern insulators, and Weyl semimetals are all examples of this trend. ED as a general method will become more important in guiding experiments, not just studying toy models. The techniques demonstrated in this thesis will continue to make more discoveries.

Bibliography

[1] P. W. Anderson. More Is Different. *Science*, 177(4047):393–396, August 1972.

[2] K. v. Klitzing, G. Dorda, and M. Pepper. New Method for High-Accuracy Determination of the Fine-Structure Constant Based on Quantized Hall Resistance. *Phys. Rev. Lett.*, 45(6):494–497, August 1980.

[3] D. C. Tsui, H. L. Stormer, and A. C. Gossard. Two-Dimensional Magnetotransport in the Extreme Quantum Limit. *Physical Review Letters*, 48:1559–1562, May 1982.

[4] F. E. Camino, Wei Zhou, and V. J. Goldman. Realization of a Laughlin quasiparticle interferometer: Observation of fractional statistics. *Physical Review B*, 72(7):075342, August 2005.

[5] D. J. Thouless, M. Kohmoto, M. P. Nightingale, and M. den Nijs. Quantized Hall Conductance in a Two-Dimensional Periodic Potential. *Physical Review Letters*, 49(6):405–408, August 1982.

[6] M. Z. Hasan and C. L. Kane. Colloquium: Topological insulators. *Reviews of Modern Physics*, 82:3045–3067, October 2010.

[7] X.-L. Qi and S.-C. Zhang. Topological insulators and superconductors. *Reviews of Modern Physics*, 83:1057–1110, October 2011.

[8] Cui-Zu Chang, Jinsong Zhang, Xiao Feng, Jie Shen, Zuocheng Zhang, Minghua Guo, Kang Li, Yunbo Ou, Pang Wei, Li-Li Wang, Zhong-Qing Ji, Yang Feng, Shuaihua Ji, Xi Chen, Jinfeng Jia, Xi Dai, Zhong Fang, Shou-Cheng Zhang, Ke He, Yayu Wang, Li Lu, Xu-Cun Ma, and Qi-Kun Xue. Experimental Observation of the Quantum

Anomalous Hall Effect in a Magnetic Topological Insulator. *Science*, 340(6129):167–170, April 2013.

[9] Cui-Zu Chang, Weiwei Zhao, Duk Y. Kim, Haijun Zhang, Badih A. Assaf, Don Heiman, Shou-Cheng Zhang, Chaoxing Liu, Moses H. W. Chan, and Jagadeesh S. Moodera. High-precision realization of robust quantum anomalous Hall state in a hard ferromagnetic topological insulator. *Nature Materials*, 14(5):473–477, May 2015.

[10] Eric M. Spanton, Alexander A. Zibrov, Haoxin Zhou, Takashi Taniguchi, Kenji Watanabe, Michael P. Zaletel, and Andrea F. Young. Observation of fractional Chern insulators in a van der Waals heterostructure. *Science*, 2018.

[11] M. Zahid Hasan, Su-Yang Xu, Ilya Belopolski, and Shin-Ming Huang. Discovery of Weyl Fermion Semimetals and Topological Fermi Arc States. *Annual Review of Condensed Matter Physics*, 8(1):289–309, 2017.

[12] N. P. Armitage, E. J. Mele, and Ashvin Vishwanath. Weyl and Dirac semimetals in three-dimensional solids. *Reviews of Modern Physics*, 90(1):015001, January 2018.

[13] Kai Sun, Zhengcheng Gu, Hosho Katsura, and S. Das Sarma. Nearly Flatbands with Nontrivial Topology. *Physical Review Letters*, 106(23):236803, June 2011.

[14] Evelyn Tang, Jia-Wei Mei, and Xiao-Gang Wen. High-Temperature Fractional Quantum Hall States. *Physical Review Letters*, 106(23):236802, June 2011.

[15] Titus Neupert, Luiz Santos, Claudio Chamon, and Christopher Mudry. Fractional Quantum Hall States at Zero Magnetic Field. *Physical Review Letters*, 106(23):236804, June 2011.

[16] N. Regnault and B. A. Bernevig. Fractional Chern Insulator. *Physical Review X*, 1(2):021014, October 2011.

[17] S. Raghu, Xiao-Liang Qi, C. Honerkamp, and Shou-Cheng Zhang. Topological Mott Insulators. *Physical Review Letters*, 100(15):156401, April 2008.

[18] R. B. Laughlin. Quantized motion of three two-dimensional electrons in a strong magnetic field. *Physical Review B*, 27(6):3383–3389, March 1983.

[19] F. Lin, C. Zhang, and V. W. Scarola. Emergent Kinetics and Fractionalized Charge in 1D Spin-Orbit Coupled Flatband Optical Lattices. *Physical Review Letters*, 112(11):110404, March 2014.

[20] B. Bauer, L. D. Carr, H. G. Evertz, A. Feiguin, J. Freire, S. Fuchs, L. Gamper, J. Gukelberger, E. Gull, S. Guertler, A Hehn, R. Igarashi, S. V. Isakov, D. Koop, P. N. Ma, P. Mates, H. Matsuo, O. Parcollet, G. Pawłowski, J. D. Picon, L Pollet, E. Santos, V. W. Scarola, U. Schollwöck, C. Silva, B. Surer, S. Todo, S. Trebst, M. Troyer, M. L. Wall, P Werner, and S. Wessel. The ALPS project release 2.0: Open source software for strongly correlated systems. *Journal of Statistical Mechanics: Theory and Experiment*, 2011(05):P05001, 2011.

[21] W. Zhu, S. S. Gong, and D. N. Sheng. Interaction-driven fractional quantum Hall state of hard-core bosons on kagome lattice at one-third filling. *Phys. Rev. B*, 94(3):035129, July 2016.

[22] Z. Qiao, S. A. Yang, W. Feng, W.-K. Tse, J. Ding, Y. Yao, J. Wang, and Q. Niu. Quantum anomalous Hall effect in graphene from Rashba and exchange effects. *Phys. Rev. B*, 82(16):161414, October 2010.

[23] F. D. M. Haldane. Model for a quantum Hall effect without Landau levels: Condensed-matter realization of the "parity anomaly". *Physical Review Letters*, 61:2015–2018, October 1988.

[24] C Lanczos. An iteration method for the solution of the eigenvalue problem of linear differential and integral operators. *J. Res. Nat'l Bur. Std*, (45):255–282, 1950.

[25] M. Chen and V. W. Scarola. Reordering fractional Chern insulators into stripes of fractional charges with long-range interactions. *Physical Review B*, 92(3):035138, July 2015.

[26] J. Wen, A. Rüegg, C.-C. J. Wang, and G. A. Fiete. Interaction-driven topological insulators on the kagome and the decorated honeycomb lattices. 82(7):075125, August 2010.

[27] M. Chen, H.-Y. Hui, S. Tewari, and V. W. Scarola. Quantum anomalous Hall state from spatially decaying interactions on the decorated honeycomb lattice. *Physical Review B*, 97(3):035114, January 2018.

[28] M. Chen and V. W. Scarola. Stability of emergent kinetics in optical lattices with artificial spin-orbit coupling. *Physical Review A*, 94(4):043601, October 2016.

[29] Fradkin Eduardo. Brief review of second quantization. *Lecture notes on condensed matter physics II (teached at UIUC)*, 2015.

[30] A. H. Castro Neto, F. Guinea, N. M. R. Peres, K. S. Novoselov, and A. K. Geim. The electronic properties of graphene. *Rev. Mod. Phys.*, 81(1):109–162, January 2009.

[31] J. P. Eisenstein and H. L. Stormer. The Fractional Quantum Hall Effect. *Science*, 248(4962):1510–1516, 1990.

[32] Qian Niu, D. J. Thouless, and Yong-Shi Wu. Quantized Hall conductance as a topological invariant. *Physical Review B*, 31(6):3372–3377, March 1985.

[33] R. B. Laughlin. Nobel Lecture: Fractional quantization. *Reviews of Modern Physics*, 71(4):863–874, July 1999.

[34] R. B. Laughlin. Quantized Hall conductivity in two dimensions. *Phys. Rev. B*, 23:5632–5633, May 1981.

[35] S.Q. Shen. *Topological Insulators: Dirac Equation in Condensed Matters*. Springer Series in Solid-State Sciences. Springer Berlin Heidelberg, 2013.

[36] Jung Hoon Han. *Skyrmions in Condensed Matter*. Springer, October 2017.

[37] Gregor Jotzu, Michael Messer, Rémi Desbuquois, Martin Lebrat, Thomas Uehlinger, Daniel Greif, and Tilman Esslinger. Experimental realization of the topological Haldane model with ultracold fermions. *Nature*, 515(7526):237–240, November 2014.

[38] J. E. Lin, H. Q.; Gubernatis. Exact diagonalization methods for quantum systems. *Computers in Physics*, 7, 1993.

[39] Shoudan Liang. A perfect Hashing function for exact diagonalization of many-body systems of identical particles. *Computer Physics Communications*, 92(1):11–15, November 1995.

[40] J. M. Zhang and R. X. Dong. Exact diagonalization: The Bose-Hubbard model as an example. *European Journal of Physics*, 31:591–602, May 2010.

[41] G.H. Golub and C.F. Van Loan. *Matrix Computations*. Johns Hopkins Studies in the Mathematical Sciences. Johns Hopkins University Press, 1996.

[42] Andreas M. Läuchli, Julien Sudan, and Erik S. Sørensen. Ground-state energy and spin gap of spin-12 Kagomé-Heisenberg antiferromagnetic clusters: Large-scale exact diagonalization results. *Phys. Rev. B*, 83(21):212401, June 2011.

[43] Andreas M. Läuchli, Julien Sudan, and Roderich Moessner. The $S=1/2$ Kagome Heisenberg Antiferromagnet Revisited. *arXiv:1611.06990 [cond-mat]*, November 2016.

[44] Alexander Wietek and Andreas M. Läuchli. Sublattice Coding Algorithm and Distributed Memory Parallelization for Large-Scale Exact Diagonalizations of Quantum Many-Body Systems. *Physical Review E*, 98(3), September 2018.

[45] Satish Balay, Shrirang Abhyankar, Mark F. Adams, Jed Brown, Peter Brune, Kris Buschelman, Lisandro Dalcin, Alp Dener, Victor Eijkhout, William D. Gropp, Dinesh Kaushik, Matthew G. Knepley, Dave A. May, Lois Curfman McInnes, Richard Tran Mills, Todd Munson, Karl Rupp, Patrick Sanan, Barry F. Smith, Stefano Zampini, Hong Zhang, and Hong Zhang. PETSc Users Manual. Technical Report ANL-95/11 - Revision 3.10, Argonne National Laboratory, 2018.

[46] Satish Balay, Shrirang Abhyankar, Mark F. Adams, Jed Brown, Peter Brune, Kris Buschelman, Lisandro Dalcin, Alp Dener, Victor Eijkhout, William D. Gropp, Dinesh Kaushik, Matthew G. Knepley, Dave A. May, Lois Curfman McInnes, Richard Tran Mills, Todd Munson, Karl Rupp, Patrick Sanan, Barry F. Smith, Stefano Zampini, Hong Zhang, and Hong Zhang. PETSc Web page. 2018.

[47] Satish Balay, William D. Gropp, Lois Curfman McInnes, and Barry F. Smith. Efficient Management of Parallelism in Object Oriented Numerical Software Libraries. In E. Arge, A. M. Bruaset, and H. P. Langtangen, editors, *Modern Software Tools in Scientific Computing*, pages 163–202. Birkhäuser Press, 1997.

[48] J E Roman and A Tomas. Krylov-Schur Methods in SLEPc. page 13.

[49] Vicente Hernandez, Jose E. Roman, and Vicente Vidal. SLEPc: A Scalable and Flexible Toolkit for the Solution of Eigenvalue Problems. *ACM Trans. Math. Softw.*, 31(3):351–362, September 2005.

[50] J. E. Roman, C. Campos, E. Romero, and A. Tomas. SLEPc Users Manual. Tech-

nical Report DSIC-II/24/02 - Revision 3.10, D. Sistemes Informàtics i Computació, Universitat Politècnica de València, 2018.

[51] V. Hernandez, J. E. Roman, and V. Vidal. SLEPc: Scalable Library for Eigenvalue Problem Computations. *Lect. Notes Comput. Sci.*, 2565:377–391, 2003.

[52] D. C. Tsui, H. L. Stormer, and A. C. Gossard. Two-dimensional magnetotransport in the extreme quantum limit. *Phys. Rev. Lett.*, 48:1559–1562, May 1982.

[53] R. B. Laughlin. Anomalous quantum hall effect: An incompressible quantum fluid with fractionally charged excitations. *Phys. Rev. Lett.*, 50:1395–1398, May 1983.

[54] J. K. Jain. Composite-fermion approach for the fractional quantum hall effect. *Phys. Rev. Lett.*, 63:199–202, Jul 1989.

[55] V. W. Scarola, Kwon Park, and J. K. Jain. Excitonic collapse of higher landau level fractional quantum hall effect. *Phys. Rev. B*, 62:R16259–R16262, Dec 2000.

[56] VW Scarola, K Park, and J. K. Jain. Cooper instability of composite fermions. *Nature*, 406:863, 2000.

[57] Hangmo Yi and H. A. Fertig. Laughlin-jastrow-correlated wigner crystal in a strong magnetic field. *Phys. Rev. B*, 58:4019–4027, Aug 1998.

[58] Gregory Moore and Nicholas Read. Nonabelions in the fractional quantum hall effect. *Nuclear Physics B*, 360(2–3):362 – 396, 1991.

[59] M. M. Fogler. Stripe and Bubble Phases in Quantum Hall Systems. In C. Berthier, L. P. Lévy, and G. Martinez, editors, *High Magnetic Fields*, volume 595 of *Lecture Notes in Physics, Berlin Springer Verlag*, pages 98–138, 2002.

[60] M. M. Fogler, A. A. Koulakov, and B. I. Shklovskii. Ground state of a two-dimensional electron liquid in a weak magnetic field. *Phys. Rev. B*, 54:1853–1871, Jul 1996.

[61] R. Côté and H. A. Fertig. Collective modes of quantum hall stripes. *Phys. Rev. B*, 62:1993–2007, Jul 2000.

[62] Seung-Yeop Lee, Vito W. Scarola, and J. K. Jain. Stripe formation in the fractional quantum hall regime. *Phys. Rev. Lett.*, 87:256803, Nov 2001.

[63] Seung-Yeop Lee, Vito W. Scarola, and J. K. Jain. Structures for interacting composite fermions: Stripes, bubbles, and fractional quantum hall effect. *Phys. Rev. B*, 66:085336, Aug 2002.

[64] Titus Neupert, Luiz Santos, Claudio Chamon, and Christopher Mudry. Fractional quantum hall states at zero magnetic field. *Phys. Rev. Lett.*, 106:236804, Jun 2011.

[65] D. N. Sheng, Z.-C. Gu, K. Sun, and L. Sheng. Fractional quantum Hall effect in the absence of Landau levels. *Nat. Comm.*, 2, July 2011.

[66] N. Regnault and B. Andrei Bernevig. Fractional chern insulator. *Phys. Rev. X*, 1:021014, Dec 2011.

[67] Y.-L. Wu, B. A. Bernevig, and N. Regnault. Zoology of fractional Chern insulators. *Phys. Rev. B*, 85(7):075116, 2012.

[68] A. M. Läuchli, Zhao Liu, E. J. Bergholtz, and R. Moessner. Hierarchy of fractional chern insulators and competing compressible states. *Phys. Rev. Lett.*, 111:126802, Sep 2013.

[69] Tianhan Liu, C. Repellin, B. Andrei Bernevig, and N. Regnault. Fractional chern insulators beyond laughlin states. *Phys. Rev. B*, 87:205136, May 2013.

[70] Siddharth A. Parameswaran, Rahul Roy, and Shivaji L. Sondhi. Fractional quantum hall physics in topological flat bands. *Comptes Rendus Physique*, 14(9–10):816 – 839, 2013.

[71] EMIL J. Bergholtz and Zhao Liu. Topological flat band models and fractional chern insulators. *International Journal of Modern Physics B*, 27(24):1330017, 2013.

[72] Adolfo G. Grushin, Titus Neupert, Claudio Chamon, and Christopher Mudry. Enhancing the stability of a fractional chern insulator against competing phases. *Phys. Rev. B*, 86:205125, Nov 2012.

[73] Stefanos Kourtis, Jörn W. F. Venderbos, and Maria Daghofer. Fractional chern insulator on a triangular lattice of strongly correlated t_{2g} electrons. *Phys. Rev. B*, 86:235118, Dec 2012.

[74] Ying-Hai Wu, J. K. Jain, and Kai Sun. Adiabatic continuity between hofstadter and chern insulator states. *Phys. Rev. B*, 86:165129, Oct 2012.

[75] E. H. Rezayi, F. D. M. Haldane, and Kun Yang. Charge-density-wave ordering in half-filled high landau levels. *Phys. Rev. Lett.*, 83:1219–1222, Aug 1999.

[76] J. K. Jain. *Composite fermions*. Cambridge University Press, 2007.

[77] A. H. MacDonald and G. C. Aers. Inversion-layer width, electron-electron interactions, and the fractional quantum hall effect. *Phys. Rev. B*, 29:5976–5978, May 1984.

[78] F. C. Zhang and S. Das Sarma. Excitation gap in the fractional quantum hall effect: Finite layer thickness corrections. *Phys. Rev. B*, 33:2903–2905, Feb 1986.

[79] Jörn W. F. Venderbos, Stefanos Kourtis, Jeroen van den Brink, and Maria Daghofer. Fractional quantum-hall liquid spontaneously generated by strongly correlated t_{2g} electrons. *Phys. Rev. Lett.*, 108:126405, Mar 2012.

[80] N. Y. Yao, A. V. Gorshkov, C. R. Laumann, A. M. Läuchli, J. Ye, and M. D. Lukin. Realizing fractional chern insulators in dipolar spin systems. *Phys. Rev. Lett.*, 110:185302, Apr 2013.

[81] Zhao Liu, Emil J. Bergholtz, and Eliot Kapit. Non-abelian fractional chern insulators from long-range interactions. *Phys. Rev. B*, 88:205101, Nov 2013.

[82] Stefanos Kourtis, Titus Neupert, Claudio Chamon, and Christopher Mudry. Fractional chern insulators with strong interactions that far exceed band gaps. *Phys. Rev. Lett.*, 112:126806, Mar 2014.

[83] Kai Sun, Zhengcheng Gu, Hosho Katsura, and S. Das Sarma. Nearly flatbands with nontrivial topology. *Phys. Rev. Lett.*, 106:236803, Jun 2011.

[84] Stefanos Kourtis and Maria Daghofer. Combined topological and landau order from strong correlations in chern bands. *Phys. Rev. Lett.*, 113:216404, Nov 2014.

[85] R. B. Laughlin. Quantized hall conductivity in two dimensions. *Phys. Rev. B*, 23:5632–5633, May 1981.

[86] R. Tao and Yong-Shi Wu. Gauge invariance and fractional quantum hall effect. *Phys. Rev. B*, 30:1097–1098, Jul 1984.

[87] B. I. Halperin. Quantized hall conductance, current-carrying edge states, and the existence of extended states in a two-dimensional disordered potential. *Phys. Rev. B*, 25:2185–2190, Feb 1982.

[88] Ranjan Mukhopadhyay, C. L. Kane, and T. C. Lubensky. Sliding luttinger liquid phases. *Phys. Rev. B*, 64:045120, Jul 2001.

[89] C. L. Kane, Ranjan Mukhopadhyay, and T. C. Lubensky. Fractional quantum hall effect in an array of quantum wires. *Phys. Rev. Lett.*, 88:036401, Jan 2002.

[90] Jelena Klinovaja and Daniel Loss. Topological edge states and fractional quantum Hall effect from umklapp scattering. *Phys. Rev. Lett.*, 111(19), Nov 2013.

[91] Titus Neupert, Claudio Chamon, Christopher Mudry, and Ronny Thomale. Wire deconstructionism of two-dimensional topological phases. *Phys. Rev. B*, 90:205101, Nov 2014.

[92] Jelena Klinovaja and Yaroslav Tserkovnyak. Quantum spin Hall effect in strip of stripes model. *Phys. Rev. B*, 90(11):115426, Sep 2014.

[93] M. Z. Hasan and C. L. Kane. Colloquium. *Rev. Mod. Phys.*, 82:3045–3067, Nov 2010.

[94] Xiao-Liang Qi and Shou-Cheng Zhang. Topological insulators and superconductors. *Rev. Mod. Phys.*, 83:1057–1110, Oct 2011.

[95] Naoto Nagaosa, Jairo Sinova, Shigeki Onoda, A. H. MacDonald, and N. P. Ong. Anomalous hall effect. *Rev. Mod. Phys.*, 82:1539, May 2010.

[96] X. G. Wen, Frank Wilczek, and A. Zee. Chiral spin states and superconductivity. *Phys. Rev. B*, 39(16):11413, Jun 1989.

[97] X. G. Wen. Mean-field theory of spin-liquid states with finite energy gap and topological orders. *Phys. Rev. B*, 44:2664–2672, Aug 1991.

[98] S. Raghu, Xiao-Liang Qi, C. Honerkamp, and Shou-Cheng Zhang. Topological Mott insulators. *Phys. Rev. Lett.*, 100:156401, Apr 2008.

[99] Jun Wen, Andreas Rüegg, C.-C. Joseph Wang, and Gregory A. Fiete. Interaction-driven topological insulators on the kagome and the decorated honeycomb lattices. *Phys. Rev. B*, 82:075125, Aug 2010.

[100] Kai Sun, Hong Yao, Eduardo Fradkin, and Steven A. Kivelson. Topological insulators and nematic phases from spontaneous symmetry breaking in 2d fermi systems with a quadratic band crossing. *Phys. Rev. Lett.*, 103:046811, Jul 2009.

[101] Yi Zhang, Ying Ran, and Ashvin Vishwanath. Topological insulators in three dimensions from spontaneous symmetry breaking. *Phys. Rev. B*, 79:245331, Jun 2009.

[102] C. Weeks and M. Franz. Interaction-driven instabilities of a dirac semimetal. *Phys. Rev. B*, 81:085105, Feb 2010.

[103] Dmytro Pesin and Leon Balents. Mott physics and band topology in materials with strong spin–orbit interaction. *Nat. Phys.*, 6(5):376–381, mar 2010.

[104] Qin Liu, Hong Yao, and Tianxing Ma. Spontaneous symmetry breaking in a two-dimensional kagome lattice. *Phys. Rev. B*, 82(4):045102, jul 2010.

[105] Eduardo V. Castro, Adolfo G. Grushin, Belén Valenzuela, María A. H. Vozmediano, Alberto Cortijo, and Fernando de Juan. Topological Fermi liquids from Coulomb interactions in the doped honeycomb lattice. *Phys. Rev. Lett.*, 107:106402, Sep 2011.

[106] Kai Sun, W. Vincent Liu, Andreas Hemmerich, and S. Das Sarma. Topological semimetal in a fermionic optical lattice. *Nat. Phys.*, 8(1):67–70, nov 2011.

[107] Kai-Yu Yang, Wenguang Zhu, Di Xiao, Satoshi Okamoto, Ziqiang Wang, and Ying Ran. Possible interaction-driven topological phases in (111) bilayers of LaNiO3. *Physical Review B*, 84(20):201104, nov 2011.

[108] Gregory A. Fiete, Victor Chua, Mehdi Kargarian, Rex Lundgren, Andreas Rüegg, Jun Wen, and Vladimir Zyuzin. Topological insulators and quantum spin liquids. *Physica E: Low-dimensional Systems and Nanostructures*, 44(5):845 – 859, 2012.

[109] Noel A. García-Martínez, Adolfo G. Grushin, Titus Neupert, Belén Valenzuela, and Eduardo V. Castro. Interaction-driven phases in the half-filled spinless honeycomb lattice from exact diagonalization. *Phys. Rev. B*, 88:245123, Dec 2013.

[110] Adolfo G. Grushin, Eduardo V. Castro, Alberto Cortijo, Fernando de Juan, María A. H. Vozmediano, and Belén Valenzuela. Charge instabilities and topological phases in the extended hubbard model on the honeycomb lattice with enlarged unit cell. *Phys. Rev. B*, 87:085136, Feb 2013.

[111] Bitan Roy and Igor F. Herbut. Topological insulators in strained graphene at weak interaction. *Phys. Rev. B*, 88:045425, Jul 2013.

[112] Igor F. Herbut and Lukas Janssen. Topological Mott insulator in three-dimensional systems with quadratic band touching. *Phys. Rev. Lett.*, 113(10):106401, sep 2014.

[113] T. Äńurić, N. Chancellor, and I. F. Herbut. Interaction-induced anomalous quantum Hall state on the honeycomb lattice. *Phys. Rev. B*, 89(16):165123, April 2014.

[114] Wei-Feng Tsai, Chen Fang, Hong Yao, and Jiangping Hu. Interaction-driven topological and nematic phases on the lieb lattice. *New J. Phys.*, 17(5):055016, 2015.

[115] Johannes Motruk, Adolfo G. Grushin, Fernando de Juan, and Frank Pollmann. Interaction-driven phases in the half-filled honeycomb lattice: An infinite density matrix renormalization group study. *Phys. Rev. B*, 92:085147, Aug 2015.

[116] Sylvain Capponi and Andreas M. Läuchli. Phase diagram of interacting spinless fermions on the honeycomb lattice: A comprehensive exact diagonalization study. *Phys. Rev. B*, 92:085146, Aug 2015.

[117] A. Dauphin, M. Müller, and M. A. Martin-Delgado. Quantum simulation of a topolog-

ical Mott insulator with Rydberg atoms in a Lieb lattice. *Phys. Rev. A*, 93(4):043611, apr 2016.

[118] W. Zhu, S.-S. Gong, T.-S. Zeng, L. Fu, and D. N. Sheng. Interaction-Driven Spontaneous Quantum Hall Effect on a Kagome Lattice. *Phys. Rev. Lett.*, 117(9):096402, August 2016.

[119] H.-Q. Wu, Y.-Y. He, C. Fang, Z. Y. Meng, and Z.-Y. Lu. Diagnosis of Interaction-driven Topological Phase via Exact Diagonalization. *Phys. Rev. Lett.*, 117(6):066403, August 2016.

[120] Satoshi Nishimoto, Masaaki Nakamura, Aroon O'Brien, and Peter Fulde. Metal-insulator transition of fermions on a kagome lattice at 1/3 filling. *Phys. Rev. Lett.*, 104(19):196401, may 2010.

[121] Bitan Roy and Jay D. Sau. Competing charge-density wave, magnetic, and topological ground states at and near dirac points in graphene in axial magnetic fields. *Phys. Rev. B*, 90:075427, Aug 2014.

[122] Frank Pollmann, Krishanu Roychowdhury, Chisa Hotta, and Karlo Penc. Interplay of charge and spin fluctuations of strongly interacting electrons on the kagome lattice. *Phys. Rev. B*, 90(3):035118, jul 2014.

[123] Moyuru Kurita, Youhei Yamaji, and Masatoshi Imada. Stabilization of topological insulator emerging from electron correlations on honeycomb lattice and its possible relevance in twisted bilayer graphene. *Phys. Rev. B*, 94(12):125131, sep 2016.

[124] Tianhan Liu, Benoît Douçot, and Karyn Le Hur. Realizing topological mott insulators from the rkky interaction. *Phys. Rev. B*, 93:195153, May 2016.

[125] G. W. Stewart. A krylov–schur algorithm for large eigenproblems. *SIAM Journal on Matrix Analysis and Applications*, 23(3):601–614, jan 2002.

[126] Chen Fang, Matthew J. Gilbert, and B. Andrei Bernevig. Bulk topological invariants in noninteracting point group symmetric insulators. *Phys. Rev. B*, 86:115112, Sep 2012.

[127] Y. Z. Zheng, M. L. Tong, W. Xue, W. X. Zhang, X. M. Chen, F. Grandjean, and G.J Long. A star antiferromagnet: A polymeric iron(iii) acetate that exhibits both spin frustration and long-range magnetic ordering. *Angew. Chem. Int. Ed.*, 46:6076, 2007.

[128] Rosa Llusar, Santiago Uriel, Cristian Vicent, Juan M. Clemente-Juan, Eugenio Coronado, Carlos J. Gamez-Garcia, Benoit Brada, and Enric Canadell. Single-component magnetic conductors based on mo3s7 trinuclear clusters with outer dithiolate ligands. *Jour. of the Amer. Chem. Soc.*, 126(38):12076–12083, 2004.

[129] A. C. Jacko, A. L. Khosla, J. Merino, and B. J. Powell. Spin-orbit coupling in $mo_3s_7(dmit)_3$. *Phys. Rev. B*, 95:155120, Apr 2017.

[130] D. Jaksch, C. Bruder, J. I. Cirac, C. W. Gardiner, and P. Zoller. Cold bosonic atoms in optical lattices. *Phys. Rev. Lett.*, 81(15):3108, OCT 12 1998.

[131] M. Greiner, O. Mandel, T. Esslinger, T. W. Hansch, and I. Bloch. Quantum phase transition from a superfluid to a Mott insulator in a gas of ultracold atoms. *Nature*, 415(6867):39, JAN 3 2002.

[132] I. Bloch, J. Dalibard, and W. Zwerger. Many-body physics with ultracold gases. *Rev. Mod. Phys.*, 80:885, 2008.

[133] R. B. Laughlin. Quantized motion of three two-dimensional electrons in a strong magnetic field. *Phys. Rev. B*, 27:3383, Mar 1983.

[134] S. D. Huber and E. Altman. Bose condensation in flat bands. *Phys. Rev. B*, 82:184502, Nov 2010.

[135] C. Becker, P. Soltan-Panahi, J. Kronjäger, S. Dörscher, K. Bongs, and K. Sengstock. Ultracold quantum gases in triangular optical lattices. *New J. Phys.*, 12(6):065025, Jun 2010.

[136] Congjun Wu, Doron Bergman, Leon Balents, and S. Das Sarma. Flat bands and wigner crystallization in the honeycomb optical lattice. *Phys. Rev. Lett.*, 99(7):070401, AUG 17 2007.

[137] P. Soltan-Panahi, J. Struck, P. Hauke, A. Bick, W. Plenkers, G. Meineke, C. Becker, P. Windpassinger, M. Lewenstein, and K. Sengstock. Multi-component quantum gases in spin-dependent hexagonal lattices. *Nat. Phys.*, 7(5):434–440, 05 2011.

[138] Leticia Tarruell, Daniel Greif, Thomas Uehlinger, Gregor Jotzu, and Tilman Esslinger. Creating, moving and merging Dirac points with a Fermi gas in a tunable honeycomb lattice. *Nature*, 483(7389):302, Mar 2012.

[139] G. Jo, J. Guzman, C. K. Thomas, P. Hosur, A. Vishwanath, and D. M. Stamper-Kurn. Ultracold atoms in a tunable optical kagome lattice. *Phys. Rev. Lett.*, 108:045305, 2012.

[140] J. Higbie and D. M. Stamper-Kurn. Periodically dressed Bose-Einstein condensate: A superfluid with an anisotropic and variable critical velocity. *Phys. Rev. Lett.*, 88:090401, Feb 2002.

[141] Y.-J. Lin, K. Jiménez-García, and I. B. Spielman. Spin-orbit-coupled Bose-Einstein condensates. *Nature*, 471:83, 2011.

[142] Jay D. Sau, B. I. Halperin, K. Flensberg, and S. Das Sarma. Number conserving

theory for topologically protected degeneracy in one-dimensional fermions. *Phys. Rev. B*, 84:144509, 2011.

[143] B. Ramachandhran, Bogdan Opanchuk, Xia-Ji Liu, Han Pu, Peter D. Drummond, and Hui Hu. Half-quantum vortex state in a spin-orbit-coupled Bose-Einstein condensate. *Phys. Rev. A*, 85:023606, Feb 2012.

[144] Hui Hu, B. Ramachandhran, Han Pu, and Xia-Ji Liu. Spin-orbit coupled weakly interacting Bose-Einstein condensates in harmonic traps. *Phys. Rev. Lett.*, 108:010402, Jan 2012.

[145] X. Zhou, Y. Li, Z. Cai, and C. Wu. Unconventional states of bosons with the synthetic spin-orbit coupling. *Journal of Physics B Atomic Molecular Physics*, 46(13):134001, July 2013.

[146] V. Galitski and I. B. Spielman. Spin-orbit coupling in quantum gases. *Nature*, 494:49, February 2013.

[147] Y. Zhang and C. Zhang. Bose-Einstein condensates in spin-orbit-coupled optical lattices: Flat bands and superfluidity. *Phys. Rev. A*, 87:023611, Feb 2013.

[148] H. Hui, Z. Zhang, C. Zhang, and V.W. Scarola. Superfluidity in the absence of kinetics in spin-orbit-coupled optical lattices. *arXiv preprint arXiv:1606.08439*, 2016.

[149] RB Laughlin. Anomalous quantum Hall-effect - an incompressible quantum fluid with fractionally charged excitations. *Phys. Rev. Lett.*, 50:1395, 1983.

[150] F. Lin, C. Zhang, and V. W. Scarola. Emergent kinetics and fractionalized charge in 1D spin-orbit coupled flatband optical lattices. *Phys. Rev. Lett.*, 112:110404, Mar 2014.

[151] F. D. M. Haldane. Effective harmonic-fluid approach to low-energy properties of one-dimensional quantum fluids. *Phys. Rev. Lett.*, 47:1840, Dec 1981.

[152] M. P. A. Fisher and L. I. Glazman. Transport in a one-dimensional Luttinger liquid. *Proceedings of the NATO Advanced Study Institute*, 345:331, 1997.

[153] E. Miranda. Introduction to bosonization. *Brazilian Journal of Physics*, 33:3, 03 2003.

[154] T. Gimarchy. *Quantum Physics in One Dimension*. Oxford University Press, 2013.

[155] Hoi-Yin Hui, Mengsu Chen, Sumanta Tewari, and V. W. Scarola. Chiral topological phases in optical lattices without synthetic fields. *Physical Review A*, 98(2):023609, August 2018.